UNIVERSIDADE FEDERAL DO RIO GRANDE DO SUL
INSTITUTO DE FÍSICA
PROGRAMA DE PÓS-GRADUAÇÃO

Mateus Henrique Köhler

WATER STRUCTURE AND DYNAMICS THROUGH FUNCTIONALIZED SURFACES

Porto Alegre(RS)

2018

Mateus Henrique Köhler

WATER STRUCTURE AND DYNAMICS THROUGH FUNCTIONALIZED SURFACES

Tese apresentada ao Programa de Pós-Graduação do Instituto de Física da Universidade Federal do Rio Grande do Sul sob orientação da Prof^{a}. Dr^{a}. Marcia Cristina Bernardes Barbosa e Prof. Dr. Leandro Barros da Silva, como parte dos requisitos para a obtenção do título de Doutor.

Porto Alegre(RS)

2018

Resumo

Neste trabalho propomos uma investigação através de simulações de dinâmica molecular da água em contato com superfícies hidrofóbicas e hidrofílicas, tanto dentro de nanotubos funcionalizados quanto em membranas bi-dimensionais para dessalinização. No caso da água em contato com superfícies hidrofóbicas e hidrofílicas de nanotubos nós encontramos uma quebra na relação de Stokes-Einstein para a difusão e a viscosidade da água. Essa quebra ocorre para os menores nanotubos − em que pelo menos duas camadas de água formam-se, condição para deslizamento de camadas necessária para o cálculo da viscosidade. O mecanismo por trás deste comportamento é ditado pela estrutura da água confinada. Esse resultado indica que algumas das características observadas para a água dentro de nanotubos hidrofóbicos, como nanotubos de carbono na natureza, são únicas.

Encontramos uma grande dependência da dinâmica e estrutura da água confinada com as características polares do nanotubo, principalmente para nanotubos com diâmetros menores que 1 nm. Ao variarmos a temperatura do sistema, observamos ainda uma forte dependência da estruturação das moléculas de água com a temperatura, a ponto de apresentar transições entre estados mais e menos ocupados.

Nossos resultados de dinâmica molecular também mostram que membranas contendo nanoporos com sítios hidrofílicos entre regiões hidrofóbicas podem apresentar grande fluxo de água e reduzido transporte de íons, o que torna esses materiais excelentes candidatos para sistemas de dessalinização e limpeza de metais pesados. Ao acrescentarmos um químico floculante (cloreto de ferro) à água salgada, encontramos resultados ainda melhores para a rejeição de sal pelas membranas nanoporosas. Todos esses resultados demonstram a importância do estudo das propriedades hidrofóbicas e hidrofílicas em interfaces aquosas. Em todos os casos, encontramos uma dependência inerente das propriedades de transporte da água com a característica polar da superfície de contato.

Abstract

In this work we have proposed an investigation through molecular dynamics (MD) simulations of the water behavior at hydrophobic and hydrophilic surfaces in both functionalyzed nanotubes and two-dimensional nanpores. In the case of water at hydrophobic and hydrophilic nanotube surfaces, we have found a breakdown of the Stokes-Einstein relation for diffusion and viscosity of water confined in narrow hydrophobic nanopores. The mechanism underlying this behavior is dictated by the structure of water under confinement. This result indicates that some of the features observed for water inside hydrophobic carbon nanotubes cannot be observed in other nanopores.

We have also found an important dependence of the water dynamics with the polar character of the nanotube, mostly for small diameters. By varying the temperature, both the dynamics and the water structuration are affected, presenting transitions between dense-packed and low-density states.

Our results also shows that nanoporous membranes, with hydrophilic sites sandwiched between hydrophobic regions, can present an important flux of water molecules and reduced ion transportation, making these structures promising for desalination processes. By adding a flocculant ingredient (ferric chloride) to the salt water, we found even larger ion rejection rates. All the results point out the importance of studying hydrophilic and hydrophobic interfaces for water transport. In all the cases, we have found an ubiquitous dependence of water dynamic properties on the surface polarity.

Keywords: water, hydrophobic and hydrophilic surface, nanopores

Contents

Chapter 1

Introduction

1.1 Water at Hydrophobic and Hydrophilic Surfaces

Understanding and predicting the behavior of water, especially in contact with various surfaces, is a scientific challenge and, for many applications in nanofluidic technology [1, 2] and almost all situations in the biological domain [3], the behavior of interfacial water is of prime importance. The geometric constraint of a solid surface as well as the interactions between water molecules and the substrate lead to structural changes in the confined water when compared to its bulk properties.

Surfaces can be divided in two classes according to their affinity to water as follows. The hydrophilic surfaces, such as mica, which exhibit polar groups capable of forming hydrogen bonds with water molecules, thus, attracting water and leading to small contact angles, $\theta < 90°$ [4], as defined in Figure 1.1. The nonpolar, hydrophobic surfaces, such as polystyrene and the alkane-functionalized surfaces [5, 6], characterized by contact angles $\theta > 90°$. The hydrogen-bonding network of water is distorted at such surfaces because they do not form hydrogen bonds, thus water repellent. This results in a fluctuating vapor-water-like depletion layer at the surface with far-reaching consequences for solvation processes and self-assembly [7].

The hydrophobicity of a solid surface plays an important role in phenomena such as adhesion, wetting, and capillary filling. As a result, the process of hydrophobization is widely used in many industrial technologies, especially in the destabilization of aqueous colloidal suspensions. For example, in mineral separation techniques, the degree of hydrophobicity of mineral particles determines their flotability since particle-bubble attachment is one of the decisive processes in flotation [8].

Since water molecules present dipole moment they interact favorably with surface

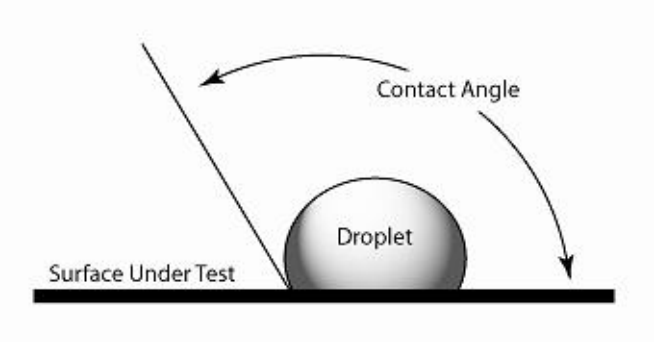

Figure 1.1: Definition of the contact angle between a water droplet and a solid surface.

charges, therefore confining geometries which bear electric charges or polar groups are hydrophilic. In contrast, non polar surfaces are generally hydrophobic since the water molecules suffer a loss of hydrogen bonding partners at the interface. This classification into hydrophobic and hydrophilic surfaces has profound influence over many systems such as interacting colloidal particles, protein folding, and adsorption of molecules or more complex structures on surfaces.

Another aspect in which the confining system influences a fluid is within the hydrodynamics behavior. Over the past years it has become increasingly clear that the no-slip boundary condition, that is, the condition of zero interfacial fluid velocity, does not necessarily hold at nanoscopic length scales [9, 10]. In fact, the hydrodynamic boundary condition at the liquid/solid interface is of particular importance for nanofluidic applications [3, 11, 12] or biological nanoscale scenarios, such as the transport through membrane channels [13, 14].

Surface slippage amplifies the flow rate for pressure driven flow, which enhances fluid transport in narrow channels. Clearly, a noticeable increase of fluid transport is only obtained if the slip length is comparable to the channel dimension. For electrically driven flow, on the other hand, even small slip lengths in the nanometer range lead to a considerable increase in flow [15]. All these examples demonstrate that a molecular level understanding of the flow boundary condition at surfaces is necessary.

In this respect, carbon nanotubes (CNTs) are the ultimate one-dimensional (1D) hydrophobic surfaces for water transportation. Their sp^2 carbon atoms arranged in a cylindrical honeycomb lattice allows for the so-called water super-flux [11]. This phenomena is mainly related to the hydrogen bond network distributed along the axial direction of the nanopore [16]. Because of the restricted space for the hydrogen bond formation inside the CNT, water align in a single-file structure, as represented in Figure 1.2.

Studying the behavior of liquids inside nanotubes, represent a modern scientific chal-

Figure 1.2: Inside the inner of a small carbon nanotube (diameter < 1 nm), water forms the so-called "single-file" structures.

lenge. The hydrophobic inner of a CNT is expected to induce heterogeneous water dynamics, with several structural transitions. Functionalization of CNTs provides a variety of fluid-surface interactions, leading to transitions between hydrophobic and hydrophilic states. The tuning of the nanotube polarity have been recently found to induce several anomalies in water behavior, such as the breakdown of Stokes-Einstein relation [17], several ice-structural transitions [18, 19], and enhanced diffusion [20, 21]. All of these results indicate how promising and at the same time intriguing are the physical-chemistry of water confined in nanotube interfaces.

The interfaces are present even in systems in which the fluid is not confined. Biomolecular surfaces, such as proteins, can also pose a formidable challenge to the movement of water around its surface. Hydrophobicity plays a key role in this phenomenon, reducing the number, lifetime and strength of hydrogen bonds between water and the amino acids. In the hydration shell, the first layer of water around a protein, both dynamics and structural features are expected to differ from the bulk. But while water is affected by the polarity of the protein surface, its presence also triggers a sequence of events in the protein itself. Water is an essential participant in the stability, structure, dynamics, and function of biomolecules. Thermodynamically, changes in the aqueous environment affect the stability of biomolecules. Structurally, water participates chemically in the catalytic function of proteins and nucleic acids and physically in the collapse of the protein chain during folding through hydrophobic collapse and mediates binding through the hydrogen bond in complex formation [22]. In fact, several techniques, such as X-ray and neutron crystallography, NMR, terahertz spectroscopy, mass spectroscopy, and computer simulations, have been used to show that water is a partner that slaves the dynamics of proteins, and water interaction with proteins affect their dynamics. In this respect, we can say that

water is certainly a protagonist.

1.2 Water through functionalized nanopores: 2D membranes for desalination

Currently, 97.5% of the world's water is salty, with a mere 2.5% of fresh water remaining for human consumption [23]. Furthermore, augmented agricultural and industrial activity has yielded increased contamination of our limited water resources due to the widespread dispersion of various industrial dyes, heavy metal ions, and other aromatic pollutants [23]. Consequently, an enhanced global endeavour has surfaced in an attempt to develop economical and efficient technologies for disinfection, decontamination and desalination in order to establish water security and create environmental and public health sustainability.

Although the practice of removing salt from water may seem theoretically straightforward, in reality, this challenging task is often exceedingly costly and extremely strenuous [24, 25, 26]. Prevailing reverse osmosis (RO) desalination technologies require approximately 3 kW/h of energy to force pre-filtered sea water through a series of semi-permeable membranes, under pressure, to produce a mere 1 m^3 of drinkable water [27]. Moreover, conventional polymeric membranes are relentlessly defied by fouling [25, 28]. Impurities and biological materials present in the water feed congregate on the membrane surface [29] or within the pores of the membrane, resulting in poor membrane selectivity, listless water flow, reduced membrane resilience and increased energy consumption. As a consequence, a greater extent of energy is required to force water through the membrane.

A solution to the water scarcity may lie within the new generation of nanoscale materials. To date, much research has focused on the ability of carbon nanotubes or zeolites to act as nanostructure membranes for ion separation [30]. Recent studies have also attempted to improve water permeability by molecular sieve action of polymers [31] and ceramics [32]. Although these materials are theoretically promising, their practical applications are not yet fully explored. Membranes fabricated from materials such as zeolites and carbon nanotubes are difficult to shape in a cost effective and scalable manner and prove somewhat ineffective with regard to the exclusion of salt ions, as well as presenting a low water flux [33, 34], hence illustrating the need for ultrathin, low cost membranes.

Owing to their atomically thin structure, large surface area and mechanical strength, 2D nanoporous materials are considered to be suitable alternatives for existing desalination and water purification membrane materials [35]. Recent progress in the development

Table 1.1: Relevant 2D materials and their applications in water treatment.

		Material properties	Application in water treatment	Ref.
Group IV graphene analogues	Graphene	Immense mechanical strength (1.0 TPa), pronounced surface area (2630 m^2g^{-1}), hydrophobic	Desalination	[36]
	2D boron nitride	Chemically inert, mechanical strength (0.81-1.3 TPa), hydrophobic	Contaminant/ pollutant adsorption	[37]
Chalco-genides	Molybdenum disulfide (MoS_2)	High thermal stability (up to 1100°C), good mechanical strength	Desalination	[38, 39]
	Tungsten chalcogenides (WS_2)	Semiconductor (2.1 eV), electron mobility of 20 $cm^2V^{-1}s^{-1}$	Desalination, Degradation of contaminants	[40]
MXenes (transition metal carbides)	Titanium carbide ($Ti_3C_2T_x$)	Structural and chemical stability, excellent conductivity, non-toxic, hydrophilic	Contaminant/ pollutant adsorption	[41, 42]

of nanoporous graphene based materials has generated enormous potential for water purification technologies.

Though many novel 2D crystals have recently been isolated from bulk structures, few 2D nanosystems have been exploited commercially for water purification (Table 1.1). However, due to their desirable properties graphene like 2D nanostructures are expected to have a significant influence on a multiplicity of applications and could potentially serve as high-performance membranes. The hexagonal form, h-BN, also known as white graphene, began to attract attention after the chemically stable insulator surfaced as an excellent substrate for mono- and bilayer graphene devices [43, 44], increasing graphene's electronic mobility by an order of magnitude. A porous layered BN nanostructure was prepared via thermal treatment for removal of oils, organic solvents and dyes from water [37]. The superhydrophobic nanosheets exhibited an exceptional surface area of 1427 m^2g^{-1}, allowing them to absorb up to 33 times their own weight. Furthermore the highly selective, porous, layered BN nanomaterial can be regenerated upon burning or heating due to its

high oxidative resistance, which supports reuse of the nanosheets.

MoS_2 is the most widely employed transition metal dichalcogenide (TMD) in a range of applications and has recently been investigated for its potential in separation techniques. MoS_2, a prototypical TMD, is made up of hexagonal layers of Mo and S_2 atoms. TMDs, a family of over 40 materials, are represented by the generalized formula, MX_2, and consist of a transition metal (M), for example, Mo, W, Nb, Re, Ni, or V, packed between two chalcogens (X) such as S, Se or Te. A flexible laminar separation membrane prepared from MoS_2 sheets exhibited a water flux 3-5 times higher than that reported for graphene oxyde (GO) and has been shown to reject 89% and 98% of Evans Blue and cytochrome C molecules, respectively [45]. Similarly, a tungsten disulfide (WS2) membrane has exhibited a water flux five times greater than GO membranes and two times greater than MoS_2 laminar membranes rejecting 90% of Evans Blue molecules. These results reinforce the idea that the surface at nanometric interfaces plays a very important role, leading to anomalous water events that can be used to advance technologies such as desalination and even energy storage.

Whenever the confinement is between nanopores or biomembranes, water behavior at hydrophobic and hydrophilic surfaces is often extraordinary, leading to new and exiting discoveries day by day [17, 46, 47, 48]. This subject is, therefore, very interesting and promising not just for chemical and physical aspects, but for technological purposes. For example, one might think of a power generation system based on the motion of water through nanotubes guided only by the hydrophobicity of the pore [49].

In this work, we propose a systematic investigation of the influence of both hydrophobic and hydrophilic surfaces on the structure and transport of the confined water. To this end, we have used molecular dynamics simulations and all its power of atomic level description of physical phenomena. In the chapter 2 we present the methodology employed in this analysis. In the chapter 3 the results for water confined in functionalized nanotubes are discussed, and in the chapter 4 the water dynamics through 2D nanopores is analyzed, highlighting the promising application in desalination processes. The mobility of water through hydrophobic and hydrophilic confining geometries are measured and compared, and the structure of low density water inside nanotubes is also computed. Conclusions and perspectives are presented in the chapter 4. The articles that resulted from this work are reproduced in the appendices A, B, C, D and E.

Chapter 2

Methodology

In this chapter we present the methods employed in the different problems analyzed in this work.

2.1 Transport coefficients

The transport of mass, energy or momentum is described, to first order, by a phenomenological relation of form

$$\text{Flux} = -\text{ coefficient} \times \text{gradient}. \tag{2.1}$$

The flux measures the transfer per unit area in unit time, the gradient provides the driving force for the flux, and the coefficient characterizes the resistance to flow. Examples of such relations include Newton's law of viscosity, Fick's law of diffusion, Fourier's law of heat conduction, and Ohm's law of electrical conduction. We normally think of these laws applied to nonequilibrium situations: for instance, when a temperature gradient is applied to a pot of water, the pot offers a resistance in terms of a thermal conductivity, and the result is a heat flux transfered through the water. But in addition to nonequilibrium situations, the linear transport equations also apply to microscopic fluctuations that occur in a system at equilibrium [50]. In the next sections we explain how the transport coefficients, which are properties of matter, can be extracted from equilibrium molecular dynamics simulations.

2.1.1 Einstein relation for diffusion

The one-dimensional diffusion as described by Fick's law:

$$N\dot{x} = -D\frac{\partial N}{\partial x}, \tag{2.2}$$

where $N = N(x,t)$ is the number of atoms per unit volume located at position x at time t, $\dot{x}$ is the local velocity at (x,t), and D is the diffusion coefficient. Then $(N\dot{x})$ is the flux. From a material balance on a differential element of fluid, we obtain the equation for continuity of mass:

$$\frac{\partial N}{\partial t} + \frac{\partial\left(N\dot{x}\right)}{\partial x} = 0 \tag{2.3}$$

and combining these two equations gives the diffusion equation:

$$\frac{\partial N}{\partial t} = D\frac{\partial^2 N}{\partial x^2}. \tag{2.4}$$

For a set of initial conditions, the diffusion equation can be solved for the temporal and spatial evolution of $N(x,t)$. For example, if N_0 atoms were concentrated at the origin $x = 0$ at time $t = 0$, then the solution could be written as:

$$N(x,t) = \frac{N_0}{2\sqrt{\pi Dt}}\exp\left[\frac{-x^2}{4Dt}\right]. \tag{2.5}$$

At any time $t > 0$ the atoms are spatially distributed in a Gaussian about the origin, and as time evolves, atoms diffuse away from the origin, causing the Gaussian to collapse. We can imagine, for instance, one drop of ink added to a pan of water: the water is left undisturbed so, at the point of insertion, the local concentration slowly decreases as the ink diffuses throughout the container.

At any time $t > 0$ the second moment of the distribution gives the mean-square displacement of atoms:

$$\left\langle[x(t) - x(0)]^2\right\rangle = \frac{1}{N_0}\int x^2 N(x,t)dx. \tag{2.6}$$

By combining Equations 2.5 and 2.6, we can integrate to find that the mean-square displacement is simply related to the diffusion coefficient:

$$\left\langle[x(t) - x(0)]^2\right\rangle = 2Dt, \tag{2.7}$$

which is the well known relation due to Einstein. This result applies when the time t is large compared to the average time between collisions of atoms. The three-dimensional analog is then:

$$\lim_{t\to\infty} \frac{\left\langle [\boldsymbol{r}(t) - \boldsymbol{r}(0)]^2 \right\rangle}{6t} = D. \tag{2.8}$$

This is not just a direct consequence of Fick's law of diffusion, it is also a relation characteristic of a random walk, in which the mean-square displacement of the walker becomes a linear function of time after a sufficiently large number of random steps. The nature of the limiting process involved in Equation 2.8 highlights the general importance of taking the thermodynamic limit before the limit $t \to \infty$. For a system of finite volume V, the diffusion coefficient defined by Equation 2.8 is strictly zero, since the maximum achievable mean-square displacement is of order $\mathrm{V}^{2/3}$ [51]. In practice, for a system of macroscopic dimensions, the ratio on the left-hand side of Equation 2.8 will reach a plateau value at times much shorter than those required for the diffusing particles to reach the boundaries of the system; it is the plateau value that provides the definition of D for a finite system. In realizing Equation 2.8 from simulations, the brackets would be interpreted as averages over time origins. Since at a specified state condition the diffusion coefficient is a constant, Equation 2.8 implies that the mean-square displacement grows linearly at large delay times.

2.1.2 Time-correlation functions and transport coefficients

Transport coefficients are defined in terms of the response of a system to a perturbation. For example, the diffusion coefficient relates the particle flux to a concentration gradient, while the shear viscosity is a measure of the shear stress induced by an applied velocity gradient. Generally, a time-dependent, nonequilibrium distribution is produced. Hence, any nonequilibrium *ensemble* average (in particular, the desired response) may be calculated. By retaining the linear terms in the perturbation, and comparing the equation for the response with a macroscopic transport equation, we may identify the transport coefficient. This is usually the infinite time integral of an equilibrium time correlation function of the form

$$\gamma = \int_0^\infty \left\langle \dot{\mathbb{A}}(t)\dot{\mathbb{A}}(0) \right\rangle dt, \tag{2.9}$$

where γ is the transport coefficient, and $\mathbb{A}$ is a variable appearing in the perturbation term in the Hamiltonian. Associated with any expression of this kind, there is also an

"Einstein relation":

$$2t\gamma = \left\langle [\mathbb{A}(t) - \mathbb{A}(0)]^2 \right\rangle , \tag{2.10}$$

which holds at large t (compared with the correlation time of $\mathbb{A}$).

In computer simulations, transport coefficients may be calculated from equilibrium correlation functions, using Equation 2.9, by observing Einstein relations, Equation 2.10, or indeed by going back to first principles and conducting a suitable nonequilibrium simulation. In this sense, by performing equilibrium molecular dynamics, one can determine the shear viscosity η by the integration of the off-diagonal components of the stress tensor of the system:

$$\eta = \frac{V}{k_{\mathrm{B}}T} \int \langle P_{\alpha\beta}(t) P_{\alpha\beta}(0) \rangle \, dt. \tag{2.11}$$

Here,

$$P_{\alpha\beta} = \frac{1}{V} \left(\sum_i \frac{p_{i\alpha} p_{i\beta}}{m_i} + \sum_i r_{i\alpha} f_{i\beta} \right) \tag{2.12}$$

is an off-diagonal ($\alpha \neq \beta$) element of the stress tensor (often called pressure tensor, due to its similarity with virial expression for pressure). These quantities are multiparticle properties, properties of the system as a whole, and so no additional averaging over the N particles is possible. Consequently, η is subject to much greater statistical imprecision than D. Some improvement is possible by averaging over different components ($\alpha\beta = xy, yz, zx$) of $P_{\alpha\beta}$.

2.1.3 Stokes-Einstein relation

Calculating the velocity autocorrelation function can be extremely challenging. The stochastic theory used by Langevin to describe the brownian motion of a large and massive particle in a bath of particles that are much smaller and lighter than itself has found wide application in the theory of transport processes in liquids. The problem is characterized by two very different timescales, one associated with the slow relaxation of the initial velocity of the brownian particle and another linked to the frequent collisions that the brownian particle suffers with particles of the bath. Langevin assumed that the force acting on the brownian particle consists of two parts: a systematic, frictional force proportional to the velocity $\boldsymbol{u}(t)$, but acting in the opposite sense, and a randomly fluctuating force,

$\boldsymbol{R}(t)$, which arises from collisions with surrounding particles. The equation of motion of a brownian particle of mass m is therefore written as

$$m\dot{\boldsymbol{u}}(t) = -m\xi\boldsymbol{u}(t) + \boldsymbol{R}(t), \tag{2.13}$$

where ξ is the friction coefficient. The random force is assumed to vanish in the mean.

The friction coefficient is related to the diffusion coefficient. Lets consider the case when the brownian particle is initially ($t = 0$) situated at the origin ($\boldsymbol{r} = 0$). We wish to calculate the mean-square displacement of the particle after a time t. By multiplying through Equation 2.13 by $\boldsymbol{r}(t)$ and using the results

$$\boldsymbol{r} \cdot \boldsymbol{u} = \boldsymbol{r} \cdot \dot{\boldsymbol{r}} = \frac{1}{2}\frac{\mathrm{d}}{\mathrm{d}t}\boldsymbol{r}^2 \tag{2.14}$$

$$\boldsymbol{r} \cdot \dot{\boldsymbol{u}} = \boldsymbol{r} \cdot \ddot{\boldsymbol{r}} = \frac{1}{2}\frac{\mathrm{d}^2}{\mathrm{d}t^2}\boldsymbol{r}^2 - \boldsymbol{u}^2 \tag{2.15}$$

we find that

$$\frac{1}{2}m\frac{\mathrm{d}^2}{\mathrm{d}t^2}\left|\boldsymbol{r}(t)\right|^2 + \frac{1}{2}\xi m\frac{\mathrm{d}}{\mathrm{d}t}\left|\boldsymbol{r}(t)\right|^2 = m\left|\boldsymbol{u}(t)\right|^2 + \boldsymbol{r}(t) \cdot \boldsymbol{R}(t). \tag{2.16}$$

By taking the statistical mean, Equation 2.16 becomes

$$\frac{\mathrm{d}^2}{\mathrm{d}t^2}\left\langle\left|\boldsymbol{r}(t)\right|^2\right\rangle + \xi\frac{\mathrm{d}}{\mathrm{d}t}\left\langle\left|\boldsymbol{r}(t)\right|^2\right\rangle = \frac{6k_\mathrm{B}T}{m}. \tag{2.17}$$

The solution to Equation 2.15 that satisfies the boundary conditions $\left\langle\left|\boldsymbol{r}(t)\right|^2\right\rangle = 0$ and

$$\frac{\mathrm{d}}{\mathrm{d}t}\left\langle\left|\boldsymbol{r}(t)\right|^2\right\rangle\Big|_{t=0} = 2\left\langle\boldsymbol{r}(0) \cdot \boldsymbol{u}(0)\right\rangle = 0 \tag{2.18}$$

can be expanded as follows:

$$\left\langle\left|\boldsymbol{r}(t)\right|^2\right\rangle = \frac{6k_\mathrm{B}T}{\xi m}\left[t - \frac{1}{\xi} + \frac{1}{\xi}\exp(-\xi t)\right]. \tag{2.19}$$

At very large times, such that $\xi t \gg 1$, the solution becomes:

$$\left\langle\left|\boldsymbol{r}(t)\right|^2\right\rangle \simeq \left(\frac{6k_\mathrm{B}T}{\xi m}\right)t \tag{2.20}$$

and comparison to Equation 2.8 leads to Einstein's expression for the diffusion coefficient:

$$D = \frac{k_{\mathrm{B}}T}{\xi m}. \tag{2.21}$$

An estimate of ξ can be obtained from a hydrodynamic calculation of the frictional force on a sphere of diameter d moving with constant velocity $\boldsymbol{u}$ in a fluid of shear viscosity η. This leads to a famous result due to Stokes, the precise form of which depends on the assumptions made about the behavior at the surface of the sphere of the velocity field created by the fluid. The stress tensor at the surface is then obtained by solving the linearized Navier-Stokes equation, supplemented by the requirement that the fluid velocity must vanish at infinite distance from the sphere. When the stress tensor is known, the total frictional force $\boldsymbol{F}$ can be calculated by integration over the surface. The final result has the form $\boldsymbol{F} = -\xi\boldsymbol{u}$, with

$$\xi = \frac{3\pi\eta d}{m}. \tag{2.22}$$

Combination of Equations 2.22 with 2.21 leads to the familiar form of Stokes-Einstein law:

$$D\eta = \frac{k_{\mathrm{B}}T}{3\pi d}, \tag{2.23}$$

where d stands for the system's dimensionality. It is a remarkable feature of Stokes's law that although it is derived from purely macroscopic considerations, and is apparently limited to brownian particles, it also provides a good, empirical correlation of experimental data on simple liquids.

2.2 Molecular dynamics: Modeling the system

The goal in a molecular dynamics simulation lies in choosing the interaction potential: a function $V(\boldsymbol{r}_1,...,\boldsymbol{r}_N)$ of the atomic positions, representing the potential energy of the system when the atoms are arranged in that specific configuration. This function is translationally and rotationally invariant, and is usually constructed from the relative positions of the atoms with respect to each other, rather than from the absolute positions.

Forces are then derived as the gradients of the potential with respect to atomic displacements:

$$\boldsymbol{F}_i = -\nabla_{\boldsymbol{r}} V(\boldsymbol{r}_1,...,\boldsymbol{r}_N). \tag{2.24}$$

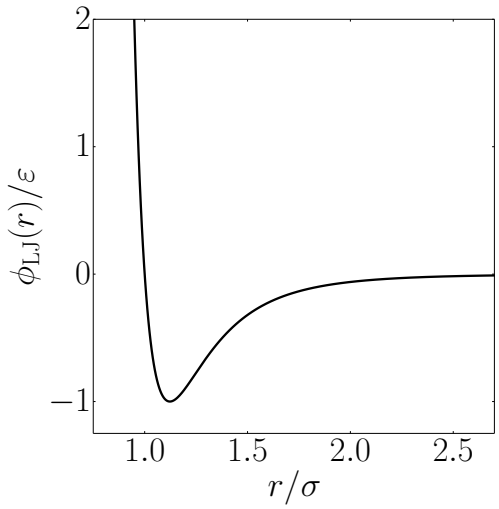

Figure 2.1: Representation of the Lennard-Jones potential.

This form implies the presence of a conservation law of the total energy $E = K + V$, where K is the instantaneous kinetic energy.

The simplest choice for V is to write it as a sum of pairwise interactions:

$$V(\boldsymbol{r}_1,...,\boldsymbol{r}_N) = \sum_i \sum_{j>i} \phi\left(|\boldsymbol{r}_i - \boldsymbol{r}_j|\right). \tag{2.25}$$

The clause $j > i$ in the second summation has the purpose of considering each atom pair only once. Though the Lennard-Jones (LJ) pair potential is currently the most commonly used interaction model, the development of accurate potentials represents an important research line.

2.2.1 The Lennard-Jones potential

The LJ potential is given by the expression

$$\phi_{\mathrm{LJ}}(\boldsymbol{r}) = 4\varepsilon \left[\left(\frac{\sigma}{\boldsymbol{r}}\right)^{12} - \left(\frac{\sigma}{\boldsymbol{r}}\right)^{6} \right] \tag{2.26}$$

for the interaction potential between a pair of atoms − the total potential of a system containing N atoms may be given by Equation 2.25. As shown in Figure 2.1, the LJ potential has an attractive tail at large $\boldsymbol{r}$ and is strongly repulsive at shorter distance, passing through 0 at $\boldsymbol{r} = \sigma$ and increasing steeply as $\boldsymbol{r}$ is decreased further.

The term $\sim \boldsymbol{r}^{-12}$, which dominates at short distance, models the repulsion between atoms when they are brought very close to each other. Its physical origin is related to

the Pauli principle: when the electronic clouds surrounding the atoms starts to overlap, the energy of the system increases abruptly. The exponent 12 was chosen exclusively on a practical basis: to make the computation easier.

The term $\sim \boldsymbol{r}^{-6}$, which dominates at large distance, constitute the attractive part. This is the term which gives cohesion to the system. The $\boldsymbol{r}^{-6}$ attraction is closely linked to the van der Waals dispersion forces, originated by dipole-dipole interactions in turn due to fluctuating dipoles. These are rather weak interactions, which however dominate the bonding character of closed-shell systems.

Regardless of how well it is able to model actual materials, the LJ potential constitutes an extremely important modeling potential system. There is a vast body of papers which investigate the behavior of atoms interacting via LJ on a variety of different geometries (solids, liquids, surfaces and clusters). One could say that LJ is the standard potential to use for all the investigations where the focus is on fundamental issues, rather than studying the properties of a specific material.

2.2.2 Truncation and long-range corrections

The potential of Equation 2.26 has an infinite range. However, in practical applications it is customary to establish a cutoff radius R_c and disregard the interactions between atoms separated by distances greater than R_c. This results in simpler programs and enormous saving of computer resources, since the number of atomic pairs grows with $\boldsymbol{r}^2$.

A simple truncation of the potential creates a new problem: whenever a particle pair crosses the cutoff distance, the energy shows a little jump. A large number of these events is likely to spoil energy conservation in a simulation. To avoid this problem, the potential is often shifted in order to vanish at the cutoff radius:

$$V(\boldsymbol{r}) = \begin{cases} \phi_\mathrm{LJ}(\boldsymbol{r}) - \phi_\mathrm{LJ}(R_\mathrm{c}) & \text{if } \boldsymbol{r} \leq R_\mathrm{c} \\ 0 & \text{if } \boldsymbol{r} > R_\mathrm{c} \end{cases} \tag{2.27}$$

Physical quantities are of course affected by the potential truncation. The effects of truncating a full-ranged potential can be approximately estimated by treating the system as a uniform continuum beyond R_c. For a bulk system, this usually amounts to a constant additive correction.

2.2.3 Electrostatic contribution

In addition to the van der Waals short-range term, there is an electrostatic contribution to the potential energy, derived from the interaction between electrically charged particles

in the system. This is the Coulomb equation for electrostatic interactions and is modeled as:

$$\phi_{el} = \sum_i \sum_{j>i} \frac{q_i q_j}{4\pi\varepsilon_0 \boldsymbol{r}_{ij}}, \tag{2.28}$$

where q_i is the charge of particle i, and $\boldsymbol{r}_{ij}$ is the distance between particle i and j. Consequently, we can write the total interaction potential $V(r)$ between two atomic sites through the sum between LJ and Coulomb terms:

$$V(\boldsymbol{r}) = \phi_{LJ} + \phi_{el}. \tag{2.29}$$

Unlike the van der Waals interactions, the Coulomb term cannot be ignored at long distances. Straightforward spherical truncation of the potential, as done for the LJ case, would lead the ions to migrate back and forth across the spherical surface, creating artificial effects at the boundary. Through the decades, plenty of methods has been developed to address this problem, such as the Ewald sum, which includes the interaction of an ion or molecule with all its periodic images. For interacting ions i and j the potential energy can be written as

$$V = \frac{1}{2} \sum_{\boldsymbol{n}} \left(\sum_{i,j} \frac{q_i q_j}{|\boldsymbol{r}_{ij} + \boldsymbol{n}|} \right). \tag{2.30}$$

For simplicity of notation, the factor $4\pi\varepsilon_0$ have been omitted. The sum over $\boldsymbol{n}$ is the sum over all simple cubic lattice points, $\boldsymbol{n}$=($\boldsymbol{n}_x L, \boldsymbol{n}_y L, \boldsymbol{n}_z L$) with $\boldsymbol{n}_x, \boldsymbol{n}_y, \boldsymbol{n}_z$ integers. This vector reflects the shape of the basic box. For long-range potentials, this sum is conditionally convergent − the result depends on the order in which we add up the terms. As we add further terms to the sum, we are building up our infinite system in roughly spherical layers. When we adopt this approach, we must specify the nature of the medium surrounding the sphere, in particular its relative permittivity ε. The results for a sphere surrounded by a good conductor ($\varepsilon = \infty$) and by vacuum ($\varepsilon = 1$) are different:

$$V_{(\varepsilon=\infty)} = V_{(\varepsilon=1)} - \frac{2\pi}{3L^3} \left| \sum_i q_i \boldsymbol{r}_i \right|^2. \tag{2.31}$$

This equation can be applied in the limit of a very large sphere of boxes. In the vacuum, the sphere has a dipolar layer on its surface, which is canceled by the last term in Equation 2.31.

At any point during the simulation, the distribution of charges in the central cell constitutes the unit cell for a neutral lattice which extends throughout space. In the Ewald method, each point charge is surrounded by a charge distribution of equal magnitude and opposite sign, which spreads out radially from the charge. This distribution is conveniently taken to be Gaussian

$$\rho_i(\boldsymbol{r}) = q_i\mu^3 \exp\left[\frac{-\mu^2\boldsymbol{r}^2}{\pi^{3/2}}\right] \tag{2.32}$$

where the arbitrary parameter μ determines the width of the distribution, and $\boldsymbol{r}$ is the position relative to the centre of the distribution. This extra distribution acts like an ionic atmosphere, to screen the interaction between neighboring charges. The screened interactions are now short-ranged, and the total screened potential is calculated by summing over all the molecules in the central cube and all their images in the real space lattice of image boxes.

A charge distribution of the same sign as the original charge, and the same shape as the distribution $\rho_i(\boldsymbol{r})$ is also added. This canceling distribution reduces the overall potential to that due to the original set of charges. The canceling distribution is summed in reciprocal space. In other words, Fourier transforms of the canceling distributions (one for each original charge) are added, and the total transformed back into real space. At this point, the self-interaction of the canceling distribution must be subtracted. Thus, the final potential energy will contain a real space sum plus a reciprocal space sum minus a self-term plus the surface term:

$$\begin{aligned} V_{(\varepsilon=1)} = \frac{1}{2}\sum_{i,j}\left(\sum_{\boldsymbol{n}} q_i q_j \frac{\operatorname{erfc}(\mu\,|\boldsymbol{r}_{ij}+\boldsymbol{n}|)}{|\boldsymbol{r}_{ij}+\boldsymbol{n}|}\right) \\ + \frac{1}{\pi L^3}\sum_{i,j}\left(\sum_{\boldsymbol{k}} q_i q_j \left(\frac{4\pi^2}{k^2}\right) \exp\left(\frac{-k^2}{4\mu^2}\right)\cos\left(\boldsymbol{k}\cdot\boldsymbol{r}_{ij}\right)\right) \\ - \left(\frac{\mu}{\pi^{1/2}}\right)\sum_i q_i + \frac{2\pi}{3L^3}\sum_i |q_i\boldsymbol{r}_i|^2 \end{aligned} \tag{2.33}$$

where $\operatorname{erfc}(x)$ is the complementary error function ($\operatorname{erfc}(x) = [2/\sqrt{\pi}]\int \exp[-t^2]\,dt$) which falls to zero with increasing x. Thus, if μ is chosen to be large enough, the only term which contributes to the sum in real space is that with $\boldsymbol{n} = 0$, and so the first term reduces to the normal minimum image convention. The second term is a sum over reciprocal vectors $\boldsymbol{k} = 2\pi\boldsymbol{n}/L^2$. A large value of μ corresponds to a sharp distribution of charge, so that we need to include many terms in the k-space summation to model it. In a simulation, the

aim is to choose a value of μ and a sufficient number of k-vectors, so that Equations 2.33 and 2.31 give the same energy for typical liquid configurations.

Another important technique to solve the long-range force is the particle-particle particle-mesh (PPPM) algorithm for ionic systems [52]. In common with the Ewald method, this algorithm separates the total force on ion i into a long-range and short-range part. The short-part of the potential is handled normally (Equation 2.28). The total long-range part of the force on i is calculated using the particle-mesh technique. There are three distinct steps:

1. The charge density in the fluid is approximated by assigning charges to a finely-spaced mesh in the simulation box.

2. The fast Fourier transform (FFT) technique is used to solve Poisson's equation for the electrostatic potential due to the charge distribution on the mesh. This gives the potential at each mesh point.

3. The field at each mesh point is calculated by numerically differentiating the potential, and then the force on a particular particle i is calculated from the mesh field by interpolation.

This method has the advantage over the Ewald method of taking a time $\varphi(N)$ at large N rather than $\varphi(N^2)$ [53], which is particularly useful in the study of large systems.

2.2.4 Periodic boundary conditions

Originally, MD simulations were designed to access at molecular level the macroscopic properties of a sample. Today, however, the number of degrees of freedom that can be conveniently handled by computer simulations ranges from a few hundred to a few million. Most of simulations probe structural and thermodynamical properties of systems with up to a few thousand particles. Clearly, this number is still far removed from the thermodynamic limit. To be more precise, for such small systems it cannot be safely assumed that the choice of the boundary conditions has a negligible effect on the properties of the system. In fact, in an isolated three-dimensional system of N particles, the fraction of molecules that undergo surface effects is proportional to $N^{-1/3}$ [54].

In order to simulate bulk phases it is essential to choose boundary conditions that mimic the presence of an infinite bulk surrounding the N-particle model system. This is usually achieved by employing periodic boundary conditions. The volume containing the N particles is treated as the primitive cell of an infinite periodic lattice of identical

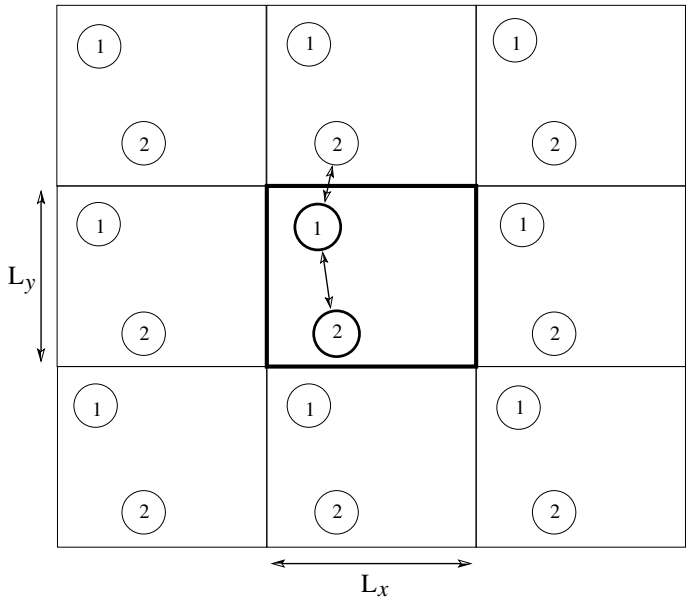

Figure 2.2: Schematic representation of periodic boundary conditions.

cells, as shown in Figure 2.2. A given particle i now interacts with all other particles in this infinite periodic system; that is, all other particles in the same periodic cell and all particles (including its own periodic image) in all other cells. For instance, if we assume that all intermolecular interactions are pairwise additive, then the total potential energy of the N particles in any one periodic box is

$$U_{tot} = \frac{1}{2} \sum_{i,j,\boldsymbol{n}} V\left(|\boldsymbol{r}_{ij} + \boldsymbol{n}L|\right), \tag{2.34}$$

where L is the diameter of the periodic box (assumed cubic) and $\boldsymbol{n}$ is an arbitrary vector of three integer numbers. By implementing the sum, the term with $i = j$ should be excluded when $\boldsymbol{n} = 0$.

2.2.5 Equations of motion

Now that the interacting potential is set, we turn our attention to the techniques used to solve the classical equations of motion for a system of N particles interacting via a potential V. These equations may be written down as the Lagrangian equation of motion:

$$\frac{\mathrm{d}}{\mathrm{d}t}\left(\frac{\partial L}{\partial \dot{q}}\right) - \frac{\partial L}{\partial q} = 0, \tag{2.35}$$

where the Lagrangian function $L(q,\dot{q})$ is defined in terms of kinetic and potential energies ($L = K - V$). If we consider a system of atoms, with Cartesian coordinates $\boldsymbol{r}_i$ and the usual definitions of K and V then Equation 2.35 becomes:

$$m_i \ddot{\boldsymbol{r}}_i = \boldsymbol{f}_i, \tag{2.36}$$

where m_i is the mass of atom i and $\boldsymbol{f}_i = \nabla L = -\nabla V$ is the force on that atom.

The most widely used method of integrating the equations of motion is that initially adopted by Verlet [55]. This method is a direct solution of the second-order equations of motion. If the centre of mass of the particle i at time t is $\boldsymbol{r}_i(t)$, at $t \pm \delta t$ we can expand the positions in a Taylor series:

$$\boldsymbol{r}_i\left(t+\delta t\right) = \boldsymbol{r}_i\left(t\right) + \dot{\boldsymbol{r}}_i\left(t\right)\delta t + \ddot{\boldsymbol{r}}_i\left(t\right)\frac{\delta t^2}{2!} + ... \tag{2.37}$$

$$\boldsymbol{r}_i\left(t-\delta t\right) = \boldsymbol{r}_i\left(t\right) - \dot{\boldsymbol{r}}_i\left(t\right)\delta t + \ddot{\boldsymbol{r}}_i\left(t\right)\frac{\delta t^2}{2!} + ... \tag{2.38}$$

where δt must be smaller than half of the collision time between the particles. Combining the above equations leads to:

$$\boldsymbol{r}_i\left(t+\delta t\right) \simeq -\boldsymbol{r}_i\left(t-\delta t\right) + 2\boldsymbol{r}_i\left(t\right) + \frac{\boldsymbol{f}_i}{m}\delta t^2. \tag{2.39}$$

The velocities have been eliminated by addition of the equations obtained by Taylor expansion about $\boldsymbol{r}_i(t)$. They are not needed to compute the trajectories, but they are useful for estimating the kinetic energy (and hence the total energy). They may be obtained from:

$$\dot{\boldsymbol{r}}_i\left(t\right) \simeq \frac{1}{2\delta t}\left[\boldsymbol{r}_i\left(t+\delta t\right) - \boldsymbol{r}_i\left(t-\delta t\right)\right]. \tag{2.40}$$

Whereas Equation 2.39 is correct except for errors of order δt^4 (the local error) the velocities from Equation 2.40 are subject to errors of order δt^2. An observation regarding Verlet algorithm is that it is properly centred ($\boldsymbol{r}(t-\delta t)$ and $\boldsymbol{r}(t+\delta t)$ play symmetrical roles in Equation 2.39), making it time-reversible.

Finally, we assume that we know the current and former positions of the particles, then we find the accelerations through $\boldsymbol{f}_i$ and determine the future positions. The overall scheme is illustrated in Figure 2.3.

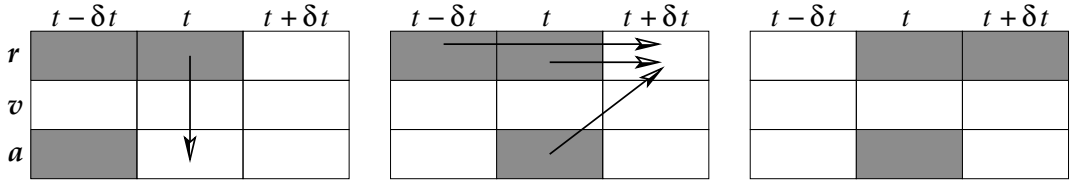

Figure 2.3: Schematic representation of the successive steps in the implementation of Verlet algorithm. In each case, the stored variables are in grey boxes. $\boldsymbol{r}$ stands for particles position, $\boldsymbol{v}$ for velocities and $\boldsymbol{a}$ for acceleration. Adapted from [53].

2.2.6 MD machinery

We have used MD simulations as implemented in the LAMMPS package [56] to analyze all the systems studied in this work. Additionally, we used the Verlet algorithm for the position integration. The PPPM method were chosen as the default algorithm for treat Coulomb interactions. Due to the system peculiarities, different *ensembles* were used: the NPT *ensemble* was used to simulate the passage of salty water through 2D nanoporous membranes, while water confined in nanotubes was simulated in the NVT *ensemble*. The reason is simple, while the size of the nanotube was kept fixed throughout the simulations, for water and nanopore systems this is not the case, and we had to consider an *ensemble* where the volume was function of hydrostatic pressure.

In the next section the simulational methods presented in this chapter are applied to two distinct systems in which water is confined.

Chapter 3

Water transport through nanotubes

In this chapter we study the behavior of water when confined in functionalized carbon nanotubes. The flow through hydrophobic and hydrophhylic nanotubes are compared.

3.1 Introduction

The research on mass transport at nanoscale through materials with nanochannels or nanopores has become an emerging area. Indeed, nanofluidics is one of the remaining virgin territories in fluid transport, in spite of hydrodynamics being a very old and established domain, where new mechanisms and phenomena are yet to be discovered.

In the past few years, the activity around nanofluidics has strongly increased with a number of groups developing even more ingenious tricks to fabricate nanoscale fluidic systems as well as new experimental tools to probe the behavior of fluids in such ultra-confined environments. But the extension to the nanoscale remains by no means an easy task.

The expectations lie in the belief that nanofluidics is not just an extension of the classical hydrodynamics and new specific behavior will emerge on the nanoscale. Otherwise, the idea that decreasing the scales would increase the efficiency of the processes is very tempting. Particularly, nanofluidics embraces a range of scales (with some arbitrariness) between 1 and 100 nm, thus including the smallest scale at which a fluid can conceivably be driven[1].

A current challenge is the design of individual fluidic channels on the nanoscale, with dedicated geometrical or chemical specificities, leading to different water-wall interactions. The good news is that, despite the emergence of strong quantum "coupling" for electronic

[1]The range of scales between 100 nm and 1 μm is sometimes called "extended nanofluidics" [57]

transport at nanoscale, quantum effects are not expected to couple easily to the flow and fluidic transport. In fact, the specificity of nanofluidics is not to host quantum effects but rather to host a broad spectrum of nanometric forces that work at controlling the fluid behavior [3]. At such scale many mechanisms are present, like van der Waals forces, electrokinetic effects and nucleation phenomena.

There is an overcrowding of players acting on the nanofluidic scale. In regular fluid dynamics, the only scale that matters is the system size, so that flow phenomena are fully controlled by the geometry. In nanofluidics, the spatial structure of the forces acting on the nanoscale must be fully taken into account to understand how fluids behave. This induces a level of complexity that contrasts with classical hydrodynamics, but, on the other hand, by combining different contributions, this may give birth to new outstanding physical effects. Today, the search for new coupling between them, or between them and the interfaces, that could allow one to drive and manipulate fluids in an unprecedented manner is just at its beginning. Discovering and harvesting such new mechanisms is the main goal of nanoscaled fluid dynamics.

Most − if not all − of the biological processes involving fluids do operate within pores of nanoscopic dimensions or less (ionic channels and transmembrane proteins, e.g. aquaporins [14]). Nature has optimized its process by scaling down the fluidic phenomena. This has actually motivated a huge amount of studies in the physiology domain. Understanding how these systems work would provide new solutions for important technological questions. This is the case for example, as we will see next, of desalination and separation.

3.2 Nanotube functionalization: Tuning the hydrophobicity

Carbon nanotubes (CNTs) and graphene have attracted significant attention from all around the world due to the emergence of novel mass-transport properties in relation to their perfect structure of sp^2 hybridized carbon atoms arranged within a honeycomb like lattice. Well-aligned CNTs can serve as robust pores in membranes for water desalination, decontamination and energy applications [26]. The smooth and hydrophobic inner core of the hollow CNTs can allow the uninterrupted and spontaneous passage of water molecules with very little absorption.

Recent advances in the development of reliable methods for the chemical functionalization of the nanotubes has increased the motivation towards extending the scope of their application spectrum. In particular, covalent modification schemes allow persistent

alteration of the electronic properties of the tubes, as well as to chemically tailor their surface properties, whereby new functions can be implemented that cannot otherwise be acquired by pristine nanotubes. CNTs functionalized in this way are soluble in many organic solvents, once the CNT hydrophobic nature is changed to hydrophilic due to the attachment of polar groups. The chemically functionalized CNTs can produce strong interfacial bonds with many polymers, allowing CNT-based nanocomposites to possess high mechanical and functional properties [58].

Non-covalent functionalization is an alternative method for tuning the interfacial properties of nanotubes. The suspension of CNTs in the presence of polymers, lead to the wrapping of polymer around the CNTs to form supermolecular complexes of CNTs, which alter the nanotube wall interactions and consequently their polarity. Inorganic nanoparticles (such as C_{60}, Ag, Au and Pt [59]) can be inserted at defect sites localized at the ends or on the sidewalls of the tube. Small biomolecules, such as proteins and DNA, can also be entrapped in the inner hollow channel of nanotubes by simple adsorption, forming natural nano-test tubes [60]. The combination of these materials is particularly useful in the development of hybrid channels for use in nanotechnology and molecular scale devices.

Recent studies have highlighted the possibility of modify CNT pores by functionalization processes to selectively sense and reject ions [61, 62]. Thus, functionalized CNT membranes can be used as "gate keeper" for size controlled separation of multiple pollutants, though it has antifouling, self-cleaning and reusable functions. Additionally, molecular simulation studies to understand the frictionless movement of water molecules through CNT nanochannels, membrane fabrication, functionalization and influencing factors have been extensively presented. Next we present some applications related to functionalized nanotubes.

Desalination

Nanotube-based membrane performances often rely on its processing and fabrication methods. The vertically aligned (VA) CNT membranes are synthesized by arranging perpendicular CNTs with supportive filler contents between the tubes. These membranes are high molecular sieves with intercalated filler matrix such as polymer between them. The fillers may be epoxy, silicon nitride and others with no water permeability. It has been shown that *biotin* and *streptavidin* attachment onto the functionalized CNT membranes reduced ion transport by 5-15 times [65]. Such functionalized membranes work as gate-keeper controlled chemical separators or an ion-channel mimetic sensor. Holt et al. [66] have incorporated silicon nitride (Si_3N_4) fillers between the nanotube spaces to inhibit

water flow between the nanotube gaps and create stress to stimulate water flow through the tube. The water flux was increased by more than 3 folds over other no-slip hydrodynamic flow, and presented enhanced ion selectivity compared to regular multi-walled CNT membranes. Additionally, such membrane engineering can provide high selectivity with low energy consumption.

Recently, Lee and his group [67] has used densified outer-wall CNT membrane to deliver a water purification capacity of 30,000 l/m^2·h at 1 bar, which is almost two orders of magnitude greater than that attainable using traditional polymer membranes. Yang et al. [63] have also demonstrated functionalized nanotubes to exhibit ultrahigh specific adsorption capacity for salt (exceeding 400% by weight) that is two orders of magnitude higher than that found in the current state-of-the-art activated carbon-based water treatment systems. Nanopore functionalization eventually modify the water-wall interaction, leading to new and improved water transport capability. This is particularly important for desalination process where water molecules would be attracted to the tube inner instead of ions. In Figure 3.1 we show some experimental setups and computational studies of water desalination using functionalized nanotubes.

Water treatment

Functionalization of CNT membranes is often a precondition for CNT-based water purification. Pristine CNTs often aggregate which significantly decreases water flux and pollutant rejection capacities of the membranes. CNTs are generally contaminated with metal catalysts, impurities and physical heterogeneities [68]. Additionally, CNTs are capped

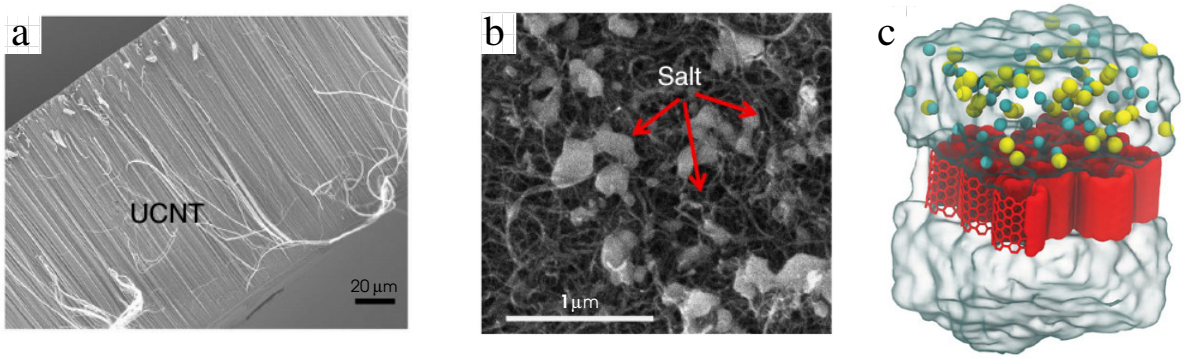

Figure 3.1: (a) Cross-sectional SEM image of pristine CNT membranes. (b) SEM image of sample CNT membranes after the adsorption reaches saturation. Adapted from [63]. (c) Angled view of simulation with CNT membranes for water-ion separation. Adapted from [64].

into hemisphere like fullerene type curvature during synthesis and purification [69]. These capped CNTs are unzipped into open tips which could be oxidized into specific functional groups to trap selective pollutants. Functionalization can add positive (-NH_3^+), negative (-COO^-, sulfonic acids) and hydrophobic (aromatic rings) groups on CNT surfaces [70]. These make CNT membranes selective for particular pollutant retention and increase water influx through the nanotube hole.

Functionalized nanotube membranes has shown good water permeability, mechanical and thermal stability, fouling resistance, pollutant degradation and self-cleaning functions [67, 63]. Tip functionalized CNT membranes have selective functional groups on the nanotube mouth and the core functionalized CNT have functionalities at the sidewall or interior core. Both types demonstrate increase water fluxing and selective rejection of pollutant. Majumder and Corry [71] has found that progressive hydrophilic modification in the nanopore walls can significantly affect the water influx, with consequences for nanofluidic devices.

Functionalization also decreases energy consumption through increased permeability and physical adjustability [70]. CNT membranes can be decorated with various nanoparticles such as Cu, Ag, Au, Pt, Pd, TiO_2, polymers, and biomolecules (pollutant degradative enzymes, DNA and proteins) which have attractive membrane properties and thus broadening functionalized CNT membrane applications − as in molecular sieves.

Energy applications

Whether the fast flow (mechanical energy) of water or polar liquids in functionalized nanocavities can be converted into electrical energy is an extremely interesting subject.

The potential electric current and voltage generation in graphitic materials immersed in flowing liquids was first predicted theoretically in 2001 by Král and Shapiro for metallic carbon nanotubes [72]. Since then, many experiments have reported the voltage generation phenomena. The main driven mechanism was found to be the direct scattering of the free carriers by the fluctuating Coulombic fields of the flowing molecules and ions in the liquid. Ghosh et al. [73] reported experimentally an induced voltage of 2.7 mV for pure water flowing at 1.8 mm s^{-1} outside single-walled carbon nanotube bundles. The addition of ions (1.2 M HCl solution) has lead to fourfold induced voltage. A significant dependence of the induced voltage on the flow velocity suggested that the fast flow of water (and other liquids) along the hydrophobic surface is the key component of the energy harvesting through the graphitic nanofluidics. Liu et al. [74] have shown that multiwalled CNTs vertically aligned along the flow direction produced ∼30 mV in aqueous solution

of 1 M NaCl at a flow velocity of 0.5 mm s^{-1}. Again, nonlinear voltage-velocity response was observed.

Notably, experiments have demonstrated that tuning the polarity of the nanopore by decorating its surface or applying electric fields along the tube axis leads to enhanced voltage generation and improved conversion efficiency. S. H. Lee and his colleagues [1] has shown that voltage generated by semiconducting nanotubes was three times greater than that for metallic nanotubes, meanwhile that the pore polarity is a crucial ingredient in the energy generation through nanofluidics. Recently, Kim and his group [2] has generated networks and carbonization between individualized single-walled carbon nanotubes (SWCNTs) by an optimized plasmonic heating process using a halogen lamp to improve electrical properties for flow-induced energy harvesting. The electrical sheet resistance of carbonized SWCNTs was decreased to 2.71 kΩ, 2.5 times smaller than normal-SWCNTs, leading the carbonized-SWCNTs to present a generated voltage and current 9.5 and 23.5 times larger than for the normal-SWCNTs. All of this results brings up the amazing possibilities that nanopore functionalization can add to nanofluidic devices. In fact, controlling the pore polarity has several consequences to the water mobility through the inner of the nanotube, as we will see next.

3.3 Water structure and dynamics inside functionalized nanotubes

Water in well characterized pores can serve as model systems for the study of inhomogeneous water, ubiquitous in biological and geological systems. It has been extensively shown that confined or interfacial water is highly relevant to properties and functions of entire systems (e.g., ion channels, clay minerals, transmembrane proteins [14, 3]).

X-ray diffraction [18], neutron scattering [75] and NMR studies [76] have shown that water can fill the inner space of CNTs at ambient conditions and freezes into crystalline solids often referred to as "ice nanotubes". The ice structures are characterized as stacked n-membered rings or equivalently as a rolled square-net sheet [19]. Regarding the structure assumed by confined water, many aspects are still unclear. Of the properties of water inside nanopores, a fundamental yet little known aspect is a global picture of the phase behavior. There are recent evidences that, inside isolated small CNTs (1.25 nm in diameter), both low and high-density liquid water states can be detected near ambient temperature and above ambient pressure [77]. In the temperature-pressure phase diagram, the low- and high-density liquid water phases are separated by an hexagonal ice nanotube phase.

When the pressure is increased from 10 to 600 MPa along the 280 K isotherm, the water can undergo low-density liquid to high-density liquid reentrant first-order transitions.

It has been reported that water-CNT systems exhibit hydrophobic/hydrophilic behavior depending on the temperature and CNT diameter. CNTs adsorb water molecules spontaneously in their cylindrical pores around room temperature, whereas they exhibit a hydrophilic-hydrophobic transition or wet-dry transition (WDT) at a critical temperature $T_{WD} \sim$ 220-230 K and above a critical diameter $D_{WD} \sim$ 1.4-1.6 nm [78]. However, details of the WDT phenomenon and its mechanism remain unknown. In a recent X-ray diffraction study, it was shown that water molecules inside thick CNTs ($D > D_{WD}$) evaporate and condense into ice Ih outside the tube at T_{WD} upon cooling, and the ice Ih evaporates and condenses inside the CNT upon heating [79]. On the other hand, residual water trapped inside the CNT below T_{WD} freezes. Molecular dynamics simulations indicate that upon lowering T, the hydrophobicity of thick CNTs increases without any structural transition, while the water inside thin SWCNTs ($D < D_{WD}$) exhibits a structural transition, forming an ordered ice. The unusual diameter dependence of the WDT was attributed to the adaptability of the structure of water to the pore dimension and shape. Hydrophobic-hydrophilic transition has been also reported upon cooling from 295 to 280 K via the observation of water adsorption isotherms in CNTs measured by NMR [80]. The observed transition demonstrates that the structure of interfacial water could depend sensitively on temperature, which could lead to intriguing temperature dependencies involving interfacial water on hydrophobic surfaces. An illustrative depiction of the phase behavior (temperature *versus* nanotube diameter) of water trapped in nanotubes is shown in Figure 3.2.

Understanding the fast transport of gas and water through nanotubes is of great importance to designing novel molecular devices, machines, and sensors. Inspired by the charges in the biological water channels (aquaporins), Gong et al. [81] proposed a molecular water pump by using a combination of charges positioned adjacent to a CNT. This molecular pump provides a possibility to develop water transport devices without an osmotic or hydrostatic pressure gradient. When the orientation of water molecules confined inside CNTs is maintained along one direction, a net flux along that direction can be attained due to the coupling between rotational and translational motions [16].

The boundary condition is a critical issue in nanoscaled systems. Several theoretical studies have demonstrated that a minute change in the attraction between the tube wall and water can dramatically affect pore hydration, leading to a sharp transition between empty and filled states within a nanosecond time scale [82, 83]. Recently, Kou et al. [49] has demonstrated unidirectional motion of water molecules created by a nonzero nanotube

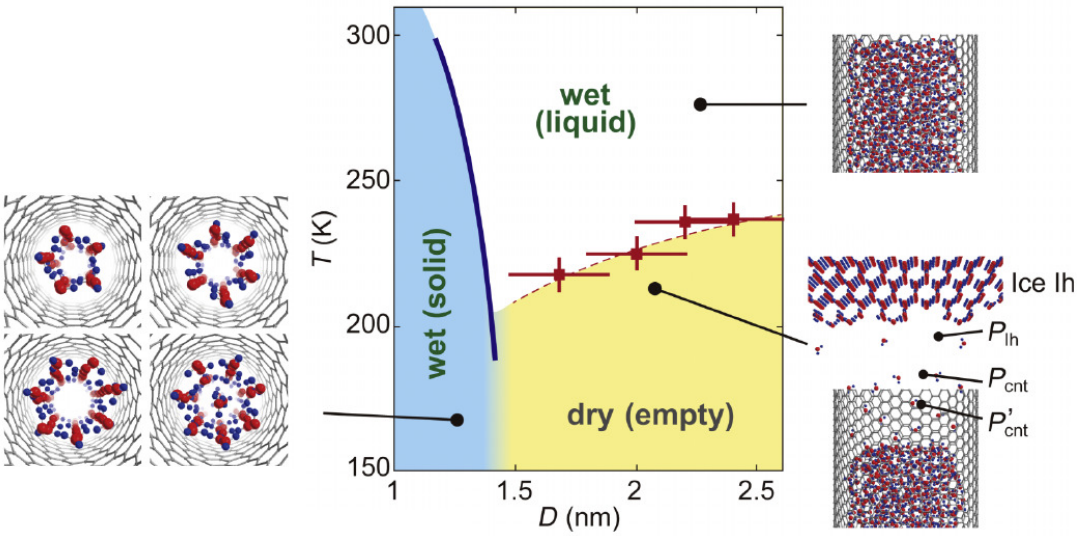

Figure 3.2: Schematic temperature-diameter (T-D) phase diagram for water-CNT system. Solid and dashed lines represent liquid-solid and wet-dry transition boundaries, respectively. Adapted from [79].

surface energy gradient. It was found that water moves along the direction of increasing surface energy, and that higher surface energy gradient promotes higher transportation efficiency. With a wavelike feature, the hydrogen bond network have been demonstrated to play an important role in the dynamic acceleration process.

The existence of confining structures in which hydrophobic and hydrophilic sites are present is not just a theoretical assumption. Recent methods allowed the synthesis of nanotubes similar to CNTs, boron-nitride nanotubes (BNNTs) [84] and carbon doped BNNTs [85]. Chemically functionalized nanotubes can have hydrophobic and hydrophilic characteristics, similar to biological channels, which have distinct solvophobic properties depending on the amino acids charge distribution. Computational investigations on the water properties inside such cylindrical structures with solvophilic and solvophobic behavior indicate distinct dependence of the overall mass flux for each species of fluid with the number of solvophilic sites for different nanotube radii [83]. Density and fluid structure are also found to be dependent on the nanotube radius and hydrophobicity [86, 17]. These results indicate that volumetric effects play an important role in the distinct dynamical and structural properties of fluids inside nanopores, mainly inside narrow nanopores, where the competition between the fluid-fluid and fluid-nanopore interactions are stronger and, therefore, distinct fluid-fluid interaction leads to distinct behaviors. There are a number of

works (including from our group) demonstrating that hydrophobicity plays a crucial role in the dynamics and structure assumed by water inside nanotubes [87, 88, 21, 89, 20, 90]. This ubiquitous characteristics has attracted our attention to the nanofluidic in functionalized nanotubes.

3.4 The effect of nanotube hydrophobicity on water transport and structuration

Transport properties of water confined inside hydrophobic and hydrophilic nanotubes were studied. Our focus was on nanopores with radii large enough to accommodate more than a single file of water, in order to determine the shear between liquid "layers". It allows us to account for water viscosity and diffusion.

We performed through molecular dynamics simulations two complementary analyzes of the diffusion of water in nanoconfinement. First using TIP4P/2005 water [91] confined in both hydrophobic and hydrophilic nanotube we show that, as illustrated in the Figure 3.3, the viscosity and the diffusion do not obey the Stokes-Einstein relation ($\eta \cdot D \propto T$) for hydrophobic nanotubes. In this confinement, the diffusion reaches a plateau while the viscosity increases abruptly. Interestingly, for the same range of densities the number of hydrogen bonds also reaches a limit, as illustrated in the Figure 3.4, thus establishing a relationship between the dynamics and the structure of the water molecules that leads to a breakdown of the Stokes-Einstein relation for water flow through narrow hydrophobic nanotubes. It is important to note that for wider nanotubes the nature of the wall plays no relevant role in the water mobility. The peculiar water behavior is observed only for

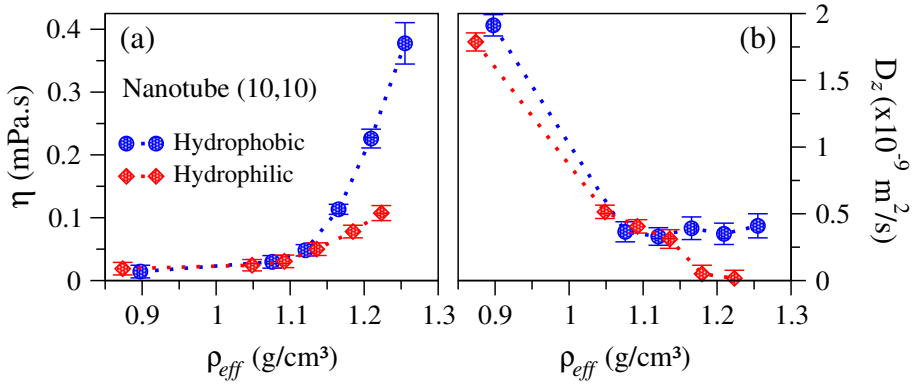

Figure 3.3: Left panel: Viscosity, η as a function of the water density. Right panel: Axial diffusion D_z as a function of density. Both panels are for 1.35 nm diameter nanotubes. From [17] (see appendix A for detail).

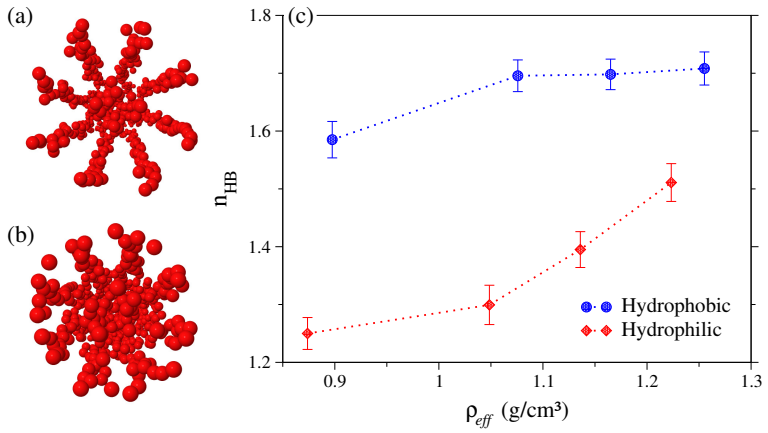

Figure 3.4: The snapshot of the last configuration for the (a) hydrophobic and the (b) hydrophilic (10,10) nanotube. For clarification, only the oxygen atoms are shown. In (c) we show the average number of hydrogen bonds per water molecule for the hydrophobic (blue) and the hydrophilic (red) confinement. From [17] (see appendix A for details).

the smaller nanotubes. The detailed presentation of this analysis is shown in the complete paper following the Appendix A.

In addition, we have implemented MD simulations to study a large variation in density of water confined in hydrophobic and hydrophilic tubes, going from 0.5 to 1.5 g/cm^3. Figure 3.5 shows the axial mean square displacement of water oxygen atoms. For high densities inside (10,10) tubes the mobility of water is higher for hydrophobic confinement, while in hydrophilic confinement water is almost immobile. This result indicates that the large flow observed in hydrophobic tubes is related to the high diffusion. We have also varied the density of water confined in these structures in order to evaluate water structural and dynamical changes. Importantly, For low densities ($\sim$ 0.5 g/cm^3) water present saturation in their diffusion along the simulation time, indicating the formation of "bubles". A detailed analysis is presented in the full paper that follows in Appendix B.

So far, we have been interested in nanotubes larger enough to accommodate more than one layer of water molecules, in order to calculate the associated shear viscosity. This have restricted us to nanotubes with diameters $d > 1.5$ nm. We now bring our attention to smaller nanotubes, where just one layer (single-file) of water is allowed due geometrical restrictions: nanotube diameters ranging from 0.8 to 1.0 nm. At this extreme confinement, water can present higher mobility (known as super-flux [82]) and several structural anomalies, such as tight hydrogen bond network and ice formation at ambient conditions [16].

Following, we have used MD simulations to investigate the diffusion characteristics

of water molecules confined in narrow nanotubes with variable polarity. The nanotubes were again built with hydrophilic or hydrophobic sites. The results shows that there is a strong relation between density and surface properties for the water structuration inside the nanotubes. At low densities and narrower nanotubes, the surface characteristics play a major role, whereas for wider nanotubes, we observe distinct structuration at higher densities. In Figure 3.6 we show the MSD along the simulation time for all nanotube samples. The density is found to profoundly affect the water mobility in both nanotube species. This effect is accompanied by an organization in layers, resulting in structural transitions of water inside the nanotube as we increase the density [93].

The temperature plays an important role in the transport and structure of water inside small nanotubes. Figure 3.7 show the radial density distribution of water along the nanotube radius. Curiously, our findings show that the structuration of water is more sensitive to temperature inside the (8,8) nanotubes than the (7,7) case. This could be associated with the squared-ice formation inside (8,8) nanotubes [94]. The results indicate how density, temperature, and surface properties affect the dynamical and structural behavior of water inside narrow nanopores. A detailed discussion can be found in the full paper that follows in Appendix C.

In summary in this chapter three complementary aspects of the behavior of confined water were explored. First, the difference between the viscosity of water inside hydrophobic and hydrophilic nanotubes as the density is increased. While in the first case, at high densities viscosity does not change with the density, for the hydrophilic case the water becomes imobile. This violation of the Stokes-Einstein relation can be understood in terms of the number of hydrogen bonds with becomes high and constant for hydrophobic tubes. Next, the mobility of water inside the hydrophobic and hydrophilic nanotubes

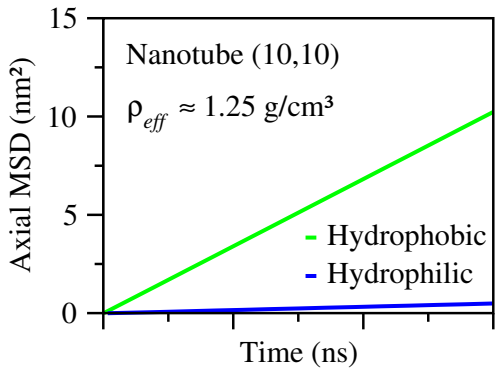

Figure 3.5: Time evolution of the mean square displacement of water oxygen atoms through hydrophobic and hydrophilic nanotubes for high density. From [92] (see appendix B for details).

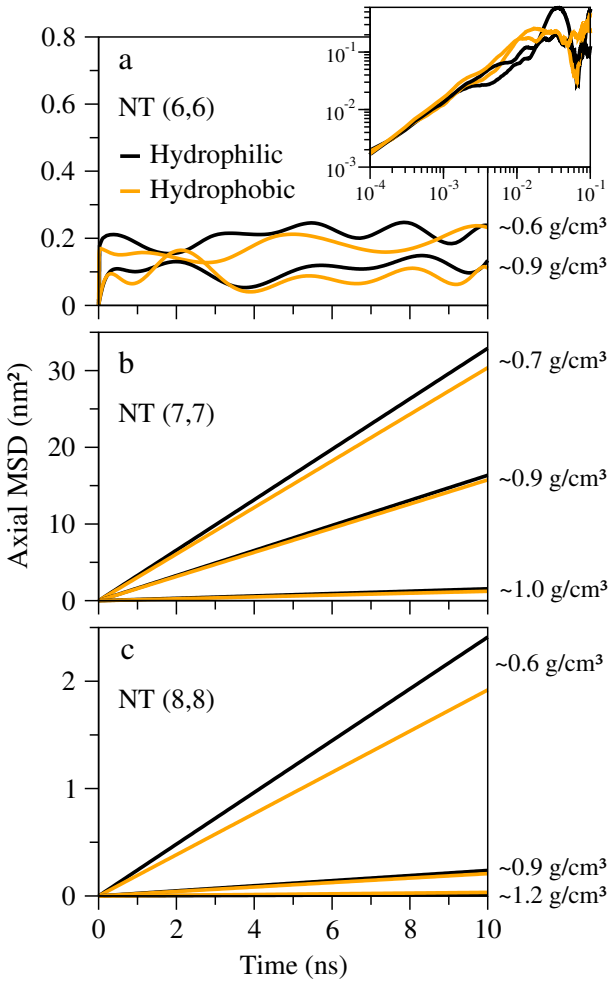

Figure 3.6: MSD *versus* time for (a) (6,6), (b) (7,7), and (c) (8,8) hydrophobic and hydrophilic nanotubes. From [93] (see appendix C for details).

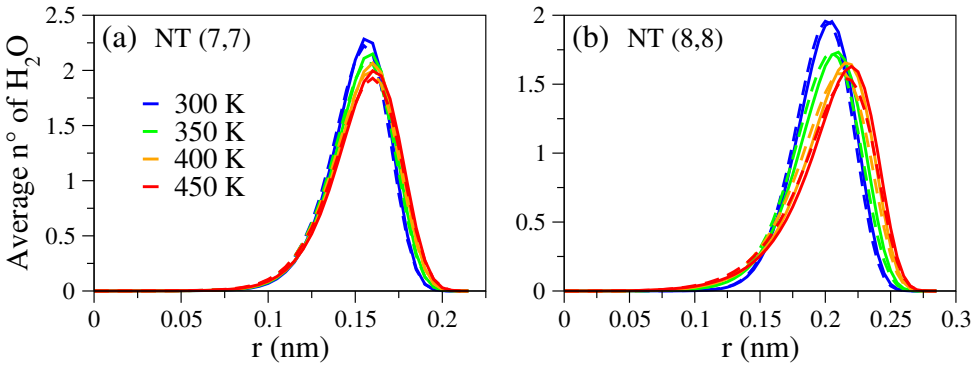

Figure 3.7: Oxygen's radial density profile inside (a) (7,7) and (b) (8,8) nanotubes at distinct temperatures. Solid lines stands for hydrophilic surfaces, whereas dashed lines for hydrophobic nanotubes. From [93] (see appendix C for details).

for different tubes diameters and densities are compared. We observed that only for (10,10) nanotubes and high densities large differences in diffusion and structure. Water at hydrophobic nanotubes are much more mobile when compared with hydrophilic tubes. Finally, the temperature effect on the diffusion of water in hydrophobic and hydrophilic tubes was studied. We observed that the temperature impacts (7,7) tubes in a linear way while the impact in (8,8) can be fitted in a cubic function. The results related to this chapter were published in references [17, 92, 93] and are presented in the appendixes A, B and C, respectively.

Chapter 4

Water transport and desalination through two-dimensional nanopores

In this chapter we study the water flux through different types of nanopores. Our analysis involved water in monovalent, multivalent solutions.

4.1 Introduction

Recently, researchers from the National Graphene Institute (NGI) at the University of Manchester fabricated slit devices from two 100-nm thick crystal slabs of graphite measuring several microns across obtained by shaving off bulk graphite crystals [95]. Rectangular-shaped pieces of 2D atomic crystals of bilayer graphene and monolayer molybdenum disulfide (MoS_2) were placed at each edge of one of the graphite crystal slabs before placing another slab on top of the first. This produces a gap between the slabs that has a height equal to the spacers' thickness. The assembly is held together by van der Waals forces and the slits are roughly the same size as the diameter of aquaporins, which form pores in the membrane of biological cells to facilitate transport of water between cells [13].

But why did the researchers spend so much time and energy to produce a graphene-based membrane with the smallest possible anthropogenically engineered holes?

It may seem unbelievable in 21st century, but several places on the planet still face problems with treatment and distribution of potable water. Extensive environmental pollution caused by worldwide industrialization and population growth has led to a water shortage, especially in underdeveloped countries [24]. This problem lowers the quality of human life and wastes a large amount of money worldwide each year due to the related consequences.

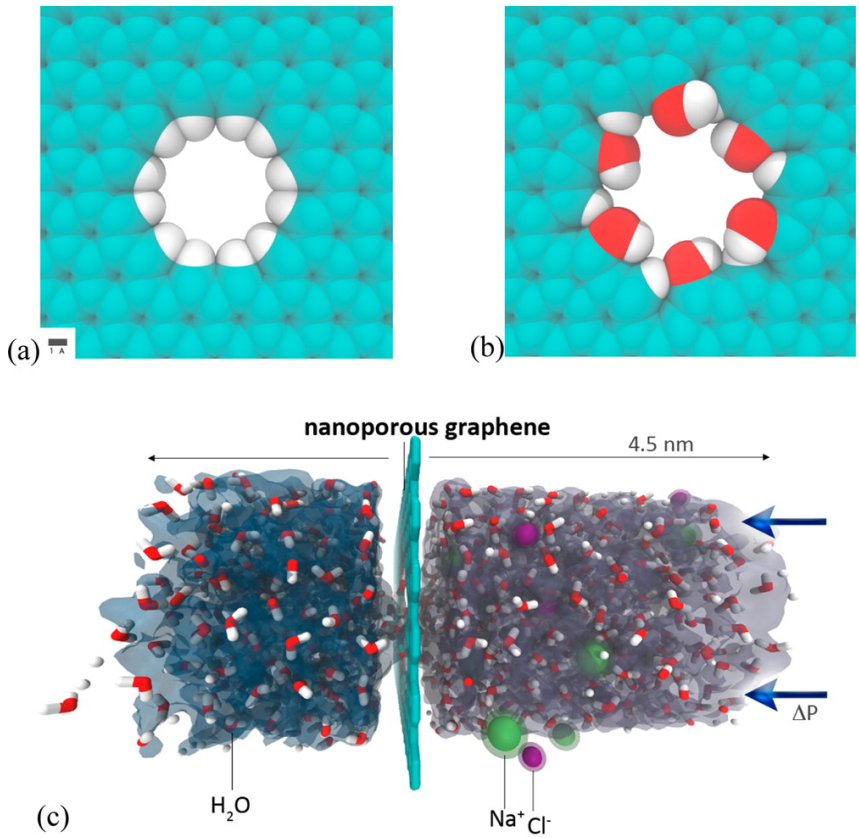

Figure 4.1: Hydrogenated (a) and hydroxylated (b) graphene pores, and (c) side view of a typical 2D nanoporous membrane for desalination. Adapted from [100].

One solution for this challenge is water purification. State-of-the-art water purification necessitates the implementation of novel materials and technologies that are cost and energy efficient. In this regard, graphene-related nanomaterials, with their unique physicochemical properties, are an optimum choice [96]. These materials offer extraordinarily high surface area, mechanical durability, atomic thickness, nanosized pores and reactivity toward polar and non-polar water pollutants [35]. These characteristics impart high selectivity and water permeability, and thus provide excellent water purification efficiency. Additionally, chemical functionalization of graphene nanopores, as shown in Figure 4.1, opens an avenue of new possibilities for enhanced ion rejection and water flux [97, 98, 99].

In the case of Manchester researchers [95], the slits made from graphene, hexagonal boron nitride and MoS_2 are several angstroms (0.1 nm) in size and allow ions with diameters larger than the size of the slit to permeate through. The idea is to trap ions inside nano-sheets of graphene or transition metal dichalcogenide monolayers to both clean water and generate energy. Ions flow through the slits with voltage application when immersed in an ionic solution, and this ion flow constitutes an electric current. Measurement of ionic

conductivity as ions passed through chloride solutions via the slits confirmed that ions could move through them as expected under an applied electric field. These mechanisms also contribute to the realization of high-flux water desalination membranes.

The fast nanotechnology developments have provided opportunities to design and fabricate novel and energy-efficient membranes for water filtration. There are plenty of works showing the promising capability of 2D materials to reject or trap ions in order to desalinate water. The most common approach is to drill a nanopore, as small as possible, in the surface of planar materials (e.g., graphene, h-BN or MoS_2) in order to press an ionic solution through the membrane, which is expected to separate water from salt. Graphene-derived 2D membranes are the most outstanding representatives in desalination that have been verified mainly by computer simulations followed by experimental evaluation. Besides nanoporous graphene, graphene oxyde, and graphyne, some other emerging novel 2D nanoporous membranes have also shown great potential in desalination, such as zeolite nanosheets and MoS_2 membranes.

4.2 Nanoporous molybdenum disulfide for water desalination

Series of mono- or few-layered 2D materials, such as hexagonal boron nitride (BN) [101] and MoS_2 [102], have attracted extensive attention in many areas including ionic sieving. MoS_2 is the most intriguing material to be used in fabricating nanoporous membranes with desalination potential, which owns equivalent speciality as graphene. MoS_2 is a kind of 2D nanoporous membrane with three-atom thickness. It consists of hexagonal arranged Mo atoms in one plane sandwiched between two planes of hexagonal arranged S atoms through covalent bonding. It was reported a Young's modulus as high as 300 GPa for MoS_2 nanoporous membrane with thickness of 1.0 nm [103], comparable to that of steel. Fabrication of defect-free MoS_2 nanoporous membranes mainly by means of CVD is possible. In some occasions (e.g., in the fabrication process by CVD), MoS_2 exhibits more stability than the graphene, since graphene is more susceptible to carbon contamination [104]. Finally, the crystallinity of MoS_2 nanoporous membranes could be significantly enhanced via modified CVD, ensuring more mechanical stability than that of graphene [105]. Using a highly focused electron beam, and transmission electron microscope, versatile nanopores with diameters ranging from subnanometer to 10 nm were sculpted successfully in MoS_2 membranes [106]. Feng et al. [107] have developed a scalable method to controllably make nanopores in single-layer MoS_2 with subnanometer

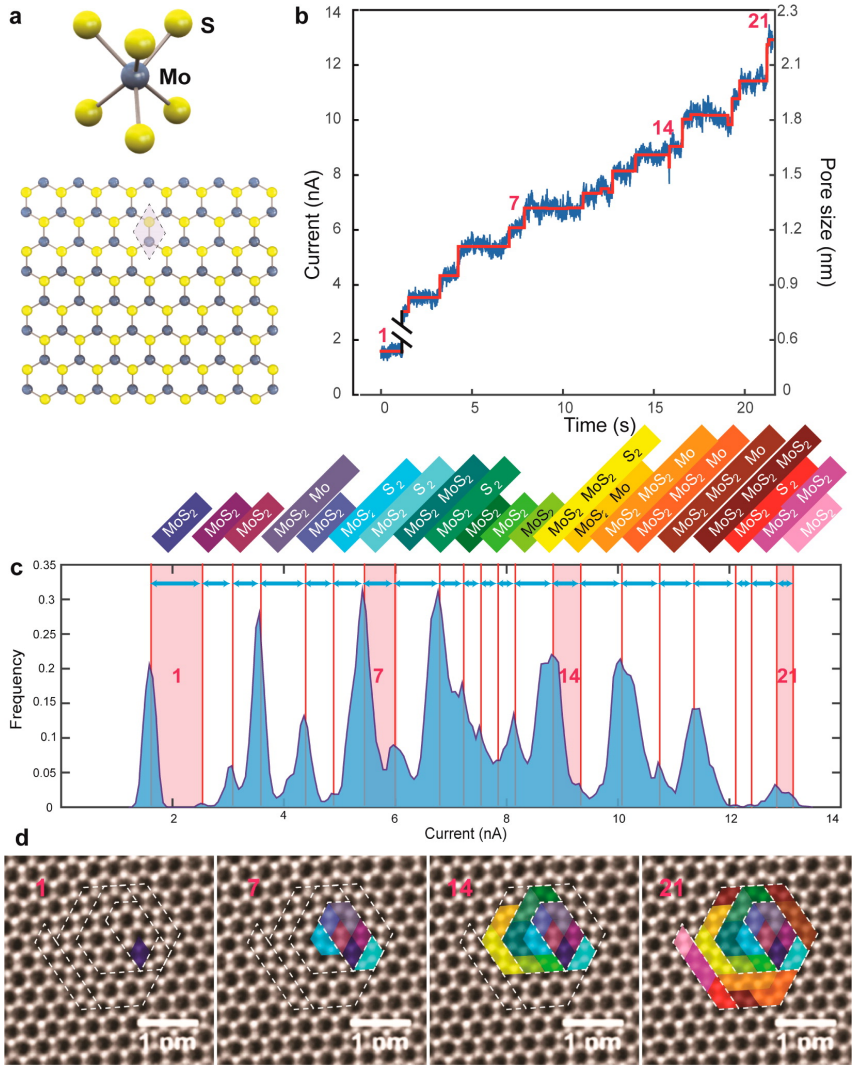

Figure 4.2: (a) Top view of a monolayer MoS_2 lattice. (b) Ionic current step-like features during the nanopore formation. (c) Trace histogram with corresponding color coded atom groups cleaved in each step during the pore formation. (d) Illustrative schematic for nanopore creation: Transmission Electron Microscope (TEM) micrograph of suspended single layer MoS_2 with superimposed polygons corresponding to atomic groups cleaved during the pore formation Adapted from [107].

precision using electrochemical reaction (ECR), as depicted in Figure 4.2. Fabrication of individual nanopores in hexagonal boron nitride (h-BN) with atomically precise control of the pore shape and size has been also reported [108]. Another challenge lies in accurately measure the size of the manufactured nanopore. Attempts have been made to extract this information from the material's conductance [109]. Recently, Wen and colleagues [110] have introduced the concept of effective transport length in order to accurate determines graphene and MoS_2 nanopore's diameter using conductance measurements.

Desalination ability of single-layer MoS_2 nanopores was first introduced by MD simulations, in which ion rejection rates of 88% were obtained for pores ranging from 20-60 $Å^2$ [38]. Water flux were also estimated to be of two to five orders higher than that of other nanoporous membranes and 70% higher than that of graphene. Markedly, the rejection of NaCl by MoS_2 nanoporous membranes was found to strongly depend on the pore chemistry and geometry. For instance, MoS_2 with pores containing only Mo and S exhibited highest and lowest water flux, respectively, while mixed pores provided intermediate rates of water flux [38]. Additionally, following a general trend for small nanochannels [111] the water flux through MoS2 have been shown to linearly depend on the external pressure.

The difference in permeability between MoS2 and graphene lies in $\sim 30\%$ (83.6 and 59.3 ns^{-1}, respectively), and the corresponding difference in the energy barrier for the water molecules to pass through the pore is $\sim 26\%$ (~ 8.5 and ~ 11 K_BT). The higher permeability coefficients and lower energy barrier of MoS_2 nanopores can be ascribed to three aspects. Firstly, the hydrophilic nature of Mo sites with contact angle of near 0∘ along the edge of pore had more attraction for the water molecules to the pore interior [112]. Secondly, the arrangement of Mo and S sites in the pores provide enhanced velocity of water molecules close to the Mo sites. Finally, the geometry of pores with only Mo at the edge could be the most important factor for the high flux. It has been reported that the conical pores always contribute to the high permeations [113, 114]. Many nanomaterials with nanopores, such as aquaporin, display pores with hourglass shape, which facilitates the fast water transport [14, 115]. The geometry structure of pores with Mo and S only at the edge, and the graphene pores are shown in Figure 4.3. Similarly, the fish-bone structure made the pores with only Mo at the edge distorted to an hourglass shape. In the pores with only Mo at the edge, water molecules slip along the hydrophobic S sites and are attracted by the Mo sites at the center. This arrangement could significantly enhance the water flux.

If we make the nanopore small enough (~ 20 Å in diameter) MoS_2 demonstrate ionic rejection of almost 100% [38]. Increasing the pores would enhance the water permeability but compensate the salt ions due to the existence of trade-off between the water flux and salt rejections. In summary, thanks to the conical geometry and nozzle-like pores with sizes < 1 nm, combined with the interior hydrophilicity of Mo and exterior hydrophobicity of S, the unique fish-bone pore structures of MoS_2 nanoporous membrane contribute to an excellent desalination performance. However, it is important to note that we still depends on the nanopore size, since larger nanopores leads to poor ionic rejection. As we will show later, this issue could be addressed by adding some flocculant ingredient to the solution, in order to induce ionic clusterization. This would avoid ionic passage through

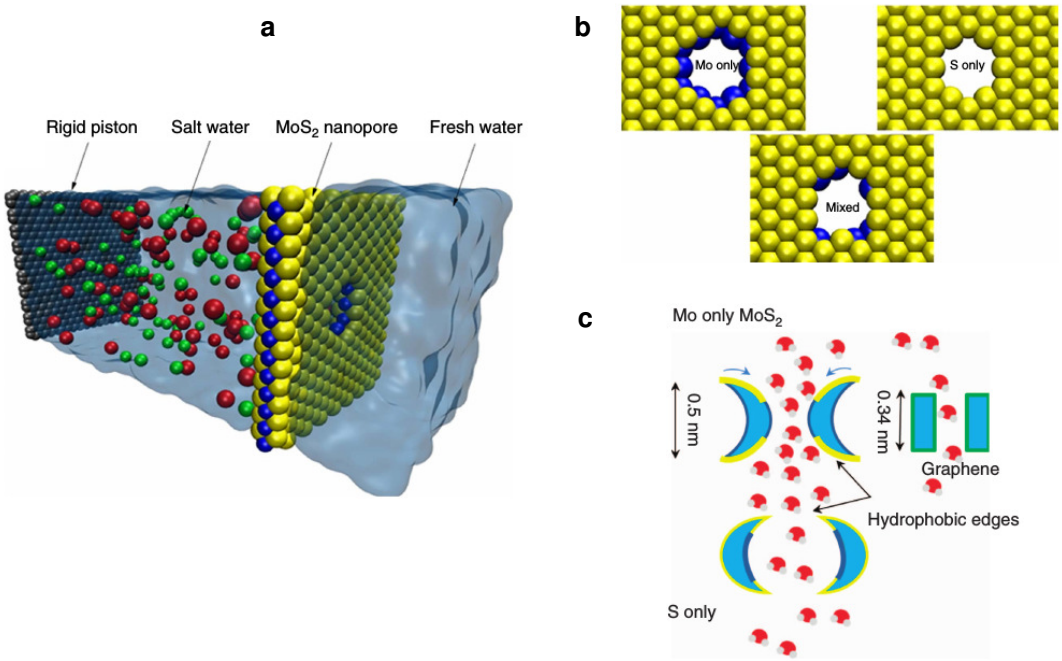

Figure 4.3: (a) Schematic illustration for the water desalination through MoS_2 nanoporous membranes, (b) three pores of MoS_2 and (c) their architectures representation compared with graphene nanopore. Adapted from [38].

the nanopore due to geometrical restrictions.

Another interesting feature of MoS_2 membranes is its "flexibility" in the in-plane direction. The Young's modulus of MoS_2 monolayer (270 GPa) is much smaller than that of graphene (2 TPa) [116], which would be explored through mechanical strain to access tunable pore diameters. By applying 12% strain on MoS_2 nanopores, Li et al. [117] have found a water flux of 100 g/(m^2·s·atm) with pore density of $1.0 \times 10^{13}/cm^2$, considerably higher than that found in graphene, 70 g/(m^2·s·atm), and orders of magnitude higher than that of commercial RO membrane, 1.18 g/(m^2·s·atm). The authors also found a higher energy barrier at the pore's edge for Na^+ (20 kJ/mol) and Cl^- (9 kJ/mol) atoms compared with water (5 kJ/mol), which means a further repulsion of ions by MoS_2 nanopores.

Mo- or S-terminated nanopores presents irregular shapes and dimensions. Recently, Kou et al. [118] have studied triangular MoS_2 nanopores via MD simulations. Remarkably, they found formation of single chain hydrogen bonds linking water molecules within at the exteriors of the nanopores, reducing the resistance of water passing through the nanopores. Despite the smaller pore diameter, nanopores with 0.74 nm displayed higher water flux than that with 0.98 nm, and almost 100% of salt rejection, which was not observed for the larger nanopores. For example, although nanopores with diameter of 1.35 nm have shown the highest permeability, the salt rejection was very low (40%). Therefore, nanopores

with sub-nanometer diameters are most suitable to endow the MoS_2 membranes with appropriate water permeability and salt rejection.

4.3 2D nanopores for heavy metal removal from water

Besides NaCl, water can also present pollutants, such as heavy metals, which may pose a risk to human health. With the rapid development of industries, chemical waste has been thrown deliberately into the water to the point of making it difficult to clean. Particularly, direct or indirect discharge of heavy metals into the environment has increased recently, especially in developing countries. Unlike organic contaminants, heavy metals are not biodegradable and tend to accumulate in living organisms. Many heavy metal ions are also known to be toxic or carcinogenic. Toxic heavy metals of particular concern in the treatment of industrial waste-water include zinc, copper, iron, mercury, cadmium, lead, and chromium. As a result, the filtration process that can acquire fresh-water from contaminated, brackish water or seawater is an effective method to also increase the potable water supply. Membranes nanotechnology can, therefore, be used for clean water from these pollutants.

We have used molecular dynamic simulations to show that single-layers of MoS_2 and graphene can effectively reject ions and allow high water permeability. Solutions of water and three cations with different valence (Na^+, Zn^{2+} and Fe^{3+}) were investigated in the presence of the two types of membranes and the results indicate a high dependence of the ion rejection on the cation charge. A typical simulation box consists of a graphene sheet acting as a rigid piston in order to apply an external force (pressure) over the ionic solution. The pressure gradient forces the solution against the 2D nanopore: a single-layer of molybdenum disulfide or graphene. Figure 4.4 shows the schematic representation of the simulation framework.

As can be seen in Figure 4.5, the ion rejection by the smallest pores for graphene and MoS_2 is 100% for all applied pressures and cation solutions. Additionally, The associative characteristic of ferric chloride leads to a high rate of ion rejection by both nanopores, while the monovalent sodium chloride induces lower rejection rates. Particularly, MoS_2 shows 100% of Fe^{3+} rejection for all pore sizes and applied pressures. The ion rejection performance of molybdenum disulfide membranes is superior to that observed for graphene membranes for all ranges of pressure, sizes, and cation valences. For instance, for the divalent case Zn^{2+} at low pressure differences, the rejection is 100% for all pore sizes in the MoS_2 membrane, while for the graphene membrane, we observe cation permeation for the bigger pores. A detailed presentation of this analysis is shown in the complete paper

following the Appendix D.

4.4 Flocculation for higher desalination: Mixing salt and ferric chloride

The flocculant characteristic of $Fe^{3+}Cl_3{}^-$ pointed in our previous work would be useful, for instance, to aggregate salt ions in order to form big clusters, larger enough to be trapped by the nanopore. The idea is to add ferric chloride to the system depicted in Figure 4.4.

We have implemented MD simulations to show that adding ferric chloride to a salt water solution can significantly increase the salt rejection by nanoporous membrane. The percentage of total ions rejected by the MoS_2 and graphene nanopores is plotted as a function of the applied pressure in Fig. 4.6. Even for nanopores beyond 1 nm, where the efficiency of the membrane is low, the clustering process lead to a 100% of salt rejection. Additionally, we have found a relation between the increase in ionic rejection and the percentage of Fe^{3+} added to the Na^+Cl^- solution.

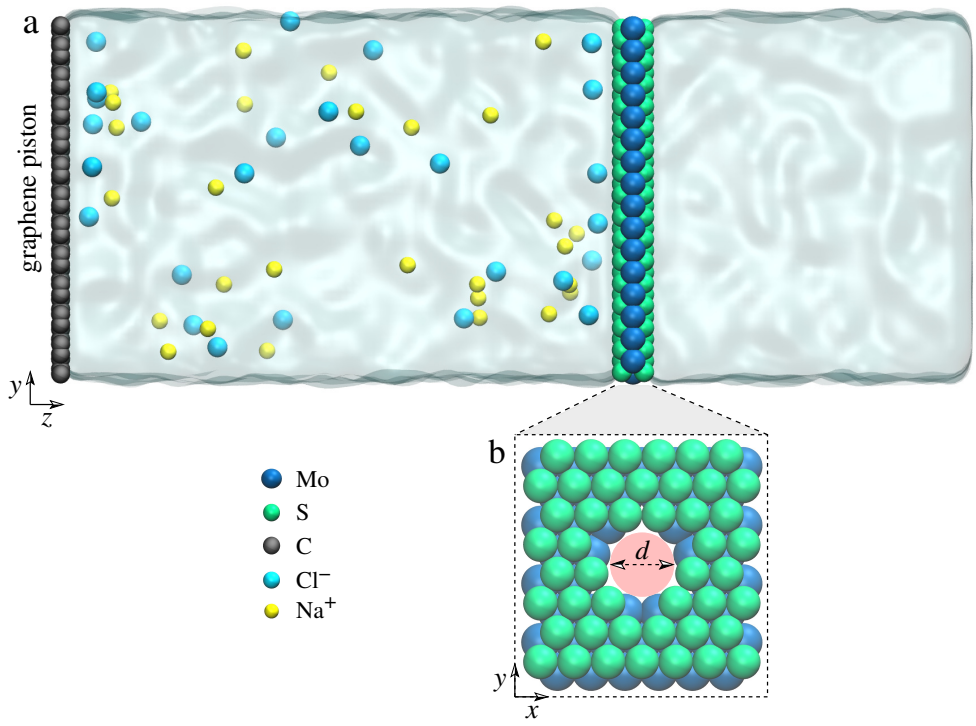

Figure 4.4: Schematic representation of the simulation framework. The system is divided as follows: On the left side we can see the piston (graphene) pressing the ionic solution against the MoS_2 nanopore. On the right side, we have bulk water. (b) Definition of the pore diameter d. From [119] (see appendix D for details).

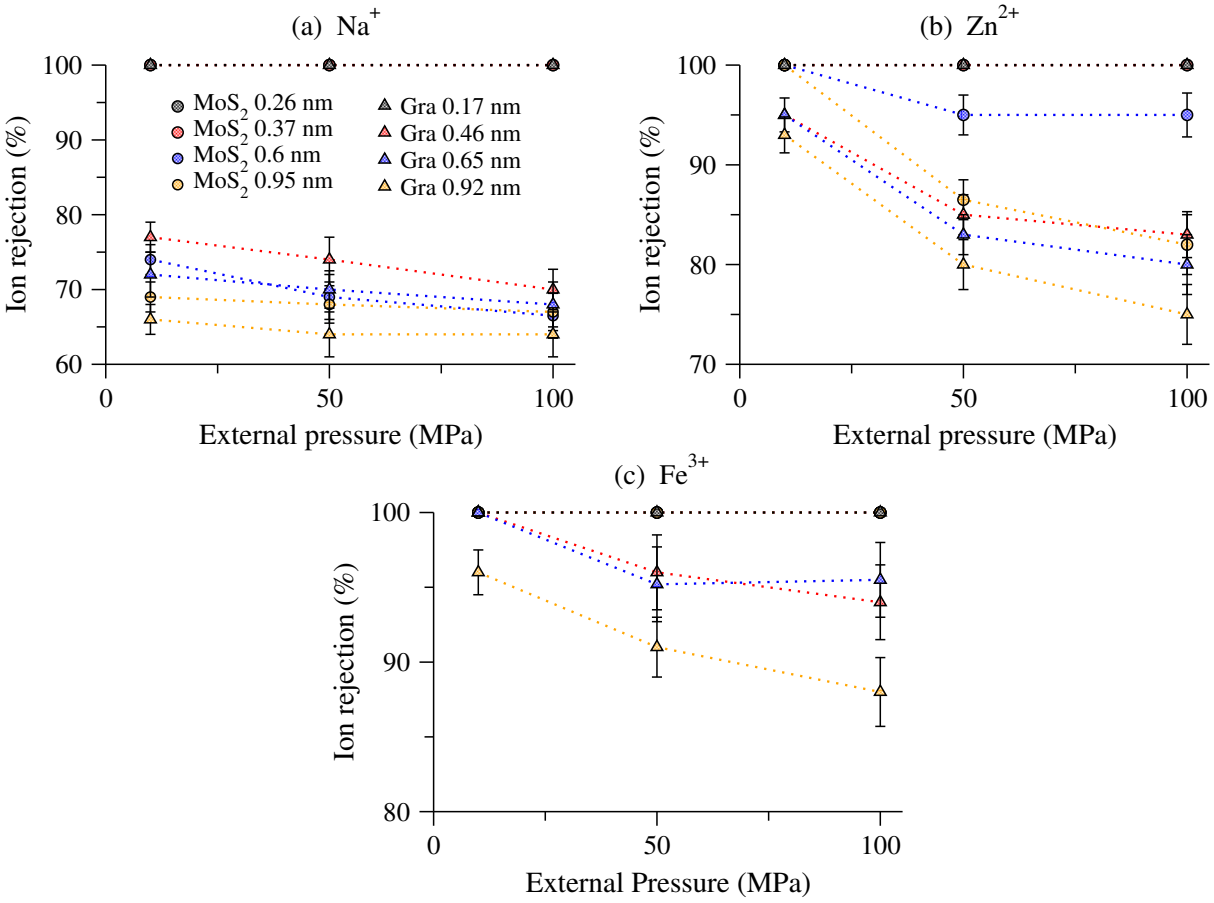

Figure 4.5: Percentage of ion rejection by various pores as a function of the applied pressure. Pores with different diameters are considered. From [119] (see appendix D for details).

The efficiency of desalination through nanoporous membranes is usually limited by the size of the pore: as the area of the pore increases, the efficiency of rejection decreases [38]. Here, we have used effective pore diameters (discounted the van der Waals radii) of ∼1 nm, larger than that used by most of simulations with nanopores [100, 38, 120]. By adding Fe^{3+} to the solution we have achieved 100% of ion blockage, which is not observed in simple saline solutions even with functionalization of the nanopore [100]. The mechanism behind this new behavior is that adding Fe^{3+} in the NaCl solution leads to the formation of ionic clusters. This clusterization is mainly regulated by the charge inversion phenomena occurring when the Cl^- anions are attracted by Fe^{3+}, causing the excess of negative charge and the consequently inversion of sign in the charge distribution profile. Then, the Na^+ cation is attracted to this cluster. As result, the cross section of the clusters is larger than the accessible diameter of the pore.

This phenomena can be better observed in the snapshots depicted in Fig. 4.7. While in

the absence of $Fe^{3+}Cl_3^-$, Figs. 4.7(a) and (b), the ions spread out through the simulation box, when the ferric chloride is added to the solution the ions assemble to form big clusters, avoiding the ion passage through the membrane. The rejection is then mainly dictated by the size of these clusters: when we add enough Fe^{3+} to the system the cross section of the clusters becomes larger than the accessible area within the nanopore.

As we increase the proportion of ferric chloride the Na^+ ions aggregates forming large clusters, which is crucial for the ion blockage at the nanopore interface. This result shows how we can improve the efficiency of nanoporous membranes for water desalination using flocculant chemicals. The detailed analysis is shown in the complete paper following the Appendix E.

In summary, in this chapter the behavior of a mixture of water, NaCl and multivalent ions were observed as the solution is pushed through a MoS_2 nanopore. Our results indicate a high clean water recovery from the proccess in particular in the case where water is mixed with both NaCl and multivalelent ions. In this case these ions work as

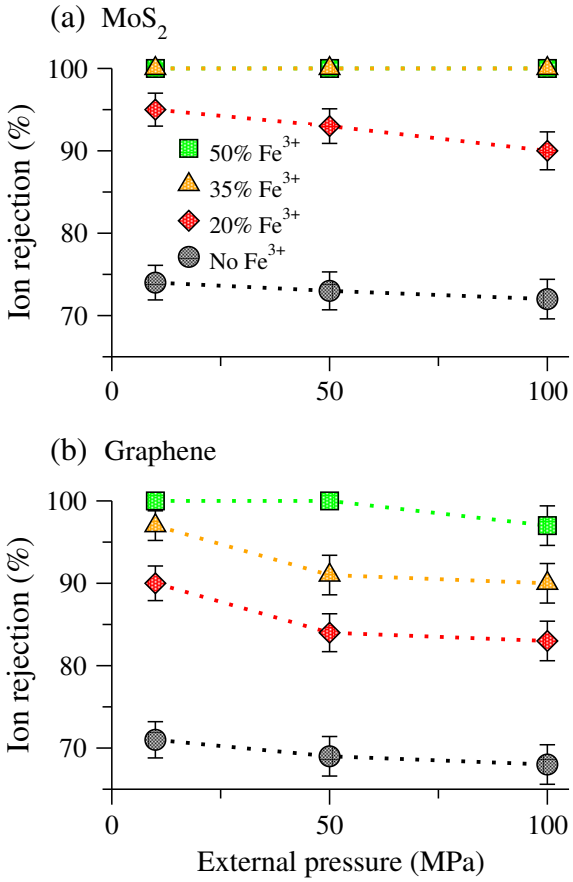

Figure 4.6: Percentage of ion rejection as a function of the applied pressure for (a) MoS_2 and (b) graphene with distinct concentrations of ferric chloride. See appendix E for details.

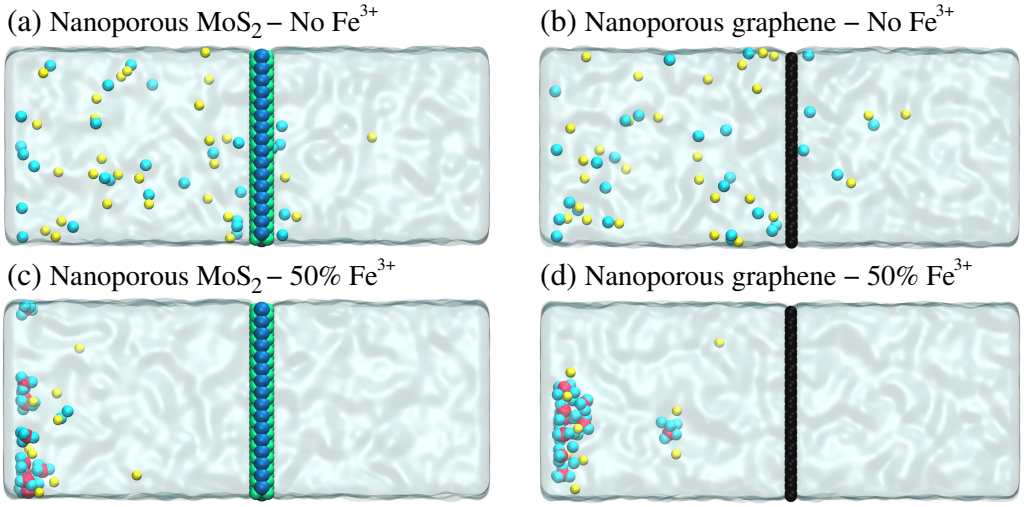

Figure 4.7: (On the top) side view snapshots after 5 ns of simulations of Na^+Cl^- passing through (a) MoS_2 and (b) graphene nanopore without any trace of clusterization. (Bottom) $Fe^{3+}Cl_3^-$ cluster formation preventing the ion passage through (c) MoS_2 and (d) graphene nanopores. These configurations are for applied pressures of 50 MPa. See appendix E for details.

flocculant. The results were both published in the reference [119] and submitted to The Journal of Chemical Physics (Under Review). They are also presented in the appendixes D and E.

Chapter 5

Conclusions

5.1 Conclusions

First, We have explored the situation in which water is restricted to the cavity of a nanotube with tunable hydrophobicity. Nanotubes with diameter ranging from 1.5 to 5 nm were analyzed. For the small nanotubes, the hydrophobic confinement presents a peculiar behavior. As the density is increased the viscosity shows a huge increase associated with a small increase in the diffusion coefficient. This breakdown in the Stokes-Einstein relation for diffusion and viscosity was observed in the hydrophobic, but not in the hydrophilic nanotubes. The mechanism underlying this behavior is dictated by the structure of water under confinement. This result indicates that some of the features observed for water inside hydrophobic carbon nanotubes cannot be observed in other nanopores.

Next, our results show that both the water structure and dynamics are strongly influenced by polarity inside narrow nanotubes, where water layers were observed, and the influence is negligible for wider nanotubes, where the water has a bulk-like density profile. As well, we show that water at low density can have a smaller diffusion inside nanotubes than water at higher densities. This result is a consequence of water diffusion anomaly.

The temperature as a critical parameter for water structuration and flow inside hydrophobic and hydrophilic nanopores has also been investigated. In this case, nanotubes with diameter ranging from 0.8 to 1.0 nm were analyzed. We have found evidence for dynamical transitions as we increase the temperature of the water-nanotube system, and the nanotube size and hydrophobicity may play an important role in this phenomena, since hydrophobic pores leads to structural dependence of water on the temperature for (8,8) nanotubes. We believe these studies represent an important step towards a deeper, comprehensive understanding of nanofluidic systems.

Additionally, a molecular dynamics study has demonstrated the possibility of water desalination through nanoporous graphene and MoS_2 membranes. The ionic valence has been found to strongly influence both water flux and ion rejection by either membranes. The study points the pore size and chemistry as determinant factors for efficient water desalination: the smaller the pore, the larger is the ionic selectivity, with small advantage for MoS_2 membranes. Remarkebly, we have found the flocculant $Fe^{3+}Na_3^-$ to increase the ionic rejection by assembling the Na and Cl atoms into large clusters, which have been demonstrated to avoid the ion passage through the nanopores. These results highlight the promising application of 2D nanoporous membranes as molecular sieves and for water desalination.

Bibliography

[1] S. H. Lee, D. Kim, S. Kim, and C.-S. Han. Flow-induced voltage generation in high-purity metallic and semiconducting carbon nanotubes. *Applied Physics Letters*, 99:104103, 2011.

[2] J. Kim, J. Lee, S. Kim, and W. Jung. Highly increased flow-induced power generation on plasmonically carbonized single-walled carbon nanotube. *ACS Appl. Mater. Interfaces*, 8:29877–29882, 2016.

[3] L. Bocquet and P. Tabeling. Physics and technological aspects of nanofluidics. *Lab Chip*, 14:3143–3158, 2014.

[4] A. Bussonniere, M. B. Bigdeli, D.-Y. Chueh, Q. Liu, P. Chen, and P. A. Tsai. Universal wetting transition of an evaporating water droplet on hydrophobic micro- and nano-structures. *Soft Matter*, 13:978–984, 2017.

[5] Z. Yoshimitsu, A. Nakajima, T. Watanabe, and K. Hashimoto. Effects of surface structure on the hydrophobicity and sliding behavior of water droplets. *Langmuir*, 18:5818–5822, 2002.

[6] C. S. Tian and Y. R. Shen. Structure and charging of hydrophobic material/water interfaces studied by phase-sensitive sum-frequency vibrational spectroscopy. *Proc. Natl. Acad. Sci. U.S.A.*, 106:15148–15153, 2009.

[7] A. J. Patel, P. Varilly, S. N. Jamadagni, M. F. Hagan, D. Chandler, and S. Garde. Sitting at the edge: How biomolecules use hydrophobicity to tune their interactions and function. *J. Phys. Chem. B*, 116:2498–2503, 2012.

[8] D. I. Verrelli, P. T.L. Koh, and A. V. Nguyen. Particle-bubble interaction and attachment in flotation. *Chem. Eng. Sci.*, 66:5910–5921, 2011.

[9] L. Joly. Capillary filling with giant liquid/solid slip: Dynamics of water uptake by carbon nanotubes. *J. Chem. Phys.*, 135:214705, 2011.

[10] K. Goh and Y. Chen. Controlling water transport in carbon nanotubes. *Nano Today*, 14:13–15, 2017.

[11] M. Majumder, N. Chopra, R. Andrews, and B. J. Hinds. Nanoscale hydrodynamics: Enhanced flow in carbon nanotubes. *Nature*, 438:44, 2005.

[12] L. Bocquet and J.-L. Barrat. Flow boundary conditions from nano- to micro-scales. *Soft Matter*, 3:685–693, 2007.

[13] D. Gomes, A. Agasse, P. Thiebaud, S. Delrot, H. Geros, and F. Chaumont. Aquaporins are multifunctional water and solute transporters highly divergent in living organisms. *Biochim. Biophys. Acta*, 1788:1213–1228, 2009.

[14] S. Gravelle, L. Joly, F. Detcheverry, C. Ybert, C. Cottin-Bizonne, and L. Bocquet. Optimizing water permeability through the hourglass shape of aquaporins. *Proc. Natl. Acad. Sci. U.S.A.*, 110:16367–16372, 2013.

[15] C. I. Bouzigues, P. Tabeling, and L. Bocquet. Nanofluidics in the debye layer at hydrophilic and hydrophobic surfaces. *Phys. Rev. Lett.*, 101:114503, 2008.

[16] S. Joseph and N. R. Aluru. Pumping of confined water in carbon nanotubes by rotation-translation coupling. *Phys. Rev. Lett.*, 101:064502, 2008.

[17] M. H. Köhler, J. R. Bordin, L. B. da Silva, and M. C. Barbosa. Breakdown of the stokes-einstein water transport through narrow hydrophobic nanotubes. *Phys. Chem. Chem. Phys.*, 19:12921–12927, 2017.

[18] Y. Maniwa, H. Kataura, M. Abe, A. Udaka, S. Suzuki, Y. Achiba, H. Kira, K. Matsuda, H. Kadowaki, and Y. Okabe. Ordered water inside carbon nanotubes: formation of pentagonal to octagonal ice-nanotubes. *Chem. Phys. Lett.*, 401:534–538, 2005.

[19] D. Takaiwa, I. Hatano, K. Koga, and H. Tanaka. Phase diagram of water in carbon nanotubes. *Proc. Natl. Acad. Sci. U.S.A.*, 105:39–43, 2008.

[20] J. R. Bordin, J. S. Andrade Jr., A. Diehl, and M. C. Barbosa. Enhanced flow of core-softened fluids through narrow nanotubes. *J. Chem. Phys.*, 140:194504, 2014.

[21] J. R. Bordin, A. B. de Oliveira, A. Diehl, and Marcia C. Barbosa. Diffusion enhancement in core-softened fluid confined in nanotubes. *J. Chem. Phys.*, 137:084504, 2012.

[22] M.-C. Bellissent-Funel, A. Hassanali, M. Havenith, R. Henchman, P. Pohl, F. Sterpone, D. van der Spoel, Y. Xu, and A. Garcia. Water determines the structure and dynamics of proteins. *Chemical Reviews*, 116:7673–7697, 2016.

[23] R. Jain. Providing safe drinking water: a challenge for humanity. *Clean Technol. Environ. Policy*, 14:1–4, 2012.

[24] M. A. Shannon, P. W. Bohn, M. Elimelech, J. G. Georgiadis, B. J. Marinas, and A. M. Mayes. Science and technology for water purification in the coming decades. *Nature*, 452:301–310, 2008.

[25] L. F. Greenlee, D. F. Lawler, B. D. Freeman, B. Marrot, and P. Moulin. Reverse osmosis desalination: Water sources, technology, and today's challenges. *Water Research*, 43:2317–2348, 2009.

[26] M. Elimelech and W. A. Phillip. The future of seawater desalination: Energy, technology, and the environment. *Science*, 333:712–717, 2011.

[27] Q. Schiermeier. Water on tap. *Nature*, 510:326–328, 2014.

[28] N. Misdan, W. J. Lau, and A. F. Ismail. Seawater reverse osmosis (swro) desalination by thin-film composite membrane—current development, challenges and future prospects. *Desalination*, 287:228–237, 2012.

[29] R. Yang, J. Xu, G. Ozaydin-Ince, S. Y. Wong, and K. K. Gleason. Surface-tethered zwitterionic ultrathin antifouling coatings on reverse osmosis membranes by initiated chemical vapor deposition. *Chem. Mater.*, 23:1263–1272, 2011.

[30] T Humplik, J Lee, S C O'Hern, B A Fellman, M A Baig, S F Hassan, M A Atieh, F Rahman, T Laoui, R Karnik, and E N Wang. Nanostructured materials for water desalination. *Nanotechnology*, 22:292001, 2011.

[31] J. Dulebohn, P. Ahmadiannamini, T. Wang, S.-S. Kim, T. Pinnavaia, and V. Tarabara. Polymer mesocomposites: Ultrafiltration membrane materials with enhanced permeability, selectivity and fouling resistance. *J. Membrane Science*, 453:478–488, 2014.

[32] J. Kujawa, S. Cerneaux, S. Koter, and W. Kujawski. Highly efficient hydrophobic titania ceramic membranes for water desalination. *ACS Appl. Mater. Interfaces*, 6:14223–14230, 2014.

[33] F. Fornasiero, J. In, S. Kim, H. Park, Y. Wang, C. Grigoropoulos, A. Noy, and O. Bakajin. ph-tunable ion selectivity in carbon nanotube pores. *Langmuir*, 26:14848–14853, 2010.

[34] Z. Hu, Y. Chen, and J. Jiang. Zeolitic imidazolate framework-8 as a reverse osmosis membrane for water desalination: Insight from molecular simulation. *J. Chem. Phys.*, 134:134705, 2011.

[35] G. Xu, J. Xu, H. Su, X. Liu, Lu-Li, H. Zhao, H. Feng, and Rasel Das. Two-dimensional (2d) nanoporous membranes with sub-nanopores in reverse osmosis desalination: Latest developments and future directions. *Desalination*, doi: 10.1016/j.desal.2017.09.024, 2018.

[36] S. P. Surwade, S. N. Smirnov, I. V. Vlassiouk, R. R. Unocic, G. M. Veith, S. Dai, and S. M. Mahurin. Water desalination using nanoporous single-layer graphene. *Nat. Nanotechnol.*, 10:459–464, 2015.

[37] W. Lei, D. Portehault, D. Liu, S. Qin, and Y. Chen. Porous boron nitride nanosheets for effective water cleaning. *Nat. Commun.*, 4:1777, 2013.

[38] M. Heiranian, A. B. Farimani, and N. R. Aluru. Water desalination with a single-layer mos_2 nanopore. *Nat. Commun.*, 6:8616, 2015.

[39] Q. Li, N. Zhang, Y. Yang, G. Wang, and D. H. L. Ng. High efficiency photocatalysis for pollutant degradation with mos2/c3n4 heterostructures. *Langmuir*, 30:8965–8972, 2014.

[40] L. Sun, Y. Ying, H. Huang, Z. Song, Y. Mao, Z. Xu, and X. Peng. Ultrafast molecule separation through layered ws2 nanosheet membranes. *ACS Nano*, 8:6304–6311, 2014.

[41] Y. Ying, Y. Liu, X. Wang, Y. Mao, W. Cao, P. Hu, and X. Peng. Two-dimensional titanium carbide for efficiently reductive removal of highly toxic chromium(vi) from water. *ACS Appl. Mater. Interfaces*, 7:1795–1803, 2015.

[42] C. E. Ren, K. B. Hatzell, M. Alhabeb, Z. Ling, K. A. Mahmoud, and Y. Gogotsi. Charge- and size-selective ion sieving through ti3c2tx mxene membranes. *J. Phys. Chem. Lett.*, 6:4026–4031, 2015.

[43] C. Dean, A. Young, I. Meric, C. Lee, L. Wang, S. Sorgenfrei, K. Watanabe, T. Taniguchi, P. Kim, and K. Shepard. Boron nitride substrates for high-quality graphene electronics. *Nat. Nanotechnol.*, 5:722–726, 2010.

[44] P. J. Zomer, S. P. Dash, N. Tombros, and B. J. van Wees. A transfer technique for high mobility graphene devices on commercially available hexagonal boron nitride. *Appl. Phys. Lett.*, 99:232104, 2011.

[45] L. Sun, H. Huang, and X. Peng. Laminar mos2 membranes for molecule separation. *Chem. Commun.*, 49:10718–10720, 2013.

[46] K. V. Agrawal, S. Shimizu, L. W. Drahushuk, D. Kilcoyne, and M. S. Strano. Observation of extreme phase transition temperatures of water confined inside isolated carbon nanotubes. *Nat. Nanotechnology*, 12:267–273, 2017.

[47] L. Wu, X. Zhou, H. Lu, Q. Liang, J. Kou, F. Wu, and J. Fan. A controllable water signal transistor. *Phys. Chem. Chem. Phys.*, 19:9625–9629, 2017.

[48] K. Xiao, Y. Zhou, X. Kong, G. Xie, P. Li, Z. Zhang, L. Wen, and L. Jiang. Electrostatic-charge- and electric-field-induced smart gating for water transportation. *ACS Nano*, 10:9703–9709, 2016.

[49] J. Kou, M. Mei, H. Lu, F. Wu, and J. Fan. Unidirectional motion of a water nanodroplet subjected to a surface energy gradient. *Phys. Rev. E*, 85:056301, 2012.

[50] C. Catlow and W. C. Mackrodt. *Computer Simulation of Solids.* Springer-Verlag, Berlin, 1982.

[51] J.-P. Hansen and I. R. McDonald. *Theory of Simple Liquids.* Academic Press, San Diego, 2013.

[52] R. W. Hockney and J. W. Eastwood. *Computer Simulation Using Particles.* McGraw-Hill, New York, 1981.

[53] M. P. Allen and D. J. Tildesley. *Computer simulation of liquids.* Oxford University Press, 1989.

[54] D. Frenkel and B. Smit. *Understanding molecular simulation.* Academic Press, San Diego, 1996.

[55] L. Verlet. Computer "experiments" on classical fluids. I. Thermodynamical properties of Lennard-Jones molecules. *Phys. Rev.*, 159:98–103, 1967.

[56] S. Plimpton. Fast parallel algorithms for short-range molecular dynamics. *J. Comp. Phys.*, 117:1–19, 1995.

[57] K. Mawatari, T. Tsukahara, Y. Sugii, and T. Kitamori. Extended-nano fluidic systems for analytical and chemical technologies. *Nanoscale*, 2:1588–1595, 2010.

[58] K. Balasubramanian and M. Burghard. Chemically functionalized carbon nanotubes. *Small*, 1:180–192, 2005.

[59] V. Georgakilas, D. Gournis, V. Tzitzios, L. Pasquato, D. M. Guldi, and M. Prato. Decorating carbon nanotubes with metal or semiconductor nanoparticles. *J. Mater. Chem.*, 17:2679–2694, 2007.

[60] A. Hirsch. Functionalization of single-walled carbon nanotubes. *Angew. Chem. Int. Ed.*, 41:1853–1859, 2002.

[61] F.-Y. Zhao, Y.-L. Ji, X.-D. Weng, Y.-F. Mi, C.-C. Ye, Q.-F. An, and C.-J. Gao. High-flux positively charged nanocomposite nanofiltration membranes filled with poly(dopamine) modified multiwall carbon nanotubes. *ACS Appl. Mater. Interfaces*, 8:6693–6700, 2016.

[62] T.-Y. Liu, H.-G. Yuan, Q. Li, Y.-H. Tang, Q. Zhang, W. Qian, B. Van der Bruggen, and X. Wang. Ion-responsive channels of zwitterion-carbon nanotube membrane for rapid water permeation and ultrahigh mono-multivalent ion selectivity. *ACS Nano*, 9:7488–7496, 2015.

[63] H. Y. Yang, Z. J. Han, S. F. Yu, K. L. Pey, K. Ostrikov, and R. Karnik. Carbon nanotube membranes with ultrahigh specific adsorption capacity for water desalination and purification. *Nat. Communications*, 4:2220, 2013.

[64] M. Thomas and B. Corry. A computational assessment of the permeability and salt rejection of carbon nanotube membranes and their application to water desalination. *Philos. Trans. R. Soc. A*, 374:2060, 2015.

[65] B. J. Hinds, N. Chopra, T. Rantell, R. Andrews, V. Gavalas, and L. G. Bachas. Aligned multiwalled carbon nanotube membranes. *Science*, 303(5654):62–65, 2004.

[66] J. K. Holt, H. G. Park, Y. Wang, M. Stadermann, A. B. Artyukhin, C. P. Grigoropoulos, A. Noy, and O. Bakajin. Fast mass transport through sub-2-nanometer carbon nanotubes. *Science*, 312(5776):1034–1037, 2006.

[67] B. Lee, Y. Baek, M. Lee, D. H. Jeong, H. Lee, J. Yoon, and Y. H. Kim. A carbon nanotube wall membrane for water treatment. *Nat. Communications*, 6:7109, 2015.

[68] M. S. Mauter and M. Elimelech. Environmental applications of carbon-based nanomaterials. *Environ. Sci. Technol.*, 42(16):5843–5859, 2008.

[69] J. Li, H. Tee Ng, A. Cassell, W. Fan, H. Chen, Q. Ye, J. Koehne, J. Han, and M. Meyyappan. Carbon nanotube nanoelectrode array for ultrasensitive dna detection. *Nano Lett.*, 3(5):597–602, 2003.

[70] P. S. Goh, A. F. Ismail, and B. C. Ng. Carbon nanotubes for desalination: Performance evaluation and current hurdles. *Desalination*, 308:2–14, 2013.

[71] M. Majumder and B. Corry. Anomalous decline of water transport in covalently modified carbon nanotube membranes. *Chem. Commun.*, 47:7683–7685, 2011.

[72] P. Král and M. Shapiro. Nanotube electron drag in flowing liquids. *Phys. Rev. Lett.*, 86:131–134, 2001.

[73] S. Ghosh, A. K. Sood, and N. Kumar. Carbon nanotube flow sensors. *Science*, 299(5609):1042–1044, 2003.

[74] J. Liu, L. Dai, and J. W. Baur. Multiwalled carbon nanotubes for flow-induced voltage generation. *J. Appl. Phys.*, 101:064312, 2007.

[75] A. Kolesnikov, J.-M. Zanotti, C.-K. Loong, P. Thiyagarajan, A. Moravsky, R. Loutfy, and C. Burnham. Anomalously soft dynamics of water in a nanotube: A revelation of nanoscale confinement. *Phys. Rev. Lett.*, 93:035503, 2004.

[76] Y. Maniwa, K. Matsuda, H. Kyakuno, S. Ogasawara, T. Hibi, H. Kadowaki, S. Suzuki, Y. Achiba, and H. Kataura. Water-filled single-wall carbon nanotubes as molecular nanovalves. *Nat. Materials*, 6:135–141, 2007.

[77] K. Nomura, T. Kaneko, J. Bai, J. S. Francisco, K. Yasuoka, and X. C. Zeng. Evidence of low-density and high-density liquid phases and isochore end point for water confined to carbon nanotube. *Proc. Natl. Acad. Sci. U.S.A.*, 114:4066–4071, 2017.

[78] H. Kyakuno, K. Matsuda, H. Yahiro, Y. Inami, T. Fukuoka, Y. Miyata, K. Yanagi, Y. Maniwa, H. Kataura, T. Saito, M. Yumura, and S. Iijima. Confined water inside single-walled carbon nanotubes: Global phase diagram and effect of finite length. *J. Chem. Phys.*, 134:244501, 2011.

[79] H. Kyakuno, M. Fukasawa, R. Ichimura, K. Matsuda, Y. Nakai, Y. Miyata, T. Saito, and Y. Maniwa. Diameter-dependent hydrophobicity in carbon nanotubes. *J. Chem. Phys.*, 145:064514, 2016.

[80] H.-J. Wang, X.-K. Xi, A. Kleinhammes, and Y. Wu. Temperature-induced hydrophobic-hydrophilic transition observed by water adsorption. *Science*, 322:80–83, 2008.

[81] X. Gong, J. Li, H. Lu, R. Wan, J. Li, J. Hu, and H. Fang. A charge-driven molecular water pump. *Nat. Nanotechnology*, 2:709–712, 2007.

[82] G. Hummer, J. C. Rasaiah, and J. P. Noworyta. Water conduction through the hydrophobic channel of a carbon nanotube. *Nature*, 414:188–190, 2001.

[83] J. R. Bordin and M. C. Barbosa. Flow and structure of fluids in functionalized nanopores. *Physica A: Statistical Mechanics and its Applications*, 467:137–147, 2017.

[84] X. Wei, D.-M. Tang, Q. Chen, Y. Bando, and D. Golberg. Local coulomb explosion of boron nitride nanotubes under electron beam irradiation. *ACS Nano*, 7:3491–3497, 2013.

[85] X. Wei, M.-S. Wang, Y. Bando, and D. Golberg. Post-synthesis carbon doping of individual multiwalled boron nitride nanotubes via electron-beam irradiation. *J. Am. Chem. Soc.*, 132:13592–13593, 2010.

[86] M. H. Köhler and L. B. da Silva. Size effects and the role of density on the viscosity of water confined in carbon nanotubes. *Chem. Phys. Lett.*, 645:38–41, 2016.

[87] M. Melillo, F. Zhu, M. A. Snyder, and J. Mittal. Water transport through nanotubes with varying interaction strength between tube wall and water. *J. Phys. Chem. Lett.*, 2:2978–2983, 2011.

[88] J. R. Bordin, A. Diehl, M. C. Barbosa, and Y. Levin. Ion fluxes through nanopores and transmembrane channels. *Phys. Rev. E*, 85:031914, 2012.

[89] J. R. Bordin, A. Diehl, and M. C. Barbosa. Relation between flow enhancement factor and structure for core-softened fluids inside nanotubes. *J. Phys. Chem. B*, 117:7047–7056, 2013.

[90] I. Moskowitz, M. A. Snyder, and J. Mittal. Water transport through functionalized nanotubes with tunable hydrophobicity. *J. Chem. Phys.*, 141:18C532, 2014.

[91] J. Abascal and C. Vega. A general purpose model for the condensed phases of water: Tip4p/2005. *J. Chem. Phys.*, 123:234505, 2005.

[92] M. H. Köhler, R. C. Barbosa, L. B. da Silva, and M. C. Barbosa. Role of the hydrophobic and hydrophilic sites in the dynamic crossover of the protein-hydration water. *Phys. A*, 468:733–739, 2017.

[93] M. H. Köhler and J. R. Bordin. Surface, density, and temperature effects on the water diffusion and structure inside narrow nanotubes. *J. Phys. Chem. C*, 122:6684–6690, 2018.

[94] Tod A. Pascal, William A. Goddard, and Yousung Jung. Entropy and the driving force for the filling of carbon nanotubes with water. *Proc. Natl. Acad. Sci. U.S.A.*, 108:11794–11798, 2011.

[95] A. Esfandiar, B. Radha, F. C. Wang, Q. Yang, S. Hu, S. Garaj, R. R. Nair, A. K. Geim, and K. Gopinadhan. Size effect in ion transport through angstrom-scale slits. *Science*, 358:511–513, 2017.

[96] S. Homaeigohar and M. Elbahri. Graphene membranes for water desalination. *Npg Asia Materials*, 9:e427, 2017.

[97] K. Mahmoud, B. Mansoor, A. Mansour, and M. Khraisheh. Functional graphene nanosheets: The next generation membranes for water desalination. *Desalination*, 356:208–225, 2015.

[98] Z. Hu, B. Liu, M. Dahanayaka, A. Law, J. Wei, and K. Zhou. Ultrafast permeation of seawater pervaporation using single-layered c2n via strain engineering. *Phys. Chem. Chem. Phys.*, 19:15973–15979, 2017.

[99] K. Zhang, Z. He, K. M. Gupta, and J. Jiang. Computational design of 2d functional covalent-organic framework membranes for water desalination. *Environ. Sci.: Water Res. Technol.*, 3:735–743, 2017.

[100] D. Cohen-Tanugi and J. C. Grossman. Water desalination across nanoporous graphene. *Nano Lett.*, 12:3602–3608, 2012.

[101] K. Watanabe, T. Taniguchi, and H. Kanda. Direct-bandgap properties and evidence for ultraviolet lasing of hexagonal boron nitride single crystal. *Nature Materials*, 3:404–409, 2004.

[102] J. Coleman, M. Lotya, A. O'Neill, S. Bergin, P. King, U. Khan, K. Young, A. Gaucher, S. De, R. Smith, I. Shvets, S. Arora, G. Stanton, H. Kim, K. Lee, G. Kim, G. Duesberg, T. Hallam, J. Boland, J. Wang, J. Donegan, J. Grunlan, G. Moriarty, A. Shmeliov, R. Nicholls, J. Perkins, E. Grieveson, K. Theuwissen, D. McComb, P. Nellist, and V. Nicolosi. Two-dimensional nanosheets produced by liquid exfoliation of layered materials. *Science*, 331:568–571, 2011.

[103] S. Bertolazzi, J. Brivio, and A. Kis. Stretching and breaking of ultrathin mos2. *ACS Nano*, 5:9703–9709, 2011.

[104] P. Waduge, I. Bilgin, J. Larkin, R. Henley, K. Goodfellow, A. Graham, D. Bell, N. Vamivakas, S. Kar, and M. Wanunu. Direct and scalable deposition of atomically thin low-noise mos2 membranes on apertures. *ACS Nano*, 9:7352–7359, 2015.

[105] A. van der Zande, P. Huang, D. Chenet, T. Berkelbach, Y. You, G.-H. Lee, T. Heinz, D. Reichman, D. Muller, and J. Hone. Grains and grain boundaries in highly crystalline monolayer molybdenum disulphide. *Nature Materials*, 12:554–561, 2013.

[106] K. Liu, J. Feng, A. Kis, and A. Radenovic. Atomically thin molybdenum disulfide nanopores with high sensitivity for dna translocation. *ACS Nano*, 8:2504–2511, 2014.

[107] J. Feng, K. Liu, M. Graf, M. Lihter, R. D. Bulushev, D. Dumcenco, D. T. L. Alexander, D. Krasnozhon, T. Vuletic, A. Kis, and A. Radenovic. Electrochemical reaction in single layer mos2: Nanopores opened atom by atom. *Nano Lett.*, 15:3431–3438, 2015.

[108] S. M. Gilbert, G. Dunn, A. Azizi, T. Pham, B. Shevitski, E. Dimitrov, S. Liu, Shaul A., and A. Zettl. Fabrication of subnanometer precision nanopores in hexagonal boron nitride. *Sci. Rep.*, 7:15096, 2017.

[109] C. M. Frament and J. R. Dwyer. Conductance-based determination of solid-state nanopore size and shape: An exploration of performance limits. *J. Phys. Chem. C*, 116:23315–23321, 2012.

[110] C. Wen, Z. Zhang, and S.-L. Zhang. Physical model for rapid and accurate determination of nanopore size via conductance measurement. *ACS Sens.*, 2:1523–1530, 2017.

[111] M. E. Suk and N. R. Aluru. Effect of induced electric field on single-file reverse osmosis. *Phys. Chem. Chem. Phys.*, 11:8614–8619, 2009.

[112] Y. Liu, B. Wang, E. Li, X. Song, H. Yan, and X. Zhang. The preparation of a strawberry-like super-hydrophilic surface on the molybdenum substrate. *Colloids Surf. A Physicochem. Eng. Asp.*, 404:52–55, 2012.

[113] S. Gravelle, L. Joly, C. Ybert, and L. Bocquet. Large permeabilities of hourglass nanopores: From hydrodynamics to single file transport. *J. Chem. Phys.*, 141:18C526, 2014.

[114] C. Belin, L. Joly, and F. Detcheverry. Optimal shape of entrances for a frictionless nanochannel. *Phys. Rev. Fluids*, 1:054103, 2016.

[115] A. Barati Farimani, N. R. Aluru, and Emad Tajkhorshid. Thermodynamic insight into spontaneous hydration and rapid water permeation in aquaporins. *Appl. Phys. Lett.*, 105:083702, 2014.

[116] J.-U. Lee, D. Yoon, and H. Cheong. Estimation of young's modulus of graphene by raman spectroscopy. *Nano Lett.*, 12:4444–4448, 2012.

[117] W. Li, Y. Yang, J. Weber, G. Zhang, and R. Zhou. Tunable, strain-controlled nanoporous mos2 filter for water desalination. *ACS Nano*, 10:1829–1835, 2016.

[118] J. Kou, J. Yao, L. Wu, X. Zhou, H. Lu, F. Wu, and J. Fan. Nanoporous two-dimensional mos2 membranes for fast saline solution purification. *Phys. Chem. Chem. Phys.*, 18:22210–22216, 2016.

[119] M. H. Köhler, J. R. Bordin, and M. C. Barbosa. 2d nanoporous membrane for cation removal from water: Effects of ionic valence, membrane hydrophobicity, and pore size. *J. Chem. Phys.*, 148:222804, 2018.

[120] W. Li, Y. Yang, J. Weber, G. Zhang, and R. Zhou. Tunable, strain-controlled nanoporous MoS_2 filter for water desalination. *ACS Nano*, 10:1829–1835, 2016.

Appendix A

PCCP

PAPER

View Article Online
View Journal | View Issue

Cite this: *Phys. Chem. Chem. Phys.*, 2017, **19**, 12921

Breakdown of the Stokes–Einstein water transport through narrow hydrophobic nanotubes

Mateus Henrique Köhler, *[a] José Rafael Bordin,[b] Leandro B. da Silva[c] and Marcia C. Barbosa[a]

Received 30th March 2017,
Accepted 19th April 2017

DOI: 10.1039/c7cp02058a

rsc.li/pccp

In this paper the transport properties of water confined inside hydrophobic and hydrophilic nanotubes are compared for different nanotube radii and densities. While for wider nanotubes the nature of the wall plays no relevant role in the water mobility, for small nanotubes the hydrophobic confinement presents a peculiar behavior. As the density is increased the viscosity shows a huge increase associated with a small increase in the diffusion coefficient. This breakdown in the Stokes–Einstein relation for diffusion and viscosity was observed in the hydrophobic, but not in the hydrophilic nanotubes. The mechanism underlying this behavior is explained in terms of the structure of water under confinement. This result indicates that some of the features observed for water inside hydrophobic carbon nanotubes cannot be observed in other nanopores.

1 Introduction

Carbon nanotubes (CNTs) have been shown to facilitate ultra-fast diffusion of water,[1–4] which is a viable strategy for desalination,[5] water treatment,[6,7] photoredox catalysis[8] and the development of biochemical nanosensors.[9,10] The applications utilizing water transport through CNTs are of particular interest due to the fast water transport predicted by molecular dynamics (MD) simulations[11] and later observed in experiments.[3,12,13]

In principle in the processes with CNTs the wall can be considered as a hydrophobic material. However, for many applications the functionalization of the confining geometry is needed. One case is the gas storage capacity of nanomaterials.[5,14,15] In other cases, the functionalization of CNTs is often either a prerequisite for their processing,[16] or desirable for sensitivity and selectivity in molecular detection.[17–19] Moreover, nanotubes with similar structural features to CNTs, but different atomic composition (such as Boron–Nitride[20]), can now be routinely synthesized.

In the context of biological nanochannels, the water–surface interactions can vary depending on the hydrophobicity of the amino acids involved.[21] Also, silica nanopores in porous rocks have hydrophobic or hydrophilic interactions.[22] In all of these cases, as the interaction between water and the nanotube atoms changes depending on its functionalization and composition, the dynamic behavior of water molecules will also be influenced. Despite the large number of studies on the water flow through CNTs, the water properties inside functionalized nanotubes are still not clear. Simple models that incorporate the details of nanotube functionalization may enable important progress in the overall understanding of fluid flow through nanopipes.[23,24]

For instance, Hummer *et al.*[11] have shown that very small changes in the water–carbon interaction can have an impact on whether water enters a CNT or not. Melillo *et al.*[25] also demonstrated, by varying the interaction strength, that the hydrophilicity of nanotubes is the key factor for water occupancy and can determine their structure and dynamics. The water shear viscosity has been revealed as being very sensitive to the nanoscale confinement.[26,27] Moreover, the connection between water dynamics and the structure of the confined water still remains an open subject, the answer to which may require deeper physical–chemical insights.[28]

In this work we are interested in studying the transport behavior of water inside hydrophilic and hydrophobic nanotubes. Our focus is on nanopores with radii large enough to accommodate more than a single file of water, and we study water at distinct densities. In this way, we perform molecular dynamics (MD) simulations of TIP4P/2005 water[29] confined inside (10,10), (16,16) and (30,30) nanotubes. The interaction strength between water molecules and the wall material of the pore, characterized by the Lennard-Jones potential well depth, was tuned to represent hydrophobic and hydrophilic behavior. The paper is organized as follows. In Section 2, the computational details and the methods are described, and in Section 3 the main results of the dynamic and structural properties of the confined water are discussed. Conclusions are presented in Section 4.

[a] *Instituto de Física, Universidade Federal do Rio Grande do Sul, Caixa Postal 15051, 91501-970, Porto Alegre, RS, Brazil. E-mail: mateus.kohler@ufrgs.br*
[b] *Campus Caapava do Sul, Universidade Federal do Pampa, v. Pedro Anunciacao 111, CEP 96570-000, Ca apava do Sul, Brazil. E-mail: josebordin@unipampa.edu.br*
[c] *Departamento de Física, Universidade Federal de Santa Maria, Av. Roraima, 1000, Santa Maria, RS, Brazil*

2 Computational details and methods

2.1 Water and nanotube models

Molecular dynamics were performed using the LAMMPS package[30] for simulations of TIP4P/2005 water[29] confined inside nanotubes. The nanotube atoms are arranged on a honeycomb lattice. Two atom types that differ only in their Lennard–Jones (LJ) parameters of interaction with water were used. They correspond to sp^2-hybridized carbon with ε_{CO} = 0.478 kJ mol^{-1} and σ_{CO} = 0.328 nm (labeled hydrophilic due to its water attractive character) and reduced carbon–water interaction strength with ε_{CO} = 0.27 kJ mol^{-1} and σ_{CO} = 0.341 (namely hydrophobic), as done in previous works.[11,23,31,32] We considered (n,n) nanotubes, with n = 10, 16 and 30. The choice of TIP4P/2005 over many other models available in the literature was due to its accuracy in calculating transport properties of water under ambient conditions.[29,33] We found the bulk viscosity to be 0.83 mPa s, and the diffusion coefficient was found to be 2.32×10^9 m^2 s^{-1}, in good agreement with previous studies.[34–37]

Periodic boundary conditions were applied to simulate isolated infinite nanotubes. Cutoff distances for LJ and coulomb interactions are 1.0 and 1.2 nm, respectively. Long-range coulomb interactions were handled using the particle–particle particle–mesh method.[38] The simulations were conducted in the *NVT* ensemble at a temperature of 300 K fixed by a Nosé–Hoover thermostat.[39,40] The system was equilibrated with a 15 ns simulation, followed by 15 ns of data accumulation. The timestep is 1 fs. In all simulations the geometry of water molecules was constrained by the SHAKE algorithm.[41] For simplicity, the positions of the carbon atoms are fixed, *i.e.*, not integrated. For each data point five independent simulations were carried out for average and standard deviation computation.

2.2 Simulation details

In order to properly evaluate the water density inside the nanotube, we define the effective diameter $d_{eff} = d - \sigma_{CO}$,[42,43] where d is the nominal diameter and σ_{CO} is the Lennard–Jones (LJ) parameter for the carbon–oxygen interaction. In terms of d_{eff}, the effective density is then given by

$$\rho_{eff} = \frac{M}{\pi \cdot \ell \cdot \left(\frac{d_{eff}}{2}\right)^2}, \quad (1)$$

where M is the total water mass in the pore and ℓ is the nanotube length. Fig. 1(a) shows a schematic depiction of the nominal and effective diameters of nanotube samples, while Fig. 1(b)–(d) shows the frontal view of the (10,10), (16,16) and (30,30) nanotubes, respectively, filled with water molecules.

We studied the dynamical and structural properties of water inside nanotubes with ρ_{eff} varying from 0.8 to 1.4 g cm^{-3}. In Table 1 the nanotube dimensions as well as the water filling details are presented.

2.3 Green–Kubo relations for shear viscosity

Thermal transport coefficients represent some of the most important properties of liquids. The large statistical uncertainties that accompany transport coefficient calculations and the long computational time necessary to reasonably reproduce the experimental results have been an obstacle for such simulations with liquids, especially in confinement. The most common method for calculating the shear viscosity η involves the Green–Kubo (G–K) relations:[44]

$$\eta = \frac{V}{k_B T}\int_0^\infty dt \langle P_{\alpha\beta}(t) P_{\alpha\beta}(0)\rangle,$$

$$P_{\alpha\beta} = \frac{1}{V}\left(\sum_{i=1}^{N}\frac{p_{i\alpha}p_{i\beta}}{m} + \sum_{i=1}^{N}\sum_{j>i}^{N} r_{ij\alpha} f_{ij\beta}\right), \quad (2)$$

where $P_{\alpha\beta}$ is the stress tensor, $r_{ij} = |\vec{r}_i - \vec{r}_j|$, $f_{ij} = -\partial U(r_{ij})/\partial r_{ij}$ and $\alpha, \beta \in (x,y,z)$ denotes Cartesian components. The stress tensor can be calculated inside the force calculation subroutine.

Viscosity is a collective property of the whole sample rather than of the individual molecules, so it cannot be calculated with the same accuracy as the diffusion coefficient. For a homogeneous fluid, the statistical error could be reduced by averaging over all the viscosity components. But the nanoconfinement (in our case, in x and y directions) hinders the glide of molecular layers, a necessary requirement for a shearing flow.[45] To analyze the behavior of these components, we consider the radial viscosity (coming from P_{xz} and P_{yz}) and the axial viscosity (from P_{xy}), which are related to the shear in the radial and axial directions, respectively. In nanotubes, due to the confinement in x and y directions, the radial components are shown to be almost zero,[46] while the axial component is shown to decrease

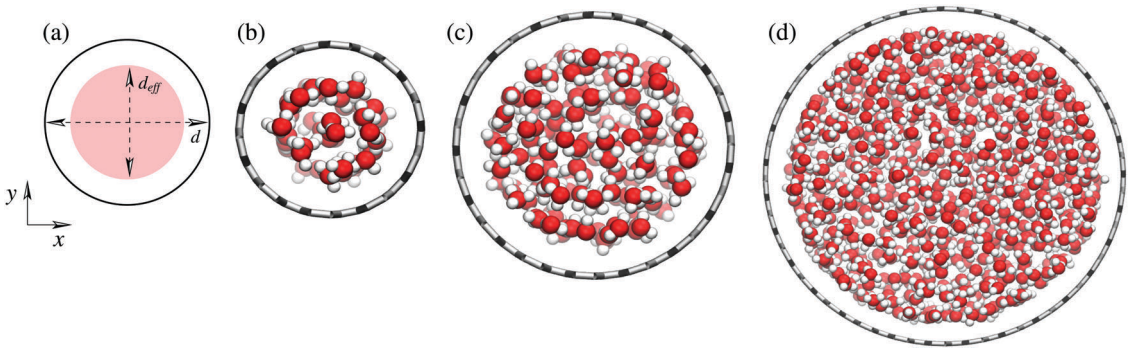

Fig. 1 (a) Definition of d_{eff} and d. Frontal view of a (b) (10,10), (c) (16,16) and (d) (30,30) nanotube filled with water.

Table 1 Nominal diameter d, length ℓ, number of enclosed molecules N and the range of effectivedensities (ρ_{eff}) for the nanotube samples

Chirality	d (nm)	ℓ (nm)	N	ρ_{eff} (g cm^{-3})
(10,10)	1.35	37.14	900–1260	0.87–1.25
(16,16)	2.17	11.07	911–1275	0.92–1.30
(30,30)	4.07	8.85	3115–4360	0.95–1.35

with the decrease of the nanotube diameter.[42] In particular, the viscosity dramatically decreases in very narrow tubes.[47,48] In fact, in very small-sized pores the radial components do not make sense, as the space is dimensionally restricted and the molecules hardly move in the x–y direction. The axial component, however, is the only sensible definition due to the obvious displacement, and the consequent shearing flow, in the axial direction. Therefore, in this work, the axial component (P_{xy}) was averaged to describe the viscosity of the fluids inside the nanopores. We have collected the stress tensor components at each timestep, in order to ensure maximum accuracy, with the upper limit of 40 ps. Following this, the converged auto-correlation functions (ACF) were integrated, as shown in Fig. 3.

2.4 Diffusion coefficient

The diffusion mechanism of a fluid can be analyzed by the scaling behavior between the mean squared displacement (MSD) and time:[44]

$$\langle|\vec{r}(t) - \vec{r}(0)|^2\rangle \propto Dt^{\alpha} \quad (3)$$

where $\langle|\vec{r}(t) - \vec{r}(0)|^2\rangle$ is referred as the MSD, the angular brackets denote an average over time origins and all water molecules, $\vec{r}(t)$ is the displacement of a molecule during the time interval t and D stands for the diffusion coefficient. The α exponent refers to the diffusion regime: $\alpha = 1$ for the linear Fickian diffusion, $\alpha > 1$ for supperdiffusive and $\alpha < 1$ for subdiffusive regime. In the bulk phase, the water molecules diffuse as the Fickian type while for the water confined in CNTs, the diffusion behavior becomes extraordinary due to the nanoscale confinement.[49] An alternative method for computing the diffusion coefficient involves the integration of the velocity auto-correlation functions (VACF); however, the Einstein relation, presented above, significantly reduces the computational time necessary for convergence.

As in the case of the viscosity calculations, the statistical error in the diffusion measurements could be reduced by averaging over all the MSD components. But the nanopore confinement in the x and y directions hinders the radial displacement of the molecules.[43] Therefore, the radial MSD is almost zero for all cases studied here and only the axial MSD will be considered. This component has been computed in the last 15 ns of simulation, and the diffusion D was obtained by a linear fit of MSD *versus* t.

3 Results and discussion

3.1 Stress tensor auto-correlation function

We have calculated water viscosity trough the equilibrium G–K relations. In this method, the main contribution comes from the tail of the stress tensor auto-correlation function (ACF), but

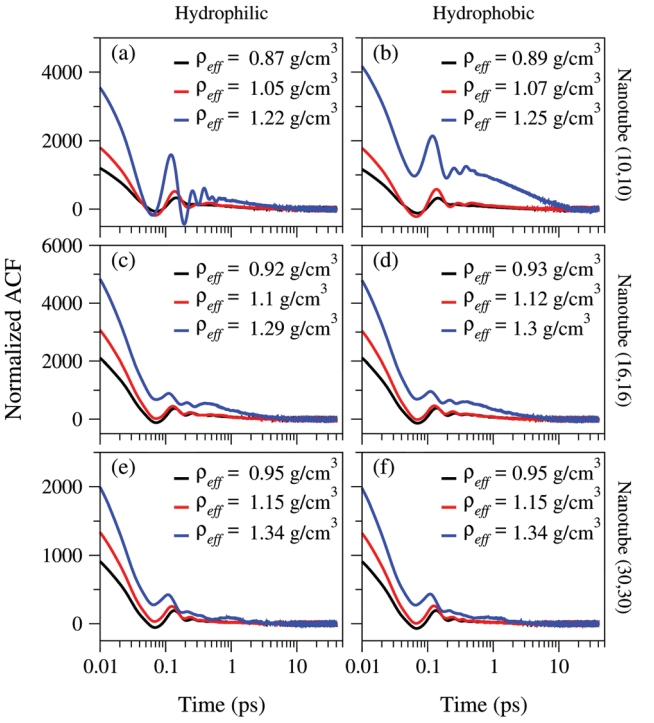

Fig. 2 Normalized auto-correlation functions for water confined in (a) and (b) (10,10) nanotube, (c) and (d) (16,16) nanotube and (e) and (f) (30,30) nanotube. Left panels show results for the hydrophilic confinement, while in the right we have the hydrophobic results.

an accurate computation of the shear viscosity also requires a precise calculation of the short time ACF. Fig. 2 shows the normalized ACFs of the non-diagonal components of the pressure tensor for confined water at 300 K. Five independent runs for each system were implemented in order to increase the statistics. We can notice two decay regimes, one for short times (fast scale), and another for higher times (slow scale of time). For each case, the fast scale part is monotonically decreasing, with an ACF decay faster than $1/t$. On the other hand, at larger times the ACF oscillates slowly while decreasing, except for the higher density case of water confined inside (10,10) hydrophobic nanotubes, that presents a large oscillation decrease with time. This behavior will, in turn, lead to several consequences related to the viscosity determination, as will be discussed throughout the paper.

A careful analysis of the case of SPC/E water model in bulk was made by Guo and Zhang.[50] Their results showed that the G–K relation leads to reliable results using an upper limit of the order of 3 ps in the integral of eqn (2). However, as Fig. 2 shows, depending on the water density for confined water, the calculations could require a higher correlation time. Particularly, for $\rho_{eff} > 1.2$ g cm^{-3} the ACF goes to zero only for correlation times higher than 10 ps. Density is not the only variable which leads to the requirement for higher integration times. When calculating viscosity for bulk water at different pressure conditions, Gonzalez and Abascal[35] also used higher time values for the integral of the ACFs. This indicates that thermodynamic parameters play an important role in the ACF calculations and,

consequently, on the precise determination of transport properties. We can also say that as the nanotube diameter increases the time required to the ACF convergence is shortened. It means that the confinement level is another important factor in calculating viscosity and should be handled carefully.

For the whole set of curves, the ACF is smaller as the density decreases, mainly in the fast time scale, with important contributions to the ACF integral. For all cases, as the density is increased the peaks become more pronounced and the oscillations are more persistent. We can also notice that as the nanotube diameter is decreased (higher confinement), the effect of density is enhanced, leading to larger oscillations for higher densities in the smaller (10,10) nanotube. The stressed situation in which more water molecules are enclosed in the nanopore leads to longer correlation between the stress components, and this is enhanced by the confinement level.

Regarding the water–wall interaction, the ACF of the water confined in hydrophobic nanotube is close to the hydrophilic case for the larger nanotubes. Only for the smaller (10,10) nanotube, the difference is enhanced at the higher density, $\rho_{\text{eff}} \sim 1.2\ \text{g cm}^{-3}$, and the hydrophobic confinement leads to a completely different behavior compared to the hydrophilic, leading the ACF to reach the convergence at times higher than 10 ps.

3.2 Shear viscosity of nanoconfined water

Fig. 3 shows the running values of the viscosities obtained by the integration of the normalized ACFs displayed in Fig. 2, for both water densities and for the hydrophilic and hydrophobic nanotubes. The upper limit in the integration to calculate the final values of viscosity is taken at the beginning of the plateau shown in Fig. 3(a)–(f). Despite the noise imposed by the hard convergence of the ACF tail, we can notice the convergence of the running viscosities at larger correlation times (~10–20 ps). This time is higher than the reported for bulk water (~1–5 ps).[35,50–52]

When confined in nanopores, water experiences an additional shear component with the wall, which is expected to play a significant role in the viscosity prediction.[47] Besides this, since we compute only the axial component of the viscosity, the statistical accuracy is affected and longer simulations are required to achieve the equilibrium condition necessary to the use of G–K relations. All the panels in Fig. 3 shows that the convergence is clearly affected by the density: higher is the density, larger correlation times are required. In fact, as the number of water molecules inside the pore is increased, the shear between water layers is increased, which in turn leads to a higher perturbation regime and longer simulations are necessary to obtain accurate values of viscosity.

3.3 The Stokes–Einstein relation

In the Fig. 4, we show the behavior of the viscosity, η, and of the diffusion coefficient, D, as a function of the density for (10,10), (16,16) and (30,30) hydrophobic and hydrophilic nanotubes. As discussed in the Section 2, the radial MSD is almost zero and only the axial diffusion D_z is shown in Fig. 4(b), (d) and (f).

In principle, the Stokes–Einstein relation for translational diffusion from the kinetic theory[53]

$$D = \frac{k_B T}{6\pi\eta\sigma^3}, \tag{4}$$

has no grounds to be valid in confined systems. However, one could expect intuitively that the increase in the viscosity would imply a slowing down of the diffusion. The comparison

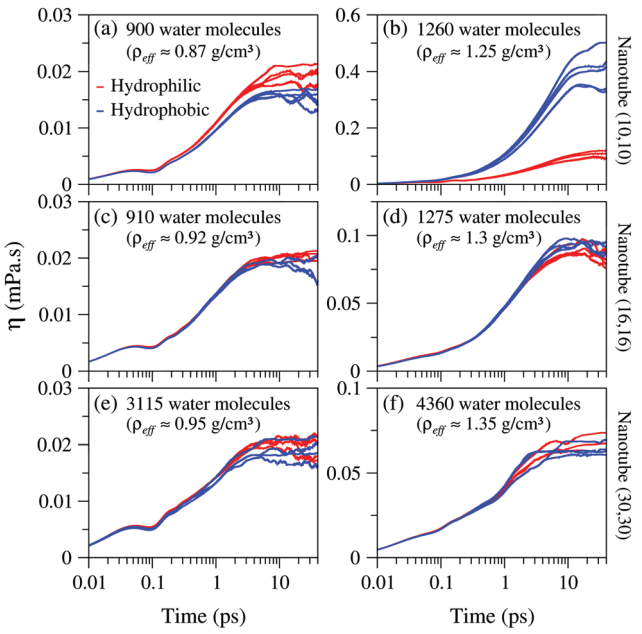

Fig. 3 Viscosity, η, *versus* time for (a) and (b) (10,10), (c) and (d) (16,16) and (e) and (f) (30,30) nanotubes.

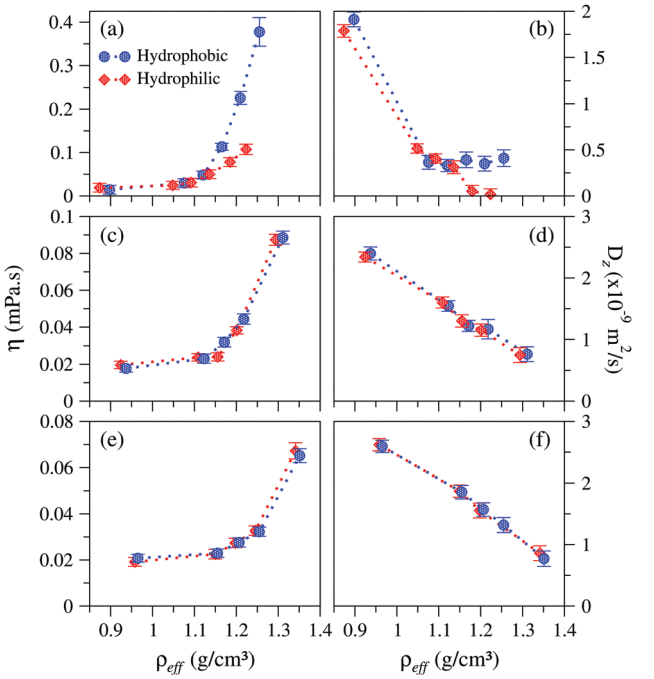

Fig. 4 Left panel: Viscosity, η as a function of the density, effective density. Right panel: Axial diffusion D_z as a function of density. Both panels are for (a) and (b) (10,10), (c) and (d) (16,16), and (e) and (f) (30,30) nanotubes.

between the viscosity and the diffusion illustrated in Fig. 4 indicates that the Stokes–Einstein relation and the intuitive assumption that the diffusion decorrelates with the viscosity are valid for all the systems with the exception of the (10,10) hydrophobic nanotubes. This decorrelation have been observed in supercooled liquids,[54,55] confined water and methanol-diluted bulk water.[56] Now, we extend the understanding of this decorrelation for distinct nanopores.

For the larger nanotube diameters, (16,16) and (30,30), whether the pore is hydrophobic or hydrophilic does not affect the water viscosity or diffusion, which is consistent with a previous analysis.[42] However, for the narrow (10,10) nanotube, the viscosity shows an increase for hydrophobic nanotubes that is 4 times larger than in the hydrophilic case. This difference means that the shear between layers of water molecules is strongly dependent on the pore hydrophobicity, and this dependence is activated with increasing density. For this narrow tube, Fig. 4 also shows that the increase in the density above $\rho_{\mathrm{eff}} \sim 1.1$ g cm^{-3} leads to a small increase in the diffusion coefficient while it increases the viscosity of the system, violating the Stokes–Einstein relation.

In all the three nanotube diameters the viscosity changes its slope at densities between 1.1–1.2 g cm^{-3}, as shown in Fig. 4. As we will see next, the mechanism behind this change of slope is related to the structure adopted by the water molecules inside the tubes.

3.4 Structure of nanoconfined water

The transport properties of fluids inside nanopores have a strong dependence on the molecules' structure.[28,57–59] The Fig. 5 illustrates the radial density profiles of the water molecules inside the hydrophobic (blue lines) and the hydrophilic nanotubes (red lines). Two densities were selected, one below the change of the slope in the viscosity and one above. Fig. 5 shows that the change in the increase of the viscosity with the density is connected to the change in the number of layers inside the tube. While for low densities one contact layer and a large central layer are formed, at high densities the system forms a number of layers. This transition between one central layer to many layers occurs at some point between $\rho_{\mathrm{eff}} \sim 1$–$1.2$ g cm^{-3}, which coincides with the density of the change of slope in Fig. 4.

Fig. 5 also shows that, regardless of whether it is hydrophobic or hydrophilic, the smaller (10,10) nanotube leads to the formation of two concentric layers at higher densities. This change in the number of layers as the density increases results in very different effects in the viscosity and in the diffusion coefficient.

For the hydrophobic nanotube, illustrated in the Fig. 6(a), the water forms a disordered central layer which maximizes the number of hydrogen bonds already for a density that is not too high. This nonstructured layer allows for an increase in the viscosity. However, since the water–wall interaction is repulsive, the two layers move as a global structure and the diffusion coefficient is non-zero even for high densities. Therefore, the decoupling between the viscosity and the diffusion, as well as

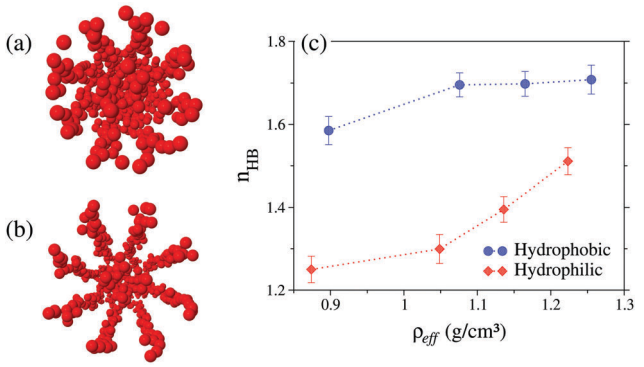

Fig. 6 The snapshot of the last configuration for the (a) hydrophobic and the (b) hydrophilic (10,10) nanotube. For clarification, only the oxygen atoms are shown. In (c) we show the average number n_{HB} of hydrogen bonds per water molecule for the hydrophobic (blue) and the hydrophilic (red) confinement.

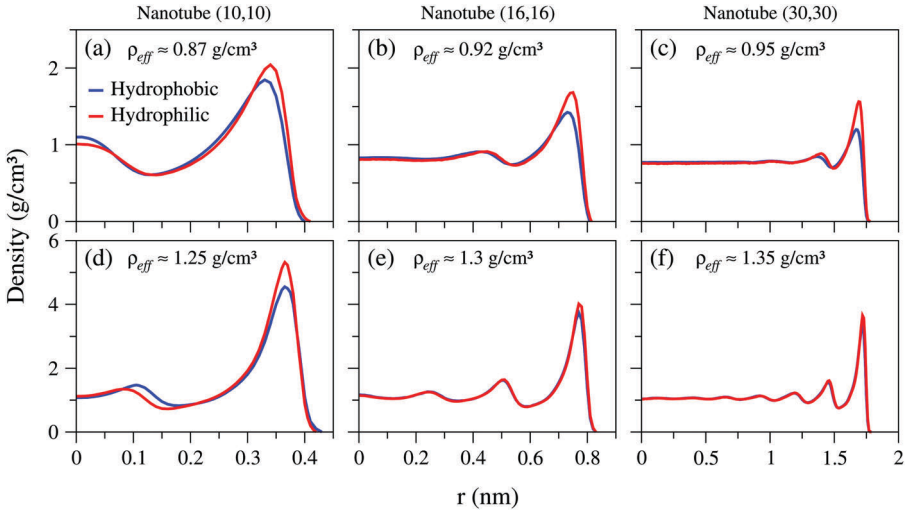

Fig. 5 Radial density distribution of oxygen atoms inside: (a) and (d) (10,10), (b) and (e) (16,16), and (c) and (f) (30,30) nanotubes, where $r = 0$ is at the center of the tube. The upper figures show the lower density results, while the bottom refers to the higher densities.

the violation of the Stokes–Einstein relation for the hydrophobic (10,10) nanotube at high densities is related to the high connectivity of water inside this tube and to the unbinding of the molecules with the wall, which defines a viscous internal dynamics and the diffusion of the whole structure.

In the case of the hydrophilic nanotube, shown in Fig. 6(b), water forms two very ordered concentric tubes with the number of bonds increasing with the increase of the density, while the mobility decreases. Since the system exhibits only two well defined layers, the viscosity increases smoothly. The diffusion coefficient, in this case, has two dynamics. The central layer moves at distinct velocity than the contact layer.[28,60] At high densities, the contact layer forms an ice-like structure and the overall mobility goes to zero.

4 Conclusions

In summary, we have calculated the viscosity and diffusion for water confined in nanotubes of different sizes. The interaction strength between water molecules and the wall material of the pore, characterized by the Lennard–Jones potential well depth, was tuned to represent the hydrophobic and hydrophilic behaviors. The viscosity calculations have been shown to depend on factors such as density, confinement size, and the water–wall interaction. A transition in the viscosity dependence with density has been found for both hydrophobic and hydrophilic nanotubes. Nevertheless, a dramatic increase in viscosity takes place for the narrow hydrophobic pore, reaching 4 times the viscosity of the hydrophilic case.

We have also identified a violation of the Stokes–Einstein relation for water confined in narrow hydrophobic nanotubes. Our findings show that the transport properties of water will only be affected by the wall properties inside narrow nanopores, where there is no space for a central liquid layer.

Acknowledgements

The authors acknowledge Brazilian science agencies CAPES and CNPq for financial support.

References

1 E. Secchi, S. Marbach, A. Nigues, D. Stein, A. Siria and L. Bocquet, *Nature*, 2016, **537**, 210–213.
2 M. Ma, F. Grey, L. Shen, M. Urbakh, S. Wu, J. Z. Liu, Y. Liu and Q. Zheng, *Nat. Nanotechnol.*, 2015, **10**, 692–695.
3 X. Qin, Q. Yuan, Y. Zhao, S. Xie and Z. Liu, *Nano Lett.*, 2011, **11**, 2173–2177.
4 D. Lu, *Phys. Chem. Chem. Phys.*, 2013, **15**, 14447–14457.
5 R. Das, S. B. A. Hamid, M. E. Ali, A. F. Ismail, M. Annuar and S. Ramakrishna, *Desalination*, 2014, **354**, 160–179.
6 B. Lee, Y. Baek, M. Lee, D. H. Jeong, H. H. Lee, J. Yoon and Y. H. Kim, *Nat. Commun.*, 2015, **6**, 7109.
7 M. F. L. De Volder, S. H. Tawfick, R. H. Baughman and A. J. Hart, *Science*, 2013, **339**, 535–539.
8 M. Verma and P. A. Deshpande, *Phys. Chem. Chem. Phys.*, 2017, **19**, 8757–8767.
9 S. F. Liu, S. Lin and T. M. Swager, *ACS Sens.*, 2016, **1**, 354–357.
10 M. Dionisio, J. M. Schnorr, V. K. Michaelis, R. G. Griffin, T. M. Swager and E. Dalcanale, *J. Am. Chem. Soc.*, 2012, **134**, 6540–6543.
11 G. Hummer, J. C. Rasaiah and J. P. Noworyta, *Nature*, 2001, **414**, 188–190.
12 M. Majunder, N. Chopra, R. Andrews and B. J. Hinds, *Nature*, 2005, **438**, 44.
13 J. K. Holt, H. G. Park, Y. M. Wang, M. Stadermann, A. B. Artyukhin, C. P. Grigoropulos, A. Noy and O. Bakajin, *Science*, 2006, **312**, 1034–1037.
14 S. Guo, E. R. Meshot, T. Kuykendall, S. Cabrini and F. Fornasiero, *Adv. Mater.*, 2015, **27**, 5726–5737.
15 L. Mandeltort, D.-L. Chen, W. A. Saidi, J. K. Johnson, M. W. Cole and J. T. Yates, *J. Am. Chem. Soc.*, 2013, **135**, 7768–7776.
16 D. Roy, N. Tiwari, M. Gupta, K. Mukhopadhyay and A. K. Saxena, *J. Phys. Chem. C*, 2015, **119**, 716–723.
17 M. Meyyappan, *Small*, 2016, **12**, 2118–2129.
18 A. Thamri, H. Baccar, C. Struzzi, C. Bittencourt, A. Abdelghani and E. Llobet, *Sci. Rep.*, 2016, **6**, 35130.
19 J.-J. Adjizian, R. Leghrib, A. A. Koos, I. Suarez-Martinez, A. Crossley, P. Wagner, N. Grobert, E. Llobet and C. P. Ewels, *Carbon*, 2014, **66**, 662–673.
20 N. G. Chopra, R. J. Luyken, K. Cherrey, V. H. Crespi, M. L. Cohen, S. G. Louie and A. Zettl, *Science*, 1995, **269**, 966–967.
21 M. H. Köhler, R. C. Barbosa, L. B. da Silva and M. C. Barbosa, *Physica A*, 2017, **468**, 733–739.
22 P. Gallo, M. Rovere and S. Chen, *J. Phys.: Condens. Matter*, 2010, **22**, 284102.
23 I. Moskowitz, M. A. Snyder and J. Mittal, *J. Chem. Phys.*, 2014, **141**, 18C532.
24 J. R. Bordin and M. C. Barbosa, *Physica A*, 2017, **467**, 137–147.
25 M. Melillo, F. Zhu, M. A. Snyder and J. Mittal, *J. Phys. Chem. Lett.*, 2011, **2**, 2978–2983.
26 M. Neek-Amal, F. M. Peeters, I. V. Grigorieva and A. K. Geim, *ACS Nano*, 2016, **10**, 3685–3692.
27 G. Tocci, L. Joly and A. Michaelides, *Nano Lett.*, 2014, **14**, 6872–6877.
28 J. R. Bordin, A. Diehl and M. C. Barbosa, *J. Phys. Chem. B*, 2013, **117**, 7047–7056.
29 J. L. F. Abascal and C. Vega, *J. Chem. Phys.*, 2005, **123**, 234505.
30 S. Plimpton, *J. Comput. Phys.*, 1995, **117**, 1–19.
31 A. Waghe, J. C. Rasaiah and G. Hummer, *J. Chem. Phys.*, 2002, **117**, 10789.
32 S. Sriraman, I. G. Kevrekidis and G. Hummer, *Phys. Rev. Lett.*, 2005, **95**, 130603.
33 Y. Mao and Y. Zhang, *Chem. Phys. Lett.*, 2012, **542**, 37–41.
34 K. R. Harris and L. A. Woolf, *J. Chem. Eng. Data*, 2004, **49**, 1064–1069.
35 M. Gonzalez and J. Abascal, *J. Chem. Phys.*, 2010, **132**, 096101.
36 K. Krynicki, C. D. Green and D. W. Sawyer, *Faraday Discuss. Chem. Soc.*, 1978, **66**, 199–208.

37 L. Liu and G. N. Patey, *J. Chem. Phys.*, 2016, **144**, 184502.
38 M. Deserno and C. Holm, *J. Chem. Phys.*, 1998, **109**, 7678–7693.
39 S. Nosé, *Mol. Phys.*, 1984, **52**, 255.
40 W. G. Hoover, *Phys. Rev. A: At., Mol., Opt. Phys.*, 1985, **31**, 1695.
41 J. P. Ryckaert, G. Ciccotti and H. J. C. Berendsen, *J. Comput. Phys.*, 1977, **23**, 327–341.
42 M. H. Köhler and L. B. da Silva, *Chem. Phys. Lett.*, 2016, **645**, 38–41.
43 J. R. Bordin, A. B. de Oliveira, A. Diehl and M. C. Barbosa, *J. Chem. Phys.*, 2012, **137**, 084504.
44 M. P. Allen and D. J. Tildesley, *Computer simulation of liquids*, Oxford University Press, 1989, p. 408.
45 Y. Liu, Q. Wang, T. Wu and L. Zhang, *J. Chem. Phys.*, 2005, **123**, 234701.
46 Y. Liu and Q. Wang, *Phys. Rev. B: Condens. Matter Mater. Phys.*, 2005, **72**, 085420.
47 X. Chen, G. Cao, A. Han, V. K. Punyamurtula, L. Liu, P. J. Culligan, T. Kim and Y. Qiao, *Nano Lett.*, 2008, **8**, 2988–2992.
48 J. S. Babu and S. P. Sathian, *J. Chem. Phys.*, 2011, **134**, 194509.
49 J. R. Bordin, L. B. Krott and M. C. Barbosa, *J. Chem. Phys.*, 2014, **141**, 144502.
50 G.-J. Guo and Y.-G. Zhang, *Mol. Phys.*, 2001, **99**, 283–289.
51 J. Medina, R. Prosmiti, P. Villarreal, G. Delgado-Barrio, G. Winter, B. González, J. Alemán and C. Collado, *Chem. Phys.*, 2011, **388**, 9–18.
52 G. S. Fanourgakis, J. S. Medina and R. Prosmiti, *J. Phys. Chem. A*, 2012, **116**, 2564.
53 A. Einstein, *Investigations on the theory of Brownian movement*, Dover Publications, New York, 1956.
54 G. Tarjus and D. Kivelson, *J. Chem. Phys.*, 1995, **103**, 3071–3073.
55 S. H. Chen, F. Mallamace, C. Y. Mou, M. Broccio, C. Corsaro, A. Faraone and L. Liu, *Proc. Natl. Acad. Sci. U. S. A.*, 2006, **103**, 12974.
56 F. Mallamace, C. Branca, C. Corsaro, N. Leone, J. Spooren, H. E. Stanley and S. H. Chen, *J. Phys. Chem. B*, 2010, **114**, 1870.
57 J. R. Bordin, J. S. Soares, A. Diehl and M. C. Barbosa, *J. Chem. Phys.*, 2014, **140**, 194504.
58 K. Zhao and H. Wu, *Phys. Chem. Chem. Phys.*, 2015, **17**, 10343–10347.
59 E. Wagemann, E. Oyarzua, J. H. Walther and H. A. Zambrano, *Phys. Chem. Chem. Phys.*, 2017, **19**, 8646–8652.
60 J. Hassan, G. Diamantopoulos, L. Gkoura, M. Karayanni, S. Alhassan, M. S. Katsiotis, T. Karagiannis, M. Fardis, N. Panopoulos, H. J. Kim and G. Papavassiliou, 2016, arXiv:1612.01161.

Appendix B

Physica A 490 (2018) 331–337

Contents lists available at ScienceDirect

Physica A

journal homepage: www.elsevier.com/locate/physa

Structure and dynamics of water inside hydrophobic and hydrophilic nanotubes

Mateus Henrique Köhler [a,*], José Rafael Bordin [b], Leandro B. da Silva [c], Marcia C. Barbosa [a]

[a] Instituto de Física, Universidade Federal do Rio Grande do Sul, Caixa Postal 15051, 91501-970, Porto Alegre, Brazil
[b] Campus Caçapava do Sul, Universidade Federal do Pampa, 96570-000, Caçapava do Sul, Brazil
[c] Departamento de Física, Universidade Federal de Santa Maria, Santa Maria, Brazil

HIGHLIGHTS

- Water structure and dynamics are strongly influenced by polarity.
- The influence is negligible for wider nanotubes.
- At low density, water present smaller diffusion than at higher densities.

ARTICLE INFO

Article history:
Received 25 April 2017
Available online 1 September 2017

Keywords:
Confined water
Water diffusion
Hydrophobicity
Hydrophilicity

ABSTRACT

We have used Molecular Dynamics simulations to investigate the structure and dynamics of TIP4P/2005 water confined inside nanotubes. The nanotubes have distinct sizes and were built with hydrophilic or hydrophobic sites, and we compare the water behavior inside each nanotube. Our results shows that the structure and dynamics are strongly influenced by polarity inside narrow nanotubes, where water layers were observed, and the influence is negligible for wider nanotubes, where the water has a bulk-like density profile. As well, we show that water at low density can have a smaller diffusion inside nanotubes than water at higher densities. This result is a consequence of water diffusion anomaly.

1. Introduction

Since its discovery [1], carbon nanotubes (CNTs) has emerged as promising model systems for nanoconfinement studies of fluids. In this respect, it has been used in a wide range of applications such as water filtration [2], single-molecule sensors [3], ion selectivity [4], and energy conversion and storage [5]. In the case of nanoconfined water solutions the efficiency of the system is determined by the water–CNT interaction. This assumption can be tested by applying electric fields [6], decorating CNT walls [7], adding surfactants [8] and many others synthetization procedures.

Although not expected, the hydrophobic inner of a pristine CNT allows the water molecules not just to enter the nanotube cavity [9] but also to present a flow rate that exceeds by three orders of magnitude the values predicted by the continuum hydrodynamics theory [10,11]. Tuning the water–CNT interaction, by making it more hydrophilic or hydrophobic, is important either to achieve higher water permeation or to induce it to experience structural and dynamical transitions [12]. However, the impact of hydrophobicity over water structure and dynamics is also under debate and may lead to significant

* Corresponding author.
E-mail address: mateus.kohler@ufrgs.br (M.H. Köhler).

http://dx.doi.org/10.1016/j.physa.2017.08.030
0378-4371/

changes in its behavior [13–15]. The synthesis of chemically functionalized nanotubes with hydrophobic and hydrophilic sites [16], as in biological channels [17], adds even more complexity to this picture and presents an opportunity to study the effect of polarity heterogeneity over confined water properties.

By providing site-specific details of water properties, molecular dynamics (MD) simulations has been proved useful in the study of local structuration and quantification of water flux inside heterogeneous nanotubes [18–21]. Moskowitz and colleagues [22] has found that both the occupancy and the water flux are more sensitive to the fraction of hydrophilic atoms than to its arrangement. However, when located in the tube entrance, the hydrophobic atoms can play some role, lowering the filling rate [19]. Recently, by tuning the strength of water–nanotube attractions, Xu and his group [18] has found a maximal flow when empty states are present in the inner of the nanotube, which is unexpected since in this situation the wired hydrogen-bonding network (prerequisite for high water permeability) is broken.

In the present study we use MD simulations to examine the impact of nanotube polarity over the mobility and structure of the confined water molecules at different density regimes. Hydrophobic and hydrophilic atoms were distributed in a honeycomb lattice to form the model tubular nanochannel. The size effect is also evaluated by varying the nanotube diameter. The paper is organized as follows. In Section 2, the computational details and the methods are described, in Section 3 the main results of the dynamic and structural properties of the confined water are discussed. Conclusions are presented in Section 4.

2. Methods

2.1. Water and nanotube models

Molecular dynamics were performed using the LAMMPS package [23] for simulations of TIP4P/2005 water [24] confined inside nanotubes. The nanotube atoms are arranged on a honeycomb lattice. Two different atom types were used to build the nanotube. These two atom types differ only by their Lennard-Jones (LJ) parameters of interaction with water, and correspond to sp^2-hybridized carbon with $\varepsilon_{CO} = 0.478$ kJ/mol and $\sigma_{CO} = 0.328$ nm (labeled hydrophilic due to water attractive character) and reduced carbon–water interaction strength with $\varepsilon_{CO} = 0.27$ kJ/mol and $\sigma_{CO} = 0.341$ (namely hydrophobic), as done in previous works [12,22]. We considered (n, n) nanotubes, with $n = 10$, 16 and 30. The choice of TIP4P/2005 over many other models available in the literature was due to its accuracy in calculating transport properties of water at ambient conditions [24,25]. Particularly for the diffusion coefficient, we have found 2.32×10^9 m^2/s, which is in close agreement to previous theoretical [26] and experimental works [27].

Periodic boundary conditions were applied to simulate isolated infinite nanotubes. Cutoff distances for LJ and Coulomb interactions are 1.0 and 1.2 nm, respectively. Long-range Coulomb interactions was handled using particle–particle particle–mesh method [28]. The simulations were conducted in the NVT ensemble at temperature 300 K fixed by a Nosé-Hoover thermostat [29,30]. The system was equilibrated with a 15 ns simulation, followed by 15 ns of data accumulation. The timestep is 1 fs. In all simulations the geometry of water molecules was constrained by the SHAKE algorithm [31].

2.2. Simulational details

The water radial density profile was evaluated by dividing the inner of the nanotube in concentric cylindrical shells and averaging the number of oxygen atoms in each shell along the simulation.

The diffusion mechanism of a fluid can be reflected by the scaling behavior between the mean squared displacement (MSD) and time [32]:

$$\left\langle \left|\vec{r}(t) - \vec{r}(0)\right|^2 \right\rangle \propto Dt^{\alpha} \tag{1}$$

where $\left\langle \left|\vec{r}(t) - \vec{r}(0)\right|^2 \right\rangle$ is referred as the MSD, $\langle\rangle$ denotes an average over all the molecules and $\vec{r}\,(t)$ is the displacement of a molecule during the time interval t. The α exponent refers to the diffusion regime: $\alpha = 1$ for the linear Fickian diffusion, $\alpha > 1$ for superdiffusive and $\alpha < 1$ for subdiffusive regime. In the bulk phase, the water molecules diffuse as the Fickian type while for the water confined in CNTs, the diffusion behavior becomes extraordinary due to the nanoscale confinement [20,33].

For a fluid, the statistical error could be reduced by averaging over all the MSD components. But the nanopore confinement in the x and y directions hinders the radial displacement of the molecules. Therefore, The radial MSD is almost zero for all cases studied here and only the axial MSD will be considered.

We use the effective diameter [34]

$$d_{eff} = d - \sigma_{\mathrm{CO}},$$

where d is the nominal diameter and σ_{CO} is the Lennard-Jones (LJ) parameter for carbon–oxygen interaction. to calculate the water density inside the nanotube. In terms of d_{eff}, the effective density is then given by

$$\rho_{eff} = \frac{M}{\pi \cdot \ell \cdot \left(\frac{d_{eff}}{2}\right)^2}, \tag{2}$$

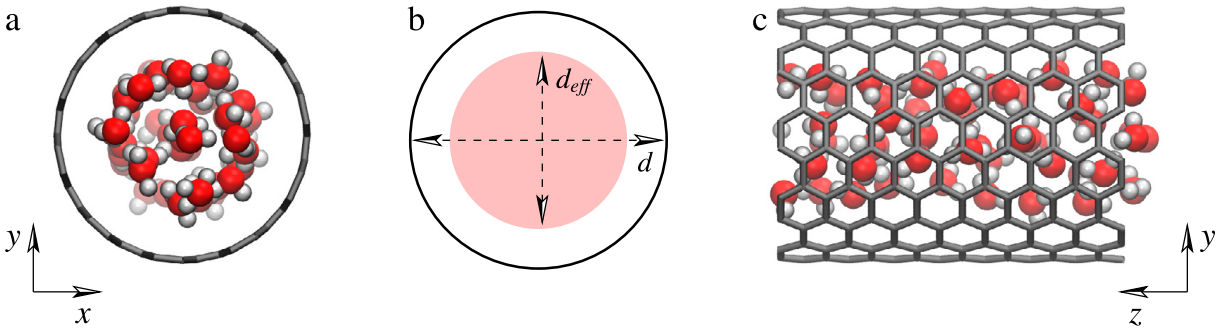

Fig. 1. (a) (10,10) nanotube filled with water and (b) definition of d_{eff} and d. In (c) we can see a side view of the nanotube.

Table 1
Nominal diameter d, length ℓ, number of enclosed molecules N and the range of *effective densities* (ρ_{eff}) for the nanotube samples.

Chirality	d (nm)	ℓ (nm)	N	ρ_{eff} (g/cm^{-3})
0.92(10,10)	1.35	37.14	540–1260	0.53–1.25
0.92(16,16)	2.17	11.07	550–1275	0.55–1.30
0.92(30,30)	4.07	8.85	1870–4360	0.57–1.35

where M is the total water mass into the pore and ℓ is the nanotube length. In Fig. 1(b) we represent the nominal and effective diameters of nanotube samples.

Based on our previous work [34], we have chosen three representative effective densities for the selected nanotubes. In Table 1 the nanotube chirality, nominal diameter d, length ℓ, number of enclosed water molecules N and the considered effective densities ρ_{eff} are presented.

3. Results and discussion

3.1. Water structure

Water structure and dynamics under hydrophobic and hydrophilic confinement is relevant to understand and develop new technologies, as well to understand aspects of life and basic science. In proteins, non-polar cavities are often located at the active site and are thought to be involved in the uptake, transfer, and release of both non-polar and polar molecules [35]. Markedly, non-polar or weakly polar pores play a prominent role in aquaporin water channels [36]. In such systems, water occupies their weakly polar pores at least transiently, exhibiting anomalous diffusion and dipoles aligned with the transmembrane axis. The pore polarity is therefore an important ingredient in the confined water properties.

In order to understand the behavior of water confined in hydrophobic and hydrophilic nanotubes at different densities, we first discuss the water molecules arrangement inside these structures. For the lower densities, $\rho_{eff} \sim 0.5$ g/cm^3, water organizes in semi-filled states with formation of bubble-like structures in hydrophilic and hydrophobic pores, as can be seen in Fig. 2. Here, we can see that the bubble inside hydrophilic nanopore is more compact than in the hydrophobic case. This indicates that the wall–water interaction affects the molecules structure in the axial direction. Hummer and co-workers [12] have highlighted the existence of sharp, two-state transitions between empty and filled states of water in such rigid hydrophobic structures. In fact, the density of water inside nanopores can be tuned by electric fields [37,38], applied pressure [39] or even functionalization [40].

This arrangement makes the water molecules more susceptible to the wall hydrophilicity, since the water–water interactions are weakened. It becomes clear in Fig. 3, where we show the density radial distribution profile for the three different nanopore radii.

Fig. 3(a), (b) and (c) reveals that, for the lower densities and all nanopore radii, the water inside the hydrophilic pore is more structured than inside the hydrophobic nanotube. For all nanotube radii, in the hydrophilic confinement the water molecules are strongly attracted to the water–wall interface, presenting a dense packing arrangement. This is not so evident for the hydrophobic confinement, where the water molecules present a more distributed density profile. For the narrowest (10,10) nanopore the water forms a concentric layer near the wall with a single line of molecules in the center. As the radius increases for the (16,16) and (30,30) nanotubes the water shows two concentric layer near the nanotube wall and a bulk-like profile in the nanotube center for hydrophilic nanopores, and only one concentric layer near the wall for the hydrophobic case. This indicates that, for low densities, the water structure inside chemically functionalized nanotubes is distinct from the observed for carbon nanotubes.

Increasing the density, at density ~ 0.9 g/cm^3, the radial density distribution, shown in Fig. 3(d), (e) and (f), indicates that the water molecules are more packed in the hydrophilic wall than in the hydrophobic. However, the number of layers is now

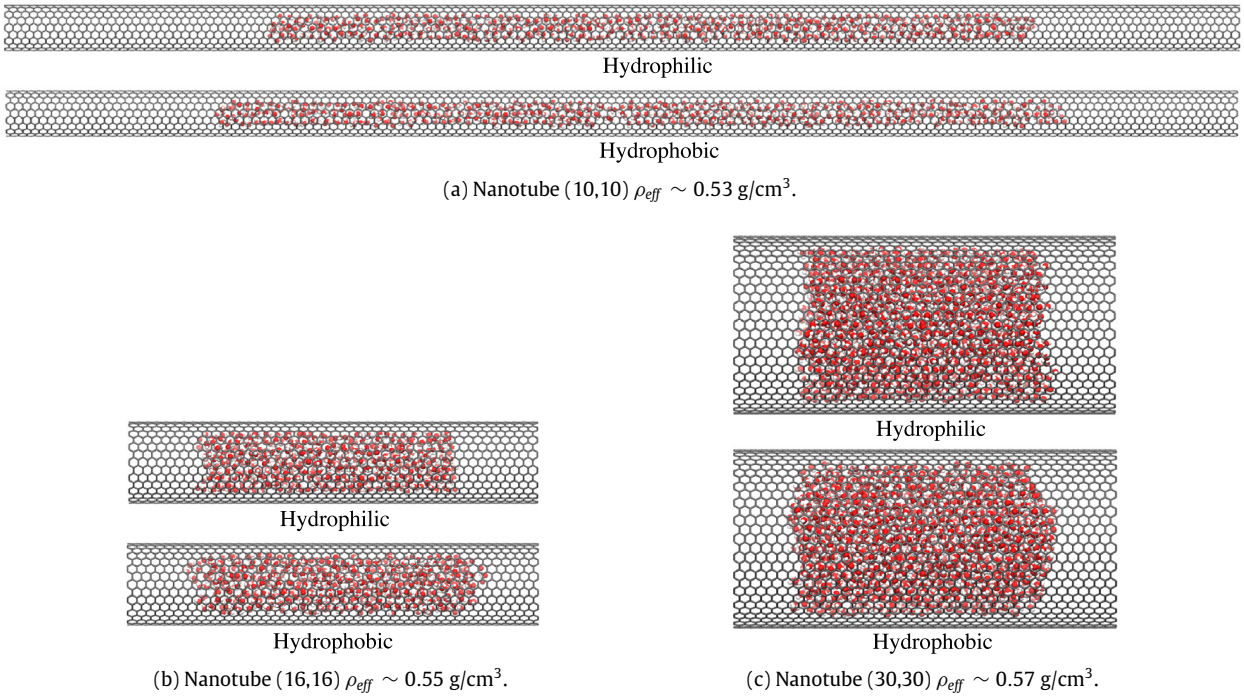

Fig. 2. Snapshot of the lowest ρ_{eff} for both hydrophilic and hydrophobic (a) (10,10), (b) (16,16) and (c) (30,30) nanotube.

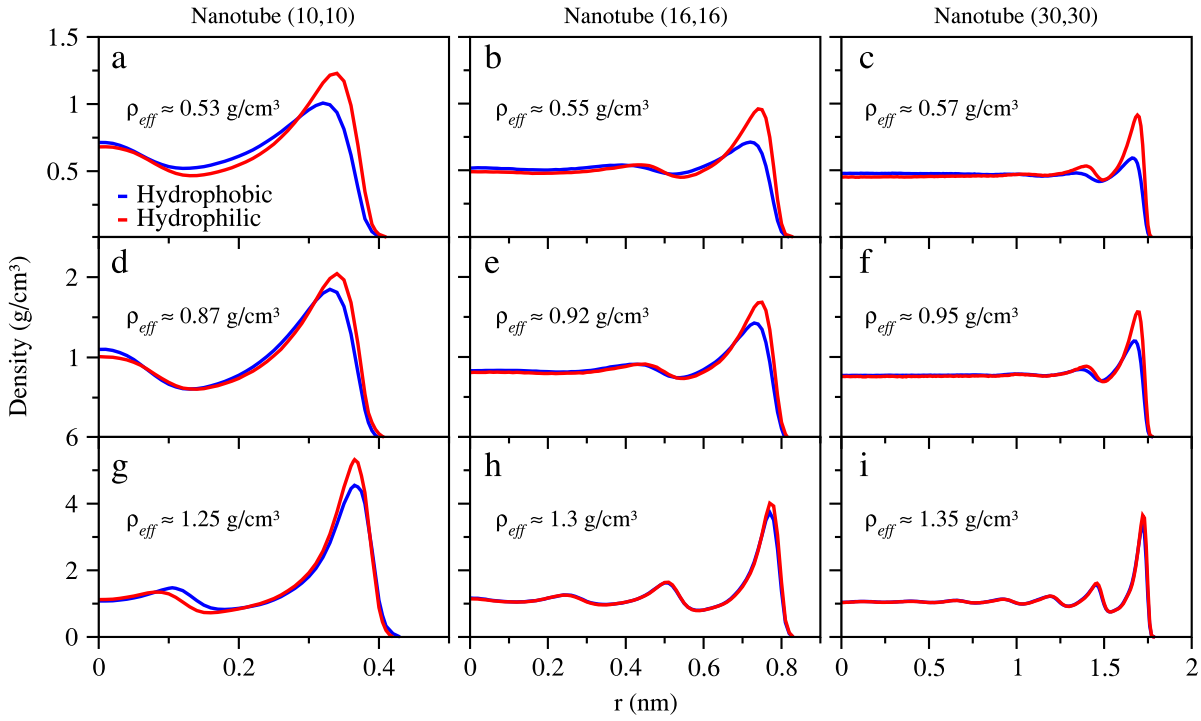

Fig. 3. Radial density distribution of oxygen atoms inside: (a) (10,10), (b)(16,16) and (c) (30,30) nanotubes, where r = 0 is at the center of the tube.

the same in all the cases. Inside (10,10) nanotubes, the water is structured in a concentric layer near the wall with a single line of molecules in the center. For (16,16) and (30,30) nanotubes the water have two concentric layers near the wall and a bulk-like profile in the center. However, the second layer for hydrophobic confinement is slightly shifted to the center of the nanotube. Therefore, for densities ∼ 0.9 g/cm^3 the water–wall interaction affects the contact and the second layer, leading to a higher packing for hydrophilic nanopores, in agreement with first principle computational studies [41].

When the density is ∼ 1.3 g/cm^3 we only observe a significant difference in the water structure for the (10,10) nanotube, Fig. 3(g). In this case, the central layer is strongly affected. For hydrophobic nanopores it is more close to the wall than

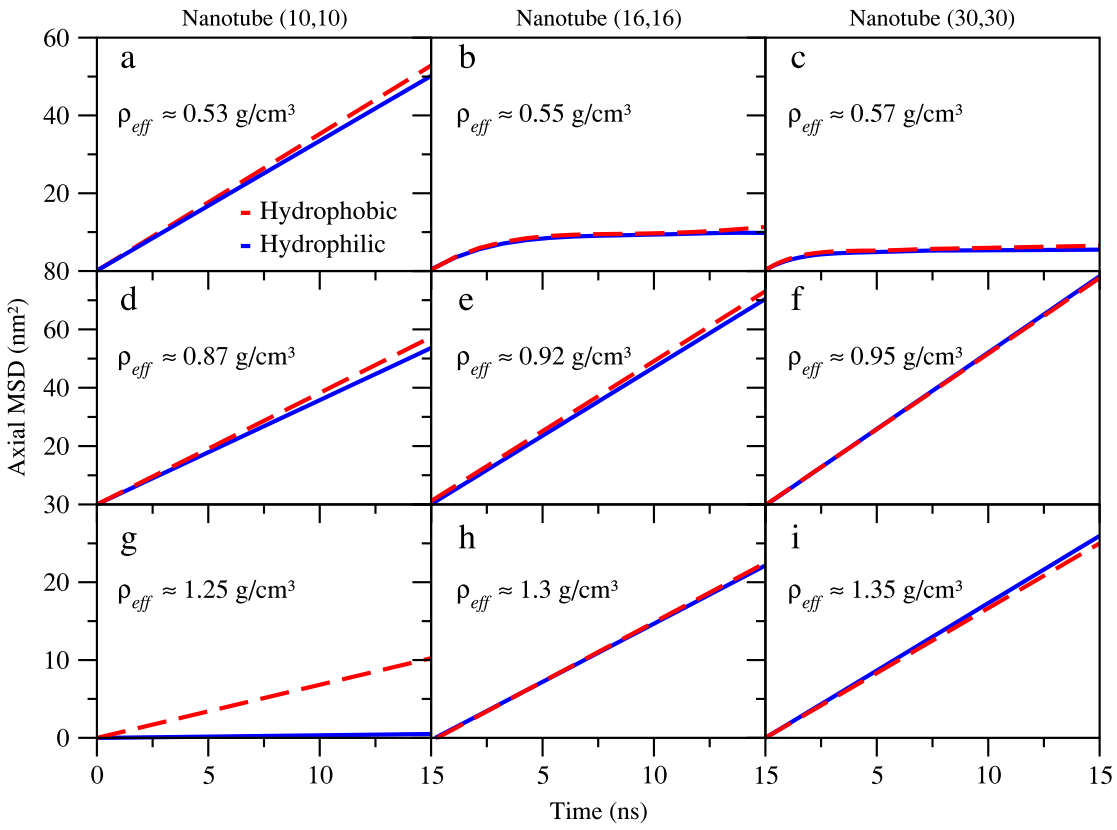

Fig. 4. Time evolution of the mean squared displacement of water oxygen atoms for some selected effective densities. The solid line stands for hydrophilic water–nanotube interaction and the dashed line for the hydrophobic interaction.

for the hydrophilic case. Inside wider nanopores, shown in Fig. 3(h) and (i), only the contact layer has a small difference, and a layered structure was obtained—4 layers inside (16,16) nanotubes and 5 concentric layers with a central bulk-like fluid for (30,30) nanotubes. This shows that at high densities the wall–water interaction is overcome by the water–water interaction. These results are relevant for biological channels and chemically modified nanotubes with polar and apolar sites, since it shows that the water structure near these sites will be affected not only by the water–wall interaction, but the water density inside the channel also plays a major role.

3.2. Water diffusion

Fluids structure and diffusion inside nanopores are strongly related [42–45]. Therefore, distinct structural regimes can lead to different diffusive behaviors. In Fig. 4, we present the axial MSD curves for water at selected densities filling (10,10), (16,16) and (30,30) nanotubes. Particularly, the diffusive regime can be defined by the scaling factor between the MSD and the exponent of time, t^{α}. For regular, or Fick, diffusive process, $\alpha = 1.0$. If $\alpha > 1.0$ we say that the system is superdiffusive, and if $\alpha < 1.0$ the regime is subdiffusive.

When $\rho_{eff} \sim 0.5$ g/cm^3, we can see that inside (10,10) nanotubes, Fig. 4(a), water diffuses faster inside hydrophobic pores than in hydrophilic pores. As well, a Fick regime is observed. Analyzing the density in Fig. 3(a), we can see that water is more packed to the hydrophilic wall. Thereafter, the friction between water and nanopore is higher, slowing the diffusion. Increasing the nanopore radius, Fig. 4(b) and (c), a distinct diffusive regime is observed. The systems shows an anomalous, subdiffusive regime. In these cases, the axial MSD is not linear and reaches a plateau at about 3 ns.

To understand this plateau, we plot in Fig. 5 the axial density profile for hydrophilic (16,16) nanotubes with densities $\rho_{eff} = 0.55$ g/cm^3 (solid red line) and $\rho_{eff} = 0.92$ g/cm^3 (solid black line). Once the densities are different, we plot the normalized density,

$$\rho_{\text{norm}}(z) = \frac{\rho_{eff}(z)}{\int \rho(z)dz} \, .$$

As Fig. 5 shows, the water have distinct profiles for each density. For $\rho_{eff} = 0.92$ g/cm^3 the water molecules are uniformly distributed in the z-direction. However, for the lower density there is a region of higher concentration of the particles. This indicates that the bubble shown in Fig. 2 remain more time in a specific region of the nanotube. Therefore, after a initial diffusion, that we can see in the MSD Fig. 4(b), the bubble stops her movement in the z-direction, leading to the plateau in

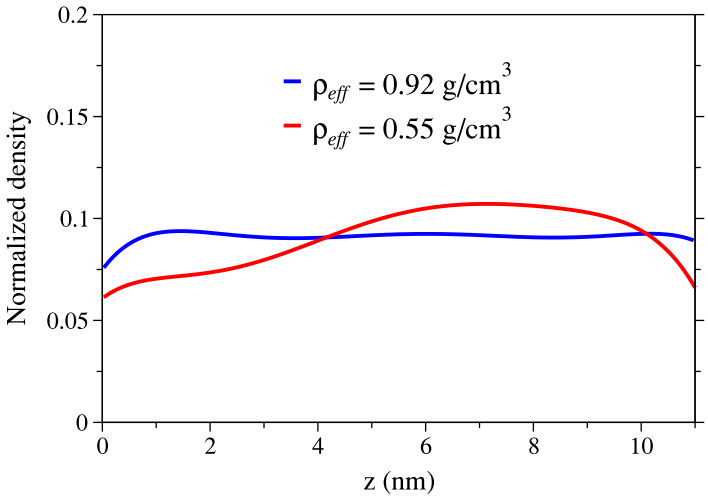

Fig. 5. Normalized axial density distribution of oxygen atoms inside hydrophilic (16,16) nanotubes with densities $\rho_{eff} \sim 0.5$ g/cm^3 (solid red line) and $\rho_{eff} \sim 0.9$ g/cm^3 (solid black line).

the MSD. To ensure that this plateau was not a equilibration problem, we run simulations up to 30 ns, and essentially the same MSD was obtained.

At the intermediate density $\rho_{eff} \sim 0.9$ g/cm^3 a Fick diffusive regime was obtained for all nanotube radii, as we show in Fig. 4(d), (e) and (f). Inside (10,10) and (16,16) nanotubes the diffusion is higher for hydrophobic confinement. Again, this is result of the higher friction with the hydrophilic wall. However, for (30,30) nanotubes there is no noticeable difference in the MSD for hydrophilic and hydrophobic nanopores. Basically, the bulk-like region, observed in Fig. 3(f), dominates the dynamical behavior, and the wall effects are less significant than for narrow nanotubes.

For the highest density, $\rho_{eff} \sim 1.3$ g/cm^3, and the narrower nanopores, the distinct water–wall interactions leads to completely different diffusive regimes. Inside hydrophobic (10,10) nanotubes the water diffuses in a Fick regime, as we shown in Fig. 4(g). This was observed in previous works for hydrophobic confinement [20,46]. Nevertheless, inside hydrophilic nanotube the system is in a solid-like state, with no diffusion. Finally, inside (16,16) and (30,30) nanotubes the diffusive behavior is the same. This was expected once the structural behavior was also the same.

Inside narrow (10,10) nanotube, either hydrophobic or hydrophilic, the number of first water neighbors is lower, and consequently the number of hydrogen bonds [47]. This leads to suppressing the strength of water–water attraction over the water–carbon interactions. In such case, the polarity of the nanotube wall plays an important role on the water mobility, rather than in larger (16,16) and (30,30) nanotubes.

4. Conclusions

We have analyzed the structural and dynamical behavior of water inside hydrophobic and hydrophilic nanotubes with distinct radii. Our results shows that both structure and diffusion are affected by the wall–water interaction. However, this influence is different accordingly with the water density inside the nanopore. As well, we have showed the strong relation between confined water structure and dynamics. The water packing at the nanopore wall affects the MSD inside the narrowest nanopores, specially for the lower densities. For wider (30,30) nanopores, our results shows that the water–wall interaction is less relevant once the fluid structure is bulk-like.

These findings shades some light on nanofluidics, and are helpful to understand the distinct behavior of water near polar or apolar sites in biological transmembrane channels, biomolecules hydration dynamics and chemically functionalized carbon, boron-nitrate or carbon doped boron-nitride nanotubes.

Acknowledgments

The authors acknowledge Brazilian science agencies CAPES and CNPq for financial support.

References

[1] S. Iijima, Helical microtubules of graphitic carbon, Nature 354 (1991) 56–58.
[2] B. Lee, Y. Baek, M. Lee, D.H. Jeong, H.H. Lee, J. Yoon, Y.H. Kim, A carbon nanotube wall membrane for water treatment, Nature Comm. 6 (2015) 7109.
[3] J. Geng, K. Kim, J. Zhang, A. Escalada, R. Tunuguntla, L.R. Comolli, F.I. Allen, A.V. Shnyrova, K. Cho, D. Munoz, Y.M. Wang, C.P. Grigoropoulos, C.M. Ajo-Franklin, V.A. Frolov, A. Noy, Stochastic transport through carbon nanotubes in lipid bilayers and live cell membranes, Nature 514 (2014) 612–615.
[4] M. Thomas, B. Corry, T.A. Hilder, Small 10 (2014) 1453–1465.
[5] H.G. Park, Y. Jung, Carbon nanofluidics of rapid water transport for energy applications, Chem. Soc. Rev. 43 (2014) 565–576.

[6] J. Shin, G. Kim, I. Kim, H. Jeon, T. An, G. Lim, Ionic liquid flow along the carbon nanotube with dc electric field, Sci. Rep. 5 (2015) 11799.
[7] A. Siddiqa, A. Shahid, R. Gill, Silica decorated CNTs sponge for selective removal of toxic contaminants and oil spills from water, J. Env. Chem. Eng. 3 (2) (2015) 892–897.
[8] C.-J. Shih, S. Lin, M.S. Strano, D. Blankschtein, Understanding the stabilization of single-walled carbon nanotubes and graphene in ionic surfactant aqueous solutions: large-scale coarse-grained molecular dynamics simulation-assisted DLVO theory, J. Phys. Chem. C 119 (2) (2015) 1047–1060.
[9] N. Naguib, H. Ye, Y. Gogotsi, A.G. Yazicioglu, C.M. Megaridis, M. Yoshimura, Observation of water confined in nanometer channels of closed carbon nanotubes, Nano Lett. 4 (11) (2004) 2237–2243.
[10] J.K. Holt, H.G. Park, Y.M. Wang, M. Stadermann, A.B. Artyukhin, C.P. Grigoropulos, A. Noy, O. Bakajin, Fast mass transport through sub-2-nanometer carbon nanotubes, Science 312 (2006) 1034–1037.
[11] M. Majunder, N. Chopra, R. Andrews, B.J. Hinds, Nanoscale hydrodynamics: enhanced flow in carbon nanotubes, Nature 438 (2005) 44.
[12] G. Hummer, J.C. Rasaiah, J.P. Noworytra, Water conduction through the hydrophobic channel of a carbon nanotube, Nature 404 (2001) 188.
[13] P. Kumar, S.V. Buldyrev, Starr Francis F.W., N. Giovambattista, H.E. Stanley, Thermodynamics, structure, and dynamics of water confined between hydrophobic plates, Phys. Rev. E 72 (2005) 051503.
[14] J.R. Bordin, J.S. Soares, A. Diehl, M.C. Barbosa, Enhanced flow of core-softened fluids through narrow nanotubes, J. Chem. Phys. 140 (2014) 194504.
[15] M.H. Köhler, J.R. Bordin, L.B. da Silva, M.C. Barbosa, Breakdown of the Stokes–Einstein water transport through narrow hydrophobic nanotubes, Phys. Chem. Chem. Phys. 19 (2017) 12921–12927.
[16] J. Jin, L. Fu, H. Yang, J. Ouyang, Carbon hybridized halloysite nanotubes for high-performance hydrogen storage capacities, Scientific Reports 5 (2015) 12429.
[17] M.H. Köhler, R.C. Barbosa, L.B. da Silva, M.C. Barbosa, Role of the hydrophobic and hydrophilic sites in the dynamic crossover of the protein-hydration water, Phys. A 468 (2017) 733–739.
[18] Y. Xu, X. Tian, M. Lv, M. Deng, B. He, P. Xiu, Y. Tu, Y. Zheng, Effects of water-channel attractions on single-file water permeation through nanochannels, J. Phys. D: Appl. Phys. 49 (28) (2016) 285302.
[19] F. Ramazani, F. Ebrahimi, Uncertainties in the capillary filling of heterogeneous water nanochannels, J. Phys. Chem. C 120 (23) (2016) 12871–12878.
[20] J.R. Bordin, A.B. de Oliveira, A. Diehl, M.C. Barbosa, Diffusion enhancement in core-softened fluid confined in nanotubes, J. Chem. Phys 137 (2012) 084504.
[21] J.R. Bordin, M.C. Barbosa, Flow and structure of fluids in functionalized nanopores, Phys. A 467 (2017) 137–147.
[22] I. Moskowitz, M.A. Snyder, J. Mittal, Water transport through functionalized nanotubes with tunable hydrophobicity, J. Chem. Phys. 141 (2014) 18C532.
[23] S. Plimpton, Fast parallel algorithms for short-range molecular dynamics, J. Comput. Phys. 117 (1995) 1–19.
[24] J.L.F. Abascal, C. Vega, A general purpose model for the condensed phases of water: TIP4P/2005, J. Chem. Phys. 123 (2005) 234505.
[25] G. Raabe, R.J. Sadus, Molecular dynamics simulation of the effect of bond flexibility on the transport properties of water, J. Chem. Phys. 137 (2012) 104512.
[26] L. Liu, G.N. Patey, Simulated conduction rates of water through a (6,6) carbon nanotube strongly depend on bulk properties of the model employed, J. Chem. Phys. 144 (2016) 184502.
[27] K. Krynicki, C.D. Green, D.W. Sawyer, Pressure and temperature dependence of self-diffusion in water, Faraday Discuss. Chem. Soc. 66 (1978) 199–208.
[28] R.W. Hockney, J.W. Eastwood, Computer Simulation using Particles, McGraw-Hill, 1981.
[29] S. Nosé, A molecular dynamics method for simulation in the canonical ensemble, Mol. Phys. 52 (1984) 255.
[30] W.G. Hoover, Canonical dynamics: equilibrium phase-space distributions, Phys. Rev. A 31 (1985) 1695.
[31] J.P. Ryckaert, G. Ciccotti, H.J.C. Berendsen, Numerical integration of the cartesian equations of motion of a system with constraints: molecular dynamics of n-alkanes, J. Comput. Phys. 23 (1977) 327–341.
[32] P. Allen, D.J. Tildesley, Computer Simulation of Liquids, Oxford University Press, 1987.
[33] Y. Zheng, H. Ye, Z. Zhang, H. Zhang, Water diffusion inside carbon nanotubes: mutual effects of surface and confinement, Phys. Chem. Chem. Phys. 14 (2012) 964–971.
[34] M.H. Köhler, L.B. da Silva, Size effects and the role of density on the viscosity of water confined in carbon nanotubes, Chem. Phys. Lett. 645 (2016) 38–41.
[35] J.C. Rasaiah, S. Garde, G. Hummer, Water in nonpolar confinement: from nanotubes to proteins and beyond, Annu. Rev. Phys. Chem. 59 (2008) 713–740.
[36] S. Capponi, M. Heyden, A.-N. Bondar, D.J. Tobias, S.H. White, Anomalous behavior of water inside the secy translocon, Proc. Natl. Acad. Sci. USA 29 (2015) 9016–9021.
[37] K. Ritos, M.K. Borg, N.J. Mottram, J.M. Reese, Electric fields can control the transport of water in carbon nanotubes, Phil. Trans. R. Soc. A 374 (2016) 20150025.
[38] Winarto, D. Takaiwa, E. Yamamoto, K. Yasuoka, Structures of water molecules in carbon nanotubes under electric fields, J. Chem. Phys. 142 (2015) 124701.
[39] K. Koga, G.T. Gao, H. Tanaka, X.C. Zeng, Formation of ordered ice nanotubes inside carbon nanotubes, Nature 412 (2001) 802–805.
[40] Z.E. Hughes, C.J. Shearer, J. Shapter, J.D. Gale, Simulation of water transport through functionalized single-walled carbon nanotubes (swcnts), J. Phys. Chem. C 116 (2012) 24943–24953.
[41] G. Cicero, J.C. Grossman, E. Schwegler, F. Gygi, G. Galli, Water confined in nanotubes and between graphene sheets:a first principle study, J. Am. Chem. Soc. 130 (2008) 1871–1878.
[42] J.R. Bordin, A. Diehl, M.C. Barbosa, Relation between flow enhancement factor and structure for core-softened fluids inside nanotubes, J. Phys. Chem. B 117 (2013) 7047–7056.
[43] K. Zhao, H. Wu, Structure-dependent water transport across nanopores of carbon nanotubes: toward selective gating upon temperature regulation, Phys. Chem. Chem. Phys. 17 (2015) 10343–10347.
[44] Yu.D. Fomin, V.N. Ryzhov, E.N. Tsiok, The behaviour of water and sodium chloride solution confined into asbestos nanotube, Mol. Phys. 114 (15) (2016) 2279–2288.
[45] M. De Marzio, G. Camisasca, M.M. Conde, M. Rovere, P. Gallo, Structural properties and fragile to strong transition in confined water, J. Chem. Phys. 146 (8) (2017) 084505.
[46] R.J. Mash, S. Joseph, N.R. Aluru, Anomalously immobilized water: a new water phase induced by confinement in nanotubes, Nano Lett. 3 (2003) 589.
[47] A. Alexiadis, S. Kassinos, Molecular simulation of water in carbon nanotubes, Chem. Rev. 108 (2008) 5014.

Appendix C

THE JOURNAL OF PHYSICAL CHEMISTRY C

Article

Cite This: J. Phys. Chem. C 2018, 122, 6684−6690

pubs.acs.org/JPCC

Surface, Density, and Temperature Effects on the Water Diffusion and Structure Inside Narrow Nanotubes

Mateus Henrique Köhler*,† and José Rafael Bordin*,‡

†Instituto de Física, Universidade Federal do Rio Grande do Sul, 91501-970 Porto Alegre, Brazil

‡Campus Caçapava do Sul, Universidade Federal do Pampa, 96570-000 Caçapava do Sul, Brazil

ABSTRACT: The nanoconfinement of water leads to outstanding anomalous behaviors. The interfacial interactions between water and surface is an important effect in the majority of these events. In this study, we have used the molecular dynamics simulations to investigate the diffusion characteristics of water molecules confined in narrow nanotubes with variable polarity. The nanotubes were built with hydrophilic or hydrophobic sites. Our results shows that there is a strong relation between density and surface properties for the water structuration inside the nanotubes. At low densities and narrower nanotubes, the surface characteristics play a major role, whereas for wider nanotubes, we observe distinct structuration at higher densities. The density is found to profoundly affect the water mobility in both nanotube species. This effect is accompanied by an organization in layers, resulting in structural transitions of water inside the nanotube as we increase the density. The temperature plays an important role in the transport of water inside small nanotubes. Our findings show that a small change in the nanotube diameter can lead to distinct dependence of diffusion with the temperature. The results indicate how density, temperature, and surface properties affect the dynamical and structural behavior of water inside narrow nanopores.

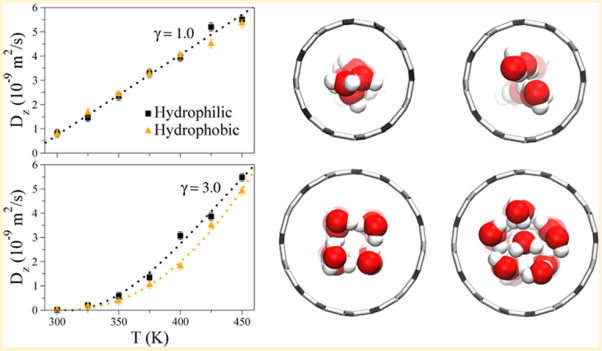

INTRODUCTION

Water, this extraordinary liquid, holds great fascination among scientists and curious people in general intrigued with its anomalies.[1,2] Although we usually think in bulk water, it is eventually found confined in nature. For instance, the mass transportation among our cells is directly mediated by water flow in nanostructured channels (e.g., aquaporins[3]). A fascinating event takes place also when water enters the hollow cavity of a carbon nanotube (CNT), presenting what we call the superflux, exceeding the flow predicted by the continuum hydrodynamic theory by more then 3 orders of magnitude.[4] This phenomenon has been widely investigated in the last decade. However, some questions still pose as open subjects. The atomically smooth surface and ordered molecular structure make the CNT an energy-efficient escape for the water molecules. The water's journey through a nanotube is full of anomalous structural and dynamical behaviors, making these systems interesting models for biomolecular mass transportation studies and for potential new technologies.

In recent years, a number of computational and experimental studies have been conducted to understand the water flow through hydrophobic,[5] modified,[6] and charged[7] narrow channels. The possibility of tuning the water−CNT interaction, by making it more hydrophilic or hydrophobic, is important either to achieve higher water permeation or to induce it to experience structural and dynamical transitions. The impact of hydrophobicity over water properties has aroused long debate. Chemically functionalized nanotubes[8−10] and biological molecules[11,12] can show hydrophobic and hydrophilic sites. This adds even more complexity to this picture and presents an opportunity to study the effect of polarity heterogeneity over confined water properties.

As we increase the degree of confinement by decreasing the nanotube radius, the hydrophobic effect over the water properties is expected to be more pronounced because the nanotube−water interactions becomes more frequent than the water−water interaction. In fact, Hummer and colleagues[13] have demonstrated that a small change in the water−carbon interaction strength can profoundly impact the water occupancy inside small CNTs. Moskowitz et al.[14] have found that the water flux through nanotubes is sensitive to the fraction of hydrophobic/hydrophilic atoms, regardless of their arrangement. It is intriguing, however, that when located in the tube entrance, the hydrophobic atoms can play some role, lowering the filling rate.[15] Additionally, Xu and his group[16] found a maximal flow when empty states are present in the inner of the nanotube, which is unexpected because in this situation the wired hydrogen-bonding network (prerequisite for high water

Received: January 4, 2018
Revised: February 8, 2018
Published: March 8, 2018

DOI: 10.1021/acs.jpcc.8b00112
J. Phys. Chem. C 2018, 122, 6684−6690

permeability) is broken. All these results point out that there are still important parameters to be taken into account in the general physical−chemical understanding of the properties of confined water, especially regarding the nanopore polarity.

Another affecting parameter is the temperature. The distinct behavior of confined and bulk water leads to distinct freezing temperatures and regions of liquid−ice coexistence.[17,18] For instance, experimental and computational studies indicates that water can freeze inside CNTs at high temperatures, where bulk water is in boiling conditions.[19,20]

In this way, in this paper, we employ molecular dynamics to analyze the impact of hydrophobic or hydrophilic surface and distinct temperatures over the structure and dynamics of the water confined inside small nanotubes. The diffusion behavior and the molecular distribution of the confined water were analyzed for nanotubes with diameters ranging from 0.8 to 1.1 nm. The paper is organized as follows. In the next section, Computational Details and Methods are described. In Results and Discussion, the main results of the dynamic and structural properties of the confined water are discussed. Summary and Conclusions are presented in last section.

COMPUTATIONAL DETAILS AND METHODS

Water and Nanotube Models. Molecular dynamics were performed using the LAMMPS package[21] for simulations of TIP4P/2005 water[22] confined inside nanotubes. The choice of TIP4P/2005 over many other models available in the literature was due to its accuracy in calculating the transport properties of water at ambient conditions.[22,23] Particularly for the bulk diffusion coefficient, we have found 2.32×10^{-9} m^2/s, which is in close agreement to previous theoretical[24] and experimental works.[25] The nanotube atoms are arranged on a honeycomb lattice. Two different atom types were used to build the nanotube. They differ only by their Lennard-Jones (LJ) parameters of interaction with water and correspond to sp^2-hybridized carbon with ε_{CO} = 0.478 kJ/mol and σ_{CO} = 0.328 nm (labeled hydrophilic due to water attractive character) and reduced carbon−water interaction strength with ε_{CO} = 0.27 kJ/mol and σ_{CO} = 0.341 nm (namely hydrophobic), as done in previous works.[13,26,27] We considered three cases of (n,n) nanotubes, with n = 6, 7, and 8.

Periodic boundary conditions were applied to simulate isolated infinite nanotubes. The cutoff distances for LJ and Coulomb interactions are 1.0 and 1.2 nm, respectively. Long-range Coulomb interactions was handled using particle−particle particle−mesh method.[28] The simulations were conducted in the NVT ensemble at temperature 300 K fixed by a Nosé−Hoover thermostat.[29,30] Each nanotube was filled up to the desired density for each combination of ε and temperature. The system was then equilibrated with a 15 ns simulation, followed by 15 ns of data accumulation. The timestep is 1 fs. In all simulations, the geometry of water molecules was constrained by the SHAKE algorithm.[31] For each case, three independent simulations were performed.

Simulation Details. The diffusion mechanism of a fluid can be reflected by the scaling behavior between the mean squared displacement (MSD) and time[32]

$$\langle |\vec{r}(t) - \vec{r}(0)|^2 \rangle \propto Dt^{\alpha} \tag{1}$$

where $\langle |\vec{r}(t) - \vec{r}(0)|^2 \rangle$ is referred as the MSD, $\langle\rangle$ denotes an average over all the molecules, and $\vec{r}(t)$ is the displacement of a molecule during the time interval t. The α exponent refers to the diffusion regime: $\alpha = 1$ for linear Fickian diffusion, $\alpha > 1$ for superdiffusive and $\alpha < 1$ for subdiffusive regime. In the bulk phase, the water molecules diffuse as the Fickian type. However, with water confined in CNTs, the diffusion behavior becomes extraordinary due to the nanoscale confinement.[26] For a fluid, the statistical error could be reduced by averaging over all the MSD components. But the nanopore confinement in the x- and y-directions hinders the radial displacement of the molecules. Therefore, the radial MSD is almost 0 for all cases studied here and only the axial MSD will be considered.

We use the effective diameter $d_{eff} = d - \sigma_{CO}$,[33] where d is the nominal diameter and σ_{CO} is the Lennard-Jones (LJ) parameter for carbon−oxygen interaction, to calculate the water density inside the nanotube. In terms of d_{eff}, the effective density is then given by

$$\rho_{eff} = \frac{M}{\pi \cdot l \cdot \left(\frac{d_{eff}}{2}\right)^2} \tag{2}$$

where M is the total water mass into the pore and l is the nanotube length. In Figure 1, we present a depiction of the computational framework. In Table 1, the nanotube chirality, nominal diameter d, length l, number of enclosed water molecules N, and the considered effective densities ρ_{eff} are presented. The water radial density profile was evaluated by dividing the inner of the nanotube in concentric cylindrical shells and averaging the number of oxygen atoms in each shell along the simulation.

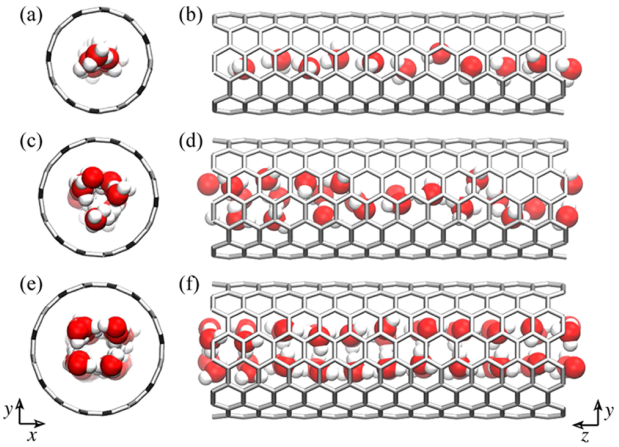

Figure 1. Frontal and lateral snapshot of (a) and (b) (6,6), (c) and (d) (7,7), and (e) and (f) (8,8) nanotube filled with water. Red spheres stands for oxygen atoms, white for hydrogen, and the carbon atoms are colored as silver dynamic bonds.

Table 1. Nominal Diameter d, Length l, Number of Enclosed Molecules N, and the Range of Effective Densities (ρ_{eff}) for the Nanotube Samples

chirality	d (nm)	l (nm)	N	ρ_{eff} (g/cm^3)
(6,6)	0.81	205	750−1100	0.6−0.9
(7,7)	0.95	102	750−1050	0.7−1.0
(8,8)	1.08	60	650−1120	0.7−1.2

DOI: 10.1021/acs.jpcc.8b00112
J. Phys. Chem. C 2018, 122, 6684−6690

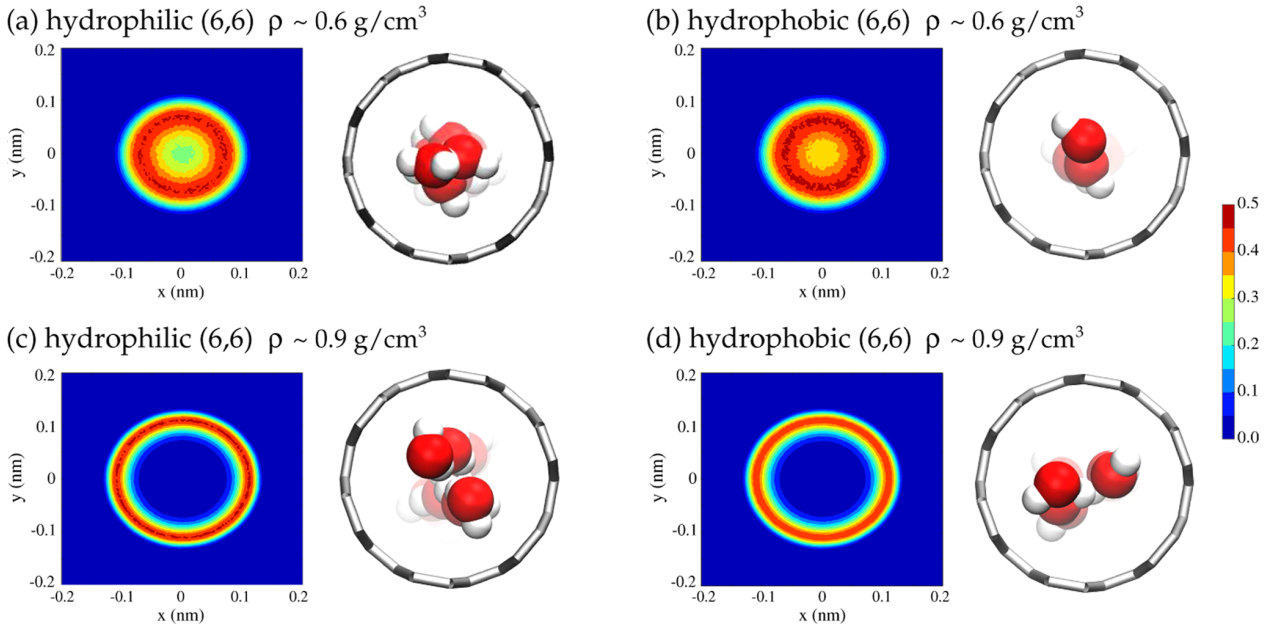

Figure 2. Two-dimensional color density maps of oxygen atoms inside (6,6) nanotubes and frontal snapshot of the final configuration for (a, b) 0.6 g/cm^3 and (c, d) 0.9 g/cm^3.

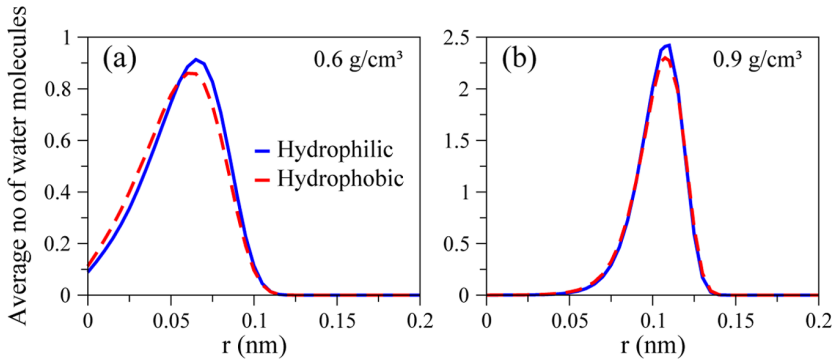

Figure 3. Radial density profile of oxygen atoms inside (6,6) nanotubes for densities (a) 0.6 g/cm^3 and (b) 0.9 g/cm^3.

RESULTS AND DISCUSSION

Surface Chemistry and Density Effect. Water structure and dynamics under hydrophobic and hydrophilic confinement is relevant to understand and develop new technologies, as well to understand aspects of life and basic science. For instance, nonpolar or weakly polar pores play a prominent role in aquaporin water channels.[34] In such systems, water occupies their weakly polar pores at least transiently, exhibiting anomalous diffusion and dipoles aligned with the transmembrane axis. The pore polarity is therefore an important parameter in the confined water properties. To understand the behavior of water confined in hydrophobic and hydrophilic nanotubes at different densities, we first discuss the water molecules arrangement inside these structures.

In Figure 2, we show the radial structuration of water molecules inside (6,6) nanotubes. At this small nanotube radius, the confinement induces a straight single-file of molecules and any physical parameter should affect the structure assumed by the water.[35] For the lower density, Figure 2a, the water molecules tend to settle at the center of the tube. In this case, we can observe that the hydrophobic confinement increases the accumulation of water molecules at the center compared with the hydrophilic case, Figure 2b. This difference is clear also in the density profile, Figure 3a. As the number of water molecules in the inner hole of the (6,6) nanotube increases, the arrangement changes to a zigzag single layer, with the molecules closer to the wall, as indicated by Figure 2c,d. At these higher densities, the nanotube polarity plays a small role, with both cases showing similar radial density maps.

Figures 2 and 3 show that higher densities weakens the surface effect for (6,6) nanotubes, leading to similar radial distribution arrangement for both hydrophobic and hydrophilic confinements.

The increase in the nanotube radius leads to distinct structures. In Figure 4, we show the radial structuration of water molecules inside a (8,8) nanotube. Here, for lower densities, we find that the water molecules form a square structure, as shown in Figure 4a. This layered arrangement is not affected by the pore polarity: the radial density map in Figure 4b for hydrophobic nanopores is essentially the same as that for the hydrophobic case, as the snapshot indicates. Also, the density profile, Figure 5a, reinforces this finding. At higher

DOI: 10.1021/acs.jpcc.8b00112
J. Phys. Chem. C 2018, 122, 6684−6690

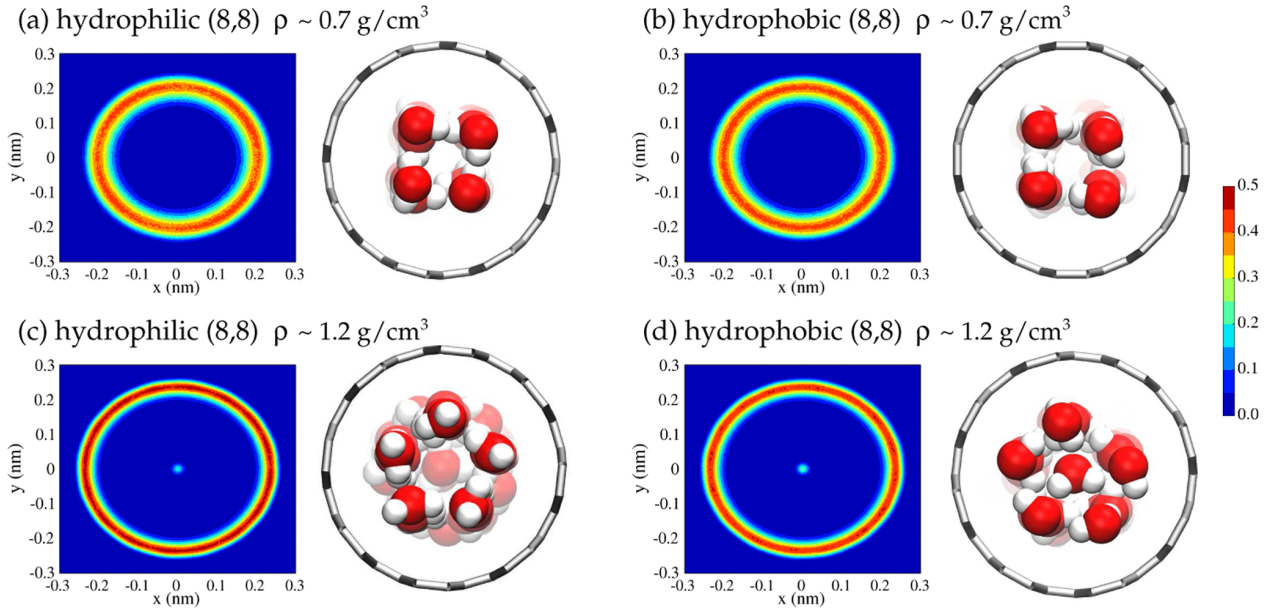

Figure 4. Two-dimensional color density maps of oxygen atoms inside (8,8) nanotubes and frontal snapshot of the final configuration for (a, b) 0.7 g/cm^3 and (c, d) 1.2 g/cm^3.

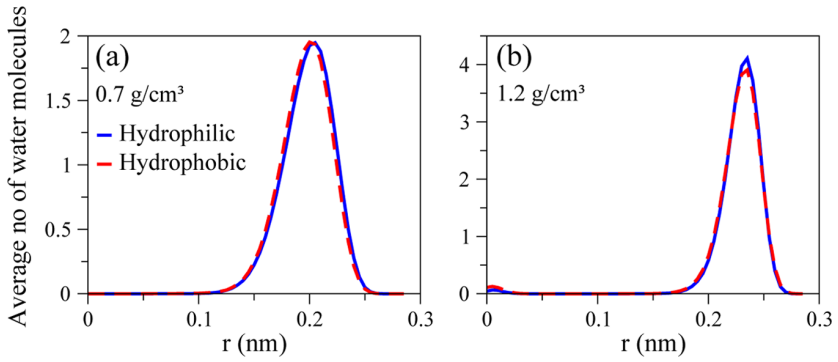

Figure 5. Radial density profile of oxygen atoms inside (8,8) nanotubes for densities (a) 0.7 g/cm^3 and (b) 1.2 g/cm^3.

density, the water structure changes to a external pentagonal layer with a central single-file layer, as the Figure 4c,d show. Despite the apparent similarity in the snapshot and in the color map, for a higher density, there are small differences in the structure regarding the nanotube surface properties: the hydrophobic nanotube shows a slightly less water packing at the nanotube interface but allows a denser arrangement of molecules at the center. This is clear in the density profile of Figure 5b, where the peak near the center of the nanotube is higher for hydrophobic nanotubes, whereas the one near the wall is higher for hydrophilic nanotubes.

Fluids structure and diffusion inside nanopores are strongly related.[36−38] Therefore, distinct structural regimes can lead to different diffusive behaviors. In Figure 6, we present the MSD as a function of simulation time for the confined water. We can notice that the nanotube radii induces differences to the water's diffusive behavior: whereas inside (7,7) and (8,8) nanotubes water undergoes Fickian diffusion (MSD $\propto t$), in the smaller (6,6) nanotube, the water molecules present a transition from a initial ballistic diffusion (inset of Figure 6a) to a plateau, where a stationary state can be implied. The water at low density inside (7,7) and (8,8) nanotubes has distinct MSD slopes regarding the nanotube surface properties, as shown in Figure 6b,c. The hydrophilic nanotubes have a higher mobility for the lower densities. Increasing the density of both species of nanotubes leads to the same slope in the MSD curve. We can associate this with the change in the conformation. For the lower density, the water has a tubular square structure, and the diffusion is affected only by the water−wall friction. On the other hand, at higher densities, we observed a tubular layer with a central single-file layer. Therefore, here we have the water−water friction as a new feature, which leads to both hydrophilic and hydrophobic nanotubes to have the same diffusive behavior.[9,26]

Role of Temperature. The diffusion coefficient of water is known to be sensitive to temperature variations.[39,40] In confined fluids, we can observe heterogeneous dynamics, which lead to anomalous diffusional behaviors.[41,42] Nanotubes usually induce the confined water to present multiphase transitions at different temperatures.[43,44] These structures are eventually connected with water mobility inside the pore, which generates a wide range of possibilities for controlling the fluid flow.

DOI: 10.1021/acs.jpcc.8b00112
J. Phys. Chem. C 2018, 122, 6684−6690

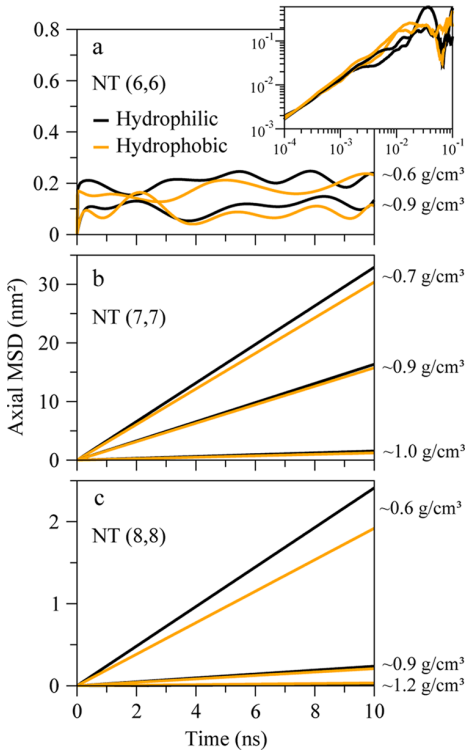

Figure 6. MSD versus time for (a) (6,6), (b) (7,7), and (c) (8,8) hydrophobic and hydrophilic nanotubes.

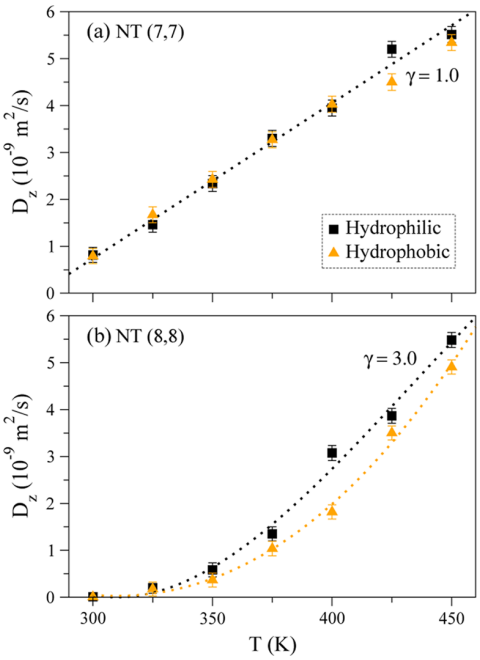

Figure 7. Axial diffusion coefficient D_z as a function of temperature T for a system with density 0.9 g/cm^3. The error bars stand for standard deviation from three independent simulations. The dotted lines are guide to the eyes based in polynomial fits, $D_z = O(T^\gamma)$. For the (7,7) nanotube, both curves can be fitted by the same line.

To clarify the effect of temperature over the dynamics of water confined in hydrophobic and hydrophilic nanotubes, we show in Figure 7 the diffusion of water molecules as a function of temperature. Because the water inside the (6,6) nanotube shows no mobility at 300 K, here we focused in the wider nanopores. As well, in these simulations, we have considered the case of density 0.9 g/cm^3 because the MSD for hydrophilic and hydrophobic nanotubes have the same slope for (7,7) and (8,8) nanotubes, Figure 6b,c. At this density, the water has a tubular structure, without the central layer, which implies the water−wall interaction to be prominent. Therefore, we can relate changes in dynamics with the temperature and surface effects.

For temperatures lower than 300 K, the diffusion coefficient is practically 0 at 275 K for (8,8) nanotubes and at 250 K inside (7,7) nanotubes. Because our goal is to study the diffusive properties, we show in Figure 7 the dependence of D_z on temperature, which ranges from 300 to 450 K. Despite the small difference in the diameter, 0.13 nm, a clear difference is noticeable in the diffusion inside each nanotube. For (7,7) nanotubes, the water have a higher mobility at 300 K than inside (8,8) nanotubes. This higher diffusion in narrower nanotubes near room temperatures was already reported in the literature.[45,46]

Above 300 K, the diffusion constant D_z shows a linear increase inside (7,7) nanotubes, i.e., $D_z \sim T$. On the other hand, D_z grows with $O(T^3)$ for (8,8) nanotubes. Also, whereas for (7,7) nanotubes, D_z is approximately the same for hydrophobic and hydrophilic nanotubes up to 400 K, and slightly smaller above this threshold, for (8,8) nanotubes, all values obtained for D_z are higher inside the hydrophobic channels. Due to the distinct dependence with temperature, at T = 450 K, the diffusion constant is approximately the same for (7,7) and (8,8) hydrophobic nanotubes. However, for the hydrophilic nanotubes, the diffusion inside the wider nanotube is small even at 450 K.

As expected, the distinct dynamical features are correlated to distinct structural conformations. In Figure 8a, we show the oxygen's radial density profile at different temperatures for (7,7) nanotubes. As the curves indicates, both hydrophilic and hydrophobic surfaces have almost the same structure, with the same radial position for the peaks for a given temperature. This shows why both surfaces lead to the same dependence of the diffusion coefficient. Remarkably, for 400 and 450 K, there is a slight difference in the peak's magnitude between the hydrophobic and hydrophilic pores, which implies a slightly more organized water layer inside the latter nanotube. This explains why the axial diffusion above 400 K is smaller inside the hydrophobic (7,7) nanotubes: the more organized the water molecules are, less collisions occur between the water molecules, and the axial displacement is facilitated through the tube. On the other hand, for (8,8) nanotubes, Figure 8b, the unpacking of the water molecules close to the interface is more clear. By increasing T, the peak decreases and the distribution spreads toward the nanotube surface. Also, in all cases, the packing is more pronounced for hydrophilic surfaces, which means the water molecules are more structured. Therefore, the friction is lower and the diffusion is higher, as we have observed in Figure 7b. This shows how the structural and dynamical properties of water inside nanotubes with distinct surfaces depends on the pore diameter.

SUMMARY AND CONCLUSIONS

In this work, we have investigated through molecular dynamics simulations, the effect of hydrophobicity over the structure and

DOI: 10.1021/acs.jpcc.8b00112
J. Phys. Chem. C 2018, 122, 6684−6690

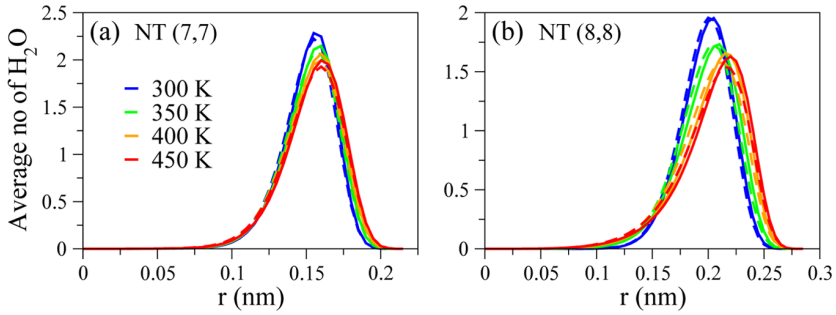

Figure 8. Oxygen's radial density profile inside (a) (7,7) and (b) (8,8) nanotubes at distinct temperatures. Solid lines stands for hydrophilic surfaces, whereas dashed lines for hydrophobic nanotubes.

dynamics of water confined in small nanotubes. The results point that the influence of the water−wall interaction over its properties is dependent on temperature, density, and nanotube diameter. The structural and dynamical properties reported in the previous section all consistently show that the increase in density leads to a higher structuration for all the samples. The organization in layers is certainly preferred by the water molecules to decrease the bond enthalpy at the high-density regime, but at the cost of mobility.

The temperature has been shown as a critical parameter for water mobility inside the nanotubes. Particularly, for higher temperatures, we have found different diffusion of water confined in hydrophilic (8,8) nanotubes compared with hydrophobic pores. Also, the dependence on the temperature is distinct for (7,7) and (8,8) nanotubes. This variation is also accompanied by changes in the water organization inside each nanotube. These findings shed some light on heterogeneous nanofluidics and are helpful in understanding the distinct behavior of water near polar and apolar sites in functionalized synthetic nanopores and biological transmembrane channels.

AUTHOR INFORMATION

Corresponding Authors

*E-mail: mateus.kohler@ufrgs.br (M.H.K.).
*E-mail: josebordin@unipampa.edu.br (J.R.B.).

ORCID

Mateus Henrique Köhler: 0000-0001-9733-9630
José Rafael Bordin: 0000-0002-8025-6529

Notes

The authors declare no competing financial interest.

ACKNOWLEDGMENTS

The authors acknowledge Brazilian science agencies FAPERGS, CNPq, and INCT-Fcx for financial support, CENAPAD-SP and CESUP-UFRGS for the computer time.

REFERENCES

(1) Barbosa, M. C. Tapping the incredible weirdness of water. *New Sci.* **2015**, *226*, 26−27.
(2) Gallo, P.; Amann-Winkel, K.; Angell, C. A.; Anisimov, M. A.; Caupin, F.; Chakravarty, C.; Lascaris, E.; Loerting, T.; Panagiotopoulos, A. Z.; Russo, J.; Sellberg, J. A.; Stanley, H. E.; Tanaka, H.; Vega, C.; Xu, L.; Pettersson, L. G. M. Water: A tale of two liquids. *Chem. Rev.* **2016**, *116*, 7463−7500.
(3) Farimani, A. B.; Aluru, N. R.; Tajkhorshid, E. Thermodynamic insight into spontaneous hydration and rapid water permeation in aquaporins. *Appl. Phys. Lett.* **2014**, *105*, No. 083702.
(4) Majumder, M.; Chopra, N.; Andrews, R.; Hinds, B. J. Nanoscale hydrodynamics: Enhanced flow in carbon nanotubes. *Nature* **2005**, *438*, 44.
(5) Secchi, E.; Marbach, S.; Nigues, A.; Stein, D.; Siria, A.; Bocquet, L. Massive radius-dependent flow slippage in carbon nanotubes. *Nature* **2016**, *537*, 210−213.
(6) Giovambattista, N.; Almeida, A. B.; Alencar, A. M.; Buldyrev, S. V. Validation of capillarity theory at the nanometer scale by atomistic computer simulations of water droplets and bridges in contact with hydrophobic and hydrophilic surfaces. *J. Phys. Chem. C* **2016**, *120*, 1597−1608.
(7) Khodabakhshi, M.; Moosavi, A. Unidirectional transport of water through an asymmetrically charged rotating carbon nanotube. *J. Phys. Chem. C* **2017**, *121*, 23649−23658.
(8) Thomas, M.; Corry, B.; Hilder, T. A. What have we learnt about the mechanisms of rapid water transport,ion rejection and selectivity in nanopores from molecular simulation? *Small* **2014**, *10*, 1453−1465.
(9) Bordin, J. R.; Barbosa, M. C. Flow and structure of fluids in functionalized nanopores. *Phys. A* **2017**, *467*, 137−147.
(10) Setaro, A. Advanced carbon nanotubes functionalization. *J. Phys.: Condens. Matter* **2017**, *29*, No. 423003.
(11) Köhler, M. H.; Barbosa, R. C.; da Silva, L. B.; Barbosa, M. C. Role of the hydrophobic and hydrophilic sites in the dynamic crossover of the protein-hydration water. *Phys. A* **2017**, *468*, 733−739.
(12) Martelli, F.; Ko, H.-Y.; Borallo, C. C.; Franzese, G. Structural properties of water confined by phospholipid membranes. *Front. Phys.* **2018**, *13*, No. 136801.
(13) Hummer, G.; Rasaiah, J. C.; Noworytra, J. P. Water conduction through the hydrophobic channel of a carbon nanotube. *Nature* **2001**, *414*, 188.
(14) Moskowitz, I.; Snyder, M. A.; Mittal, J. Water transport through functionalized nanotubes with tunable hydrophobicity. *J. Chem. Phys.* **2014**, *141*, No. 18C532.
(15) Ramazani, F.; Ebrahimi, F. Uncertainties in the capillary filling of heterogeneous water nanochannels. *J. Phys. Chem. C* **2016**, *120*, 12871−12878.
(16) Xu, Y.; Tian, X.; Lv, M.; Deng, M.; He, B.; Xiu, P.; Tu, Y.; Zheng, Y. Effects of water-channel attractions on single-file water permeation through nanochannels. *J. Phys. D: Appl. Phys.* **2016**, *49*, No. 285302.
(17) Moore, E. B.; Alle, J. T.; Molinero, V. Liquid-ice coexistence below the melting temperature for water confined in hydrophilic and hydrophobic nanopores. *J. Phys. Chem. C* **2012**, *116*, 7507−7514.
(18) Giovambattista, N.; Rossky, P.; Debenedetti, P. Computational studies of pressure, temperature, and surface effects on the structure and thermodynamics of confined water. *Annu. Rev. Phys. Chem.* **2012**, *63*, 179−200.
(19) Agrawal, K. V.; Shimizu, S.; Drahushuk, L. W.; Kilcoyne, D.; Strano, M. S. Observation of extreme phase transition temperatures of water confined inside isolated carbon nanotubes. *Nat. Nanotechnol.* **2017**, *12*, 267−273.
(20) Pugliese, P.; Conde, M. M.; Rovere, M.; Gallo, P. Freezing temperatures, ice nanotubes structures, and proton ordering of

DOI: 10.1021/acs.jpcc.8b00112
J. Phys. Chem. C 2018, 122, 6684−6690

TIP4P/ICE water inside single wall carbon nanotubes. *J. Phys. Chem. B* **2017**, *121*, 10371−10381.
(21) Plimpton, S. Fast parallel algorithms for short-range molecular dynamics. *J. Comput. Phys.* **1995**, *117*, 1−19.
(22) Abascal, J. L. F.; Vega, C. A general purpose model for the condensed phases of water: TIP4P/2005. *J. Chem. Phys.* **2005**, *123*, No. 234505.
(23) Raabe, G.; Sadus, R. J. Molecular dynamics simulation of the effect of bond flexibility on the transport properties of water. *J. Chem. Phys.* **2012**, *137*, No. 104512.
(24) Liu, L.; Patey, G. N. Simulated conduction rates of water through a (6,6) carbon nanotube strongly depend on bulk properties of the model employed. *J. Chem. Phys.* **2016**, *144*, No. 184502.
(25) Krynicki, K.; Green, C. D.; Sawyer, D. W. Pressure and temperature dependence of self-diffusion in water. *Faraday Discuss. Chem. Soc.* **1978**, *66*, 199−208.
(26) Köhler, M. H.; Bordin, J. R.; da Silva, L. B.; Barbosa, M. C. Breakdown of the Stokes-Einstein water transport through narrow hydrophobic nanotubes. *Phys. Chem. Chem. Phys.* **2017**, *19*, 12921−12927.
(27) Köhler, M. H.; Bordin, J. R.; da Silva, L. B.; Barbosa, M. C. Structure and dynamics of water inside hydrophobic and hydrophilic nanotubes. *Phys. A* **2018**, *490*, 331−337.
(28) Hockney, R. W.; Eastwood, J. W. *Computer Simulation Using Particles*; McGraw-Hill: New York, 1981.
(29) Nosé, S. A molecular dynamics method for simulation in the canonical ensemble. *Mol. Phys.* **1984**, *52*, 255.
(30) Hoover, W. G. Canonical dynamics: Equilibrium phase-space distributions. *Phys. Rev. A* **1985**, *31*, 1695.
(31) Ryckaert, J. P.; Ciccotti, G.; Berendsen, H. J. C. Numerical integration of the cartesian equations of motion of a system with constraints: molecular dynamics of n-alkanes. *J. Comput. Phys.* **1977**, *23*, 327−341.
(32) Allen, P.; Tildesley, D. J. *Computer Simulation of Liquids*; Oxford University Press: Oxford, 1987.
(33) Köhler, M. H.; da Silva, L. B. Size effects and the role of density on the viscosity of water confined in carbon nanotubes. *Chem. Phys. Lett.* **2016**, *645*, 38−41.
(34) Capponi, S.; Heyden, M.; Bondar, A.-N.; Tobias, D. J.; White, S. H. Anomalous behavior of water inside the SecY translocon. *Proc. Natl. Acad. Sci. U.S.A.* **2015**, *112*, 9016−9021.
(35) Bordin, J. R.; Diehl, A.; Barbosa, M. C. Relation between flow enhancement factor and structure for core-softened fluids inside nanotubes. *J. Phys. Chem. B* **2013**, *117*, 7047−7056.
(36) Bordin, J. R.; de Oliveira, A. B.; Diehl, A.; Barbosa, M. C. Diffusion enhancement in core-softened fluid confined in nanotubes. *J. Chem. Phys.* **2012**, *137*, No. 084504.
(37) Fomin, Y. D.; Ryzhov, V. N.; Tsiok, E. N. The behaviour of water and sodium chloride solution confined into asbestos nanotube. *Mol. Phys.* **2016**, *114*, 2279−2288.
(38) De Marzio, M.; Camisasca, G.; Conde, M. M.; Rovere, M.; Gallo, P. Structural properties and fragile to strong transition in confined water. *J. Chem. Phys.* **2017**, *146*, No. 084505.
(39) Gallo, P.; Rovere, M. Mode coupling and fragile to strong transition in supercooled TIP4P water. *J. Chem. Phys.* **2012**, *137*, No. 164503.
(40) Gallo, P.; Rovere, M.; Chen, S.-H. Water confined in MCM-41: A mode coupling theory analysis. *J. Phys.: Condens. Matter* **2012**, *24*, No. 064109.
(41) Krott, L. B.; Bordin, J. R.; Barraz, N. M.; Barbosa, M. C. Effects of confinement on anomalies and phase transitions of core-softened fluids. *J. Chem. Phys.* **2015**, *142*, No. 134502.
(42) Gavazzoni, C.; Giovambattista, N.; Netz, P. A.; Barbosa, M. C. Structure and mobility of water confined in AlPO4-54 nanotubes. *J. Chem. Phys.* **2017**, *146*, No. 234509.
(43) Bordin, J. R.; Krott, L. B.; Barbosa, M. C. Surface phase transition in anomalous fluid in nanoconfinement. *J. Phys. Chem. C* **2014**, *118*, 9497−9506.
(44) Farimani, A. B.; Aluru, N. R. Existence of multiple phases of water at nanotube interfaces. *J. Phys. Chem. C* **2016**, *120*, 23763−23771.
(45) Mashl, R. J.; Joseph, S.; Aluru, N. R.; et al. Anomalously immobilized water: A new water phase induced by confinement in nanotubes. *Nano Lett.* **2003**, *3*, 589.
(46) Farimani, A. B.; Aluru, N. R. Spatial diffusion of water in carbon nanotubes: From fickian to ballistic motion. *J. Phys. Chem. B* **2011**, *115*, 12145−12149.

DOI: 10.1021/acs.jpcc.8b00112
J. Phys. Chem. C 2018, 122, 6684−6690

Appendix D

THE JOURNAL OF CHEMICAL PHYSICS **148**, 222804 (2018)

2D nanoporous membrane for cation removal from water: Effects of ionic valence, membrane hydrophobicity, and pore size

Mateus Henrique Köhler,[1,a)] José Rafael Bordin,[2,b)] and Marcia C. Barbosa[1]
[1]*Instituto de Física, Universidade Federal do Rio Grande do Sul, Caixa Postal 15051, 91501-970 Porto Alegre, Brazil*
[2]*Campus Caçapava do Sul, Universidade Federal do Pampa, Av. Pedro Anunciação 111, CEP 96570-000 Caçapava do Sul, Brazil*

(Received 14 November 2017; accepted 8 January 2018; published online 13 February 2018)

Using molecular dynamic simulations, we show that single-layers of molybdenum disulfide (MoS_2) and graphene can effectively reject ions and allow high water permeability. Solutions of water and three cations with different valencies (Na^+, Zn^{2+}, and Fe^{3+}) were investigated in the presence of the two types of membranes, and the results indicate a high dependence of the ion rejection on the cation charge. The associative characteristic of ferric chloride leads to a high rate of ion rejection by both nanopores, while the monovalent sodium chloride induces lower rejection rates. Particularly, MoS_2 shows 100% of Fe^{3+} rejection for all pore sizes and applied pressures. On the other hand, the water permeation does not vary with the cation valence, having dependence only with the nanopore geometric and chemical characteristics. This study helps us to understand the fluid transport through a nanoporous membrane, essential for the development of new technologies for the removal of pollutants from water. *Published by AIP Publishing.* https://doi.org/10.1063/1.5013926

I. INTRODUCTION

Centuries of misuse of natural resources have stressed available freshwater supplies throughout the world. With the rapid development of industries, chemical waste has been thrown deliberately into the water to the point of making it difficult to clean. Particularly, direct or indirect discharge of heavy metals into the environment has increased recently, especially in developing countries.[1] Unlike organic contaminants, heavy metals are not biodegradable and tend to accumulate in living organisms. Many heavy metal ions are also known to be toxic or carcinogenic.[2] Toxic heavy metals of particular concern in the treatment of industrial waste-water include zinc, copper, iron, mercury, cadmium, lead, and chromium.

As a result, the filtration process that can acquire freshwater from contaminated, brackish water or seawater is an effective method to also increase the potable water supply. Modern desalination is mainly based on reverse osmosis (RO) performed through membranes due to their low energy consumption and easy operation. Current RO plants have already been operated near the thermodynamic limit, with the applied pressure being only 10%–20% higher than the osmotic pressure of the concentrate.[3] Meanwhile, advances in nanotechnology have inspired the design of novel membranes based on two-dimensional (2D) nanomaterials. Nanopores with diameters ranging from a few Angstroms to several nanometers can be drilled in membranes to fabricate molecular sieves.[4] As the diameter of the pore approaches the size of the hydrated ions, various types of ions can be rejected by nanoporous membranes, leading to efficient water desalination. Graphene (Gra), a single-atom-thick carbon membrane, was demonstrated to have several orders of magnitude higher flux rates when compared with conventional zeolite membranes.[5] In this way, graphene and graphene oxide are one of the most prominent materials for highly efficient membranes.[6–8] More recently, other 2D materials have also been investigated for water filtration. A nanoporous single-layer of molybdenum disulfide (MoS_2) has shown a great desalination capacity.[9–11] The possibility to craft the pore edge with Mo, S, or both provides flexibility to design the nanopore with desired functionality. In the same way, boron nitride nanosheets have also been investigated for water purification from distinct pollutants.[12,13] Therefore, for the purpose of cleaning water, not only the nanopore size but also the hydrophobicity and the geometry of the porous membrane are considered.

For instance, the performance of the commercial RO membrane is usually on the order of 0.1 L/cm^2 day MPa (1.18 g/m^2 s atm).[14] With the aid of zeolite nanosheets, permeability as high as 1.3 L/cm^2 day MPa can be obtained.[15] Recent studies have shown that MoS_2 nanopore filters have the potential to achieve a water permeability of roughly 100 g/m^2 s atm[10]—2 orders of magnitude higher than the commercial RO. This is comparable with that measured experimentally for the graphene filter (~70 g/m^2 s atm) under similar conditions.[16] These results have shown that the water permeability scales linearly with the pore density. Therefore, the water filtering performance of 2D nanopores can be even higher.

Controlling the size and shape of the pores created in these membranes, however, represents a huge experimental challenge. Inspired by a number of molecular dynamics (MD) studies predicting ultrahigh water permeability across graphene

[a)]Electronic mail: mateus.kohler@ufrgs.br
[b)]Electronic mail: josebordin@unipampa.edu.br

and other 2D nanoporous membranes,[11,17] technologies have been developed to create and control the nanopore size and distribution. Methods including electron beam,[18] ion irradiation,[19] and chemical etching[20] have been reported to introduce pores in graphene. Feng *et al.*[21] have also developed a scalable method to controllably make nanopores in single-layer MoS_2 with subnanometer precision using the electrochemical reaction (ECR). Recently, Liu and colleagues[22] investigated the geometrical effect of the nanopore shape on ionic blockage induced by DNA translocation through h-BN and MoS_2 nanopores. They observed a geometry-dependent ion scattering effect and further proposed a modified ionic blockage model which is highly related to the ionic profile caused by geometrical variations. Additionally, recent experimental efforts have been devoted to amplify the filtering efficiency of the nanoporous membranes. Wang and colleagues[23] mechanistically related the performance of MoS_2 membranes to the size of their nanochannels in different hydration states. They attributed the high water flux (30-250 L/m^2 h bars) of MoS_2 membranes to the low hydraulic resistance of the smooth, rigid MoS_2 nanochannels. The membrane compaction with high pressure has also been found to create a neatly stacked nanostructure with minimum voids, leading to stable water flux and enhanced separation performance. By tuning the pore creation process, Jang *et al.*[24] have demonstrated nanofiltration membranes that reject small molecules but offer high permeance to water or monovalent ions. Also, studies have shown how defects, oxidation, and functionalization can affect the ionic blockage[25–27] All of these studies point to a near future where 2D membranes will have a major impact on desalination processes.

In this work, we address the issue of the selectivity of the porous membrane. In order to do that, we compare the water filtration capacity of MoS_2 and graphene through molecular dynamics simulations. While graphene is a purely hydrophobic material, MoS_2 sheets have both hydrophobic (S) and hydrophilic (Mo) sites. Recent studies have shown that the water dynamics and structure inside hydrophobic or hydrophilic pores can be quite distinct regarding the pore size[28–30] and even near hydrophobic or hydrophilic protein sites.[31] Three cations are considered: the standard monovalent sodium (Na^+), the divalent zinc (Zn^{2+}), and the trivalent iron (Fe^{3+}). The study of sodium removal is relevant due to its applications for water desalination.[32–34] Zinc is a trace element that is essential for human health. It is important for the physiological functions of living tissue and regulates many biochemical processes. However, excess of zinc can cause eminent health problems.[35] The cation Zn^{2+} is ranked 75th in the *Comprehensive Environmental Response, Compensation and Liability Act* (CERCLA) 2017 priority list of hazardous substances. In its trivalent form, ferric chloride Fe^{3+} Cl_3^- is a natural flocculant, with high power of aggregation. It is also on the CERCLA list with recommended limit concentration of 0.3 mg/l. In this way, we explore the water permeation and cations rejection by nanopore with distinct radii. Our results show that the hydrophilic/hydrophobic MoS_2 nanopores have a higher salt rejection in all scenarios, while the purely hydrophobic graphene nanopores have a higher water permeation. Especially, MoS_2 membranes show the impressive capacity of blocking all the trivalent iron cations regardless of the nanopore size.

Our paper is organized as follows. In Sec. II, we introduce our model and the details about the simulation method. In Sec. III, we show and discuss our results for the water permeation in the distinct membranes, while in Sec. IV, we show the ion rejection properties for each case. Finally, a summary of our results and the conclusions are shown in Sec. V.

II. COMPUTATIONAL DETAILS AND METHODS

Molecular dynamics (MD) simulations were performed using the Large-scale Atomic/Molecular Massively Parallel Simulator (LAMMPS) package.[36] A typical simulation box consists of a graphene sheet acting as a rigid piston in order to apply an external force (pressure) over the ionic solution. The pressure gradient forces the solution against the 2D nanopore:

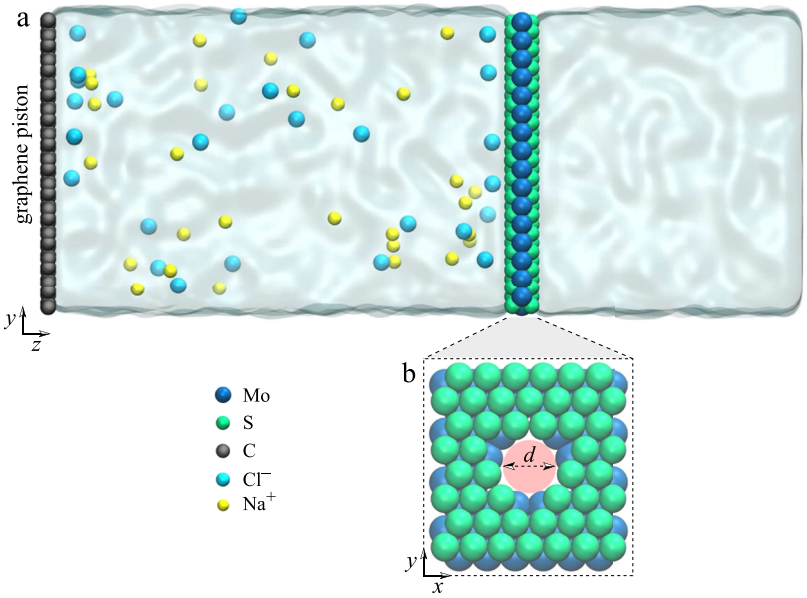

FIG. 1. (a) Schematic representation of the simulation framework. The system is divided as follows: On the left side we can see the piston (graphene) pressing the ionic solution (in this case, water + NaCl) against the MoS_2 nanopore. For the case of a graphene nanopore, the depiction is the same, but with a porous graphene sheet instead of the MoS_2 sheet. On the right side, we have bulk water. (b) Definition of the pore diameter d.

a single-layer of molybdenum disulfide or graphene. Figure 1 shows the schematic representation of the simulation framework.

A nanopore was drilled in both MoS_2 and graphene sheets by removing the desired atoms, as shown in Fig. 1. The accessible pore diameters considered in this work range from 0.26 to 0.95 nm for the MoS_2 (which means a pore area ranging from 5.5 to 71 Å^2) and 0.17–0.92 nm for the graphene (with area ranging from 2.5 to 67 Å^2). M. Heiranian *et al.*[11] have studied different MoS_2 nanopore compositions for water filtration: with only Mo, only S, and a mix of the two atoms at the pore's edge. They found similar ion rejection rates for both cases. Here, in order to account for circular nanopores, mixed pore edges have been chosen. The system contains 22 000 atoms distributed in a box with dimensions 5 × 5 × 13 nm in x, y, and z, respectively. Although the usual salinity of seawater is ∼0.6M, we choose a molarity of ∼ 1.0M for all the cations (Na^+, Zn^{2+}, and Fe^{3+}) due to the computational cost associated with low-molarity solutions.

The TIP4P/2005[37] water model was used and the SHAKE algorithm[38] was employed to maintain the rigidity of the water molecules. The non-bonded interactions are described by the Lennard-Jones (LJ) potential with a cutoff distance of 0.1 nm and the parameters tabulated in Table I. The Lorentz-Berthelot mixing rule was used to obtain the LJ parameters for different atomic species. The long-range electrostatic interactions were calculated by the *particle-particle-particle mesh* method.[39] Periodic boundary conditions were applied in all the three directions.

For each simulation, the system was first equilibrated for constant number of particles, pressure, and temperature (NPT) ensemble for 1 ns at P = 1 atm and T = 300 K. Graphene and MoS_2 atoms were held fixed in the space during equilibration, and the NPT simulations allow water to reach its equilibrium density (1 g/cm^3). After the pressure equilibration, a 5 ns simulation was carried out in the constant number of particles, volume, and temperature (NVT) ensemble to further equilibrate the system at the same T = 300 K. Finally, a 10 ns production run was carried out, also in the NVT ensemble. The Nosé-Hoover thermostat[44,45] was used at each 0.1 ps in both NPT and NVT simulations, and the Nosé-Hoover barostat was used to keep the pressure constant in the NPT simulations. Different external pressures were applied on the rigid piston to characterize the water filtration through the 2D (graphene and MoS_2) nanopores. For simplicity, the pores were held fixed in space to study solely the water transport and ion rejection properties of these materials. The external pressures range from 10 to 100 MPa. These are higher than the osmotic pressure used in the experiments. The reason for applying such high pressures at MD simulations with running time in nanosecond scale is that the low pressures would yield a very low water flux that would not go above the statistical error. We carried out three independent simulations for each system collecting the trajectories of atoms every picosecond.

TABLE I. The Lennard-Jones parameters and charges of the simulated atoms. The crossed parameters were obtained by Lorentz-Berthelot rule.

Interaction	σ (nm)	ε (kcal/mol)	Charge
C–C[40]	3.39	0.0692	0.00
Mo–Mo[41]	4.20	0.0135	0.60
S–S[41]	3.13	0.4612	–0.30
O–O[37]	3.1589	0.1852	–1.1128
H–H	0.00	0.00	0.5564
Na–Na[42]	2.52	0.0347	1.00
Cl–Cl[42]	3.85	0.3824	–1.00
Zn–Zn[43]	0.0125	1.960	2.00
Fe–Fe[43]	0.18	0.745	3.00

III. WATER FLUX

First, let us compare the flux performance of the graphene and the MoS_2 membranes. In Fig. 2, we show the water flux through 2D nanopores in number of molecules per nanosecond (MoS_2 and graphene) as a function of the applied pressure gradient for different pore diameters. The water is filtered from a reservoir containing an ionic solution of either monovalent sodium (Na^+), divalent zinc (Zn^{2+}), or trivalent iron cations (Fe^{3+}). In all cases, chlorine (Cl^-) was used as the standard anion. Four pore sizes for each material were investigated.

Our results indicate that for the smaller pore diameter, the black points in Fig. 2, both materials have the same water permeation. However, for the other values of pore diameter, the graphene membrane shows a higher water flux, for all applied pressure gradient. While the flux at the purely hydrophobic graphene pore for a fixed pressure monotonically increases with the pore diameter, this is not the case for the MoS_2 pore for which the flows show a minimum pore diameter of around 0.37 nm probably due to the nonuniform distribution of the hydrophobic and hydrophilic sites of the pore. Figures 2(a)–2(c) show that this behavior of the water flux is not affected by the cation valence, only by the applied pressure, by geometric effects, and by the pore composition. For instance, the 0.46 nm graphene pore shows enhanced water flux compatible with the 0.6 nm MoS_2 pore for all cations. Therefore, it is clear that pore composition affects the water permeation properties more than the water-ion interaction.

This result agrees with the findings by Aluru and his group,[11] where they showed that even a small change in pore composition can lead to enhanced water flux through a MoS_2 nanocavity. This is also consistent with our recent findings that the dynamics of water inside nanopores with diameter ≈1.0 nm is strongly affected by the presence of hydrophilic or hydrophobic sites.[29] This investigation, over distinct cation valences and membranes, highlights the importance of the nanopore physical-chemistry properties for water filtration processes.

To quantify the water permeability through the pores, we compute the permeability coefficient, p, across the pore. For dilute solutions,

$$p = \frac{j_w}{-V_w \Delta C_s + \frac{V_w}{N_A k_B T}\Delta P}, \quad (1)$$

where j_w is the flux of water (H_2O/ns), V_w is the molar volume of water (19 ml/mol), ΔC_s is the concentration gradient of the solute (1.0M), N_A is the Avogadro number, k_B is the Boltzmann

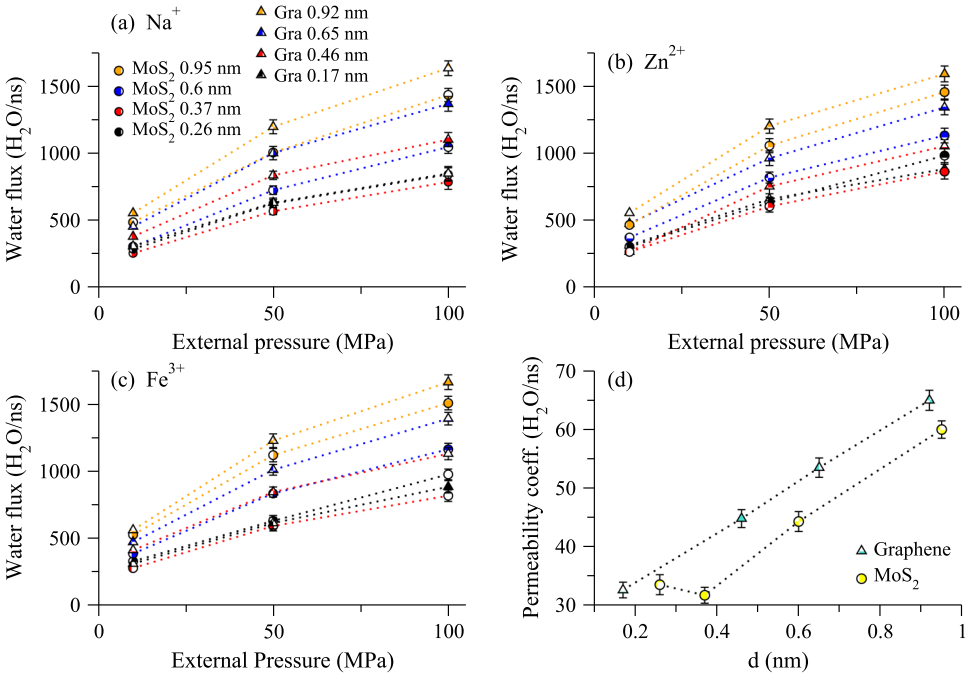

FIG. 2. Water flux as a function of the applied pressure for MoS_2 and graphene nanopores with similar pore areas. (a) Monovalent Na^+, (b) divalent Zn^{2+}, and (c) trivalent Fe^{3+} cations are considered for the ionic solution at the reservoir. (d) Water permeability through the pores as a function of the pore diameter for the case of $\Delta P = 50$ MPa. The dotted lines are a guide to the eye.

constant, T is the temperature (300 K), and ΔP is the applied hydrodynamic pressure (MPa).

The case of $\Delta P = 50$ MPa is shown in Fig. 2(d). The permeability coefficient of the MoS_2 ranges from approximately 33 to 55 H_2O/ns for the 0.26 and 0.95 nm diameters, respectively. The graphene nanopore presents a permeability coefficient of ~34–63 H_2O/ns as the pore diameter is varied from 0.17 to 0.92 nm, respectively. For smaller pores, the difference between MoS_2 and graphene is inside the error bars, whereas for the larger pores, both materials exhibit high permeability rates, with a slight advantage in the case of graphene.

The water structure and dynamics inside nanopores are strongly related.[29,46] Therefore, distinct structural regimes can lead to different diffusive behaviors. In Fig. 3, we present the distribution of water molecules in the z-direction inside the MoS_2 (solid line) and graphene (dotted line) nanopores. As for the water flux, the water axial distribution is not affected by the cation valence. Therefore, for simplicity and since there are more studies about monovalent salts, we show only the Na^+ case. The nanopore length in the z-direction, considering the van der Waals diameter for each sheet, is 0.63 (−0.315–0.315) nm for the MoS_2 and 0.34 (−0.17–0.17) nm for the graphene. The structures inside both pores are considerably different. For the graphene nanopore, shown in Fig. 3(a), there is no favorable positions for the water molecules to remain throughout the simulation. This can be related to the hydrophobic characteristic of the graphene sheet and the high slippage observed for water inside carbon nanopores.[47,48] Since all the pore is hydrophobic, there is no preferable position for the water molecules, and the permeability is higher. On the other hand, along the MoS_2 cavity we can observe a high structuration in three sharp peaks, as shown in Fig. 3(b). This structuration comes from the existence of hydrophilic (Mo) and hydrophobic sites (S atoms). This layered organization within the MoS_2 nanopore can be linked to the reduced flux compared with graphene, since it implies an additional term in the energy required for the water molecule to pass through the pore.

The higher water flux through graphene nanopores compared with MoS_2 implies that for a desired water flux, a smaller applied pressure is needed. Nevertheless, it is important to note that both fluxes are higher, especially when compared with current desalination technologies.[11,49] Therefore, both materials are capable of providing a high water permeability. The question is whether these materials are also able to effectively clean the water by removing the ions.

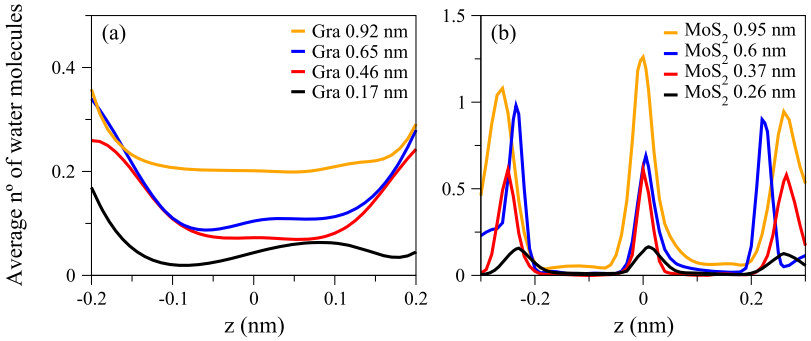

FIG. 3. Averaged axial distribution of water molecules inside the (a) graphene (Gra) and (b) MoS_2 nanopores with distinct diameters. Here, z = 0 is at the center of the pore, the external pressure is $\Delta P = 10$ MPa, and the cation is the Na^+.

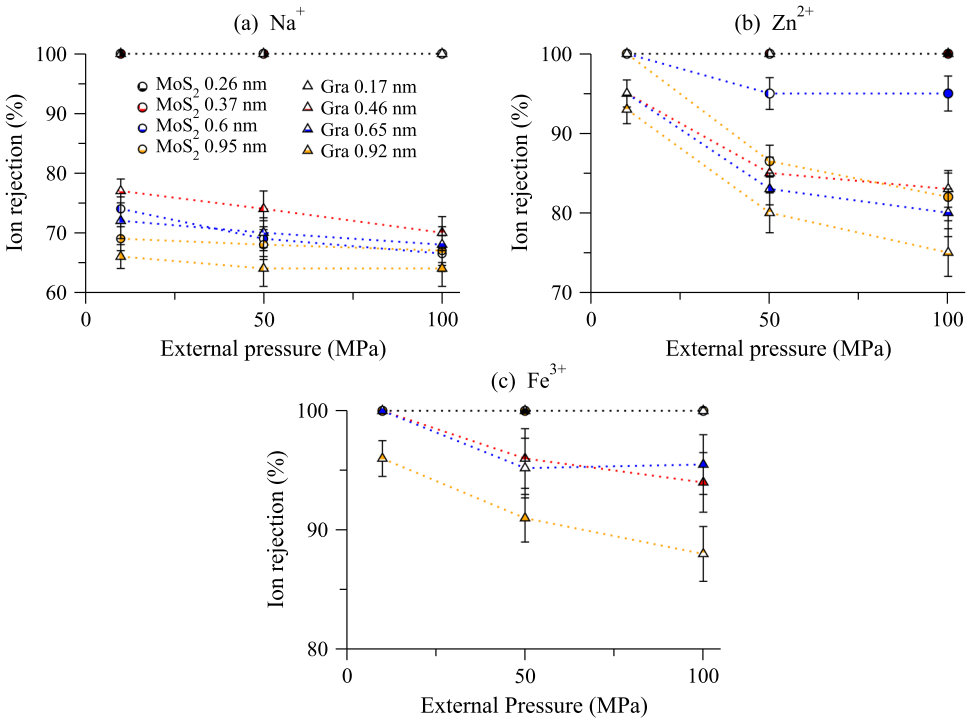

FIG. 4. Percentage of ion rejection by various pores as a function of the applied pressure. Pores with different diameters are considered.

IV. ION REJECTION EFFICIENCY

The other important aspect for the cleaning of water is the membrane's ability to separate water and ions. In this way, we investigate how the cation valence and the pore size affect the percentage of rejected ions. In Fig. 4, we show the percentage of total ions rejected by the 2D nanopores as a function of the applied pressure for the three cations. The pore diameters are the same as discussed in Sec. III.

The ion rejection by the smallest pores, 0.17 and 0.26 nm for graphene and MoS_2, respectively, was 100% for all applied pressures and cation solutions. This is expected since the

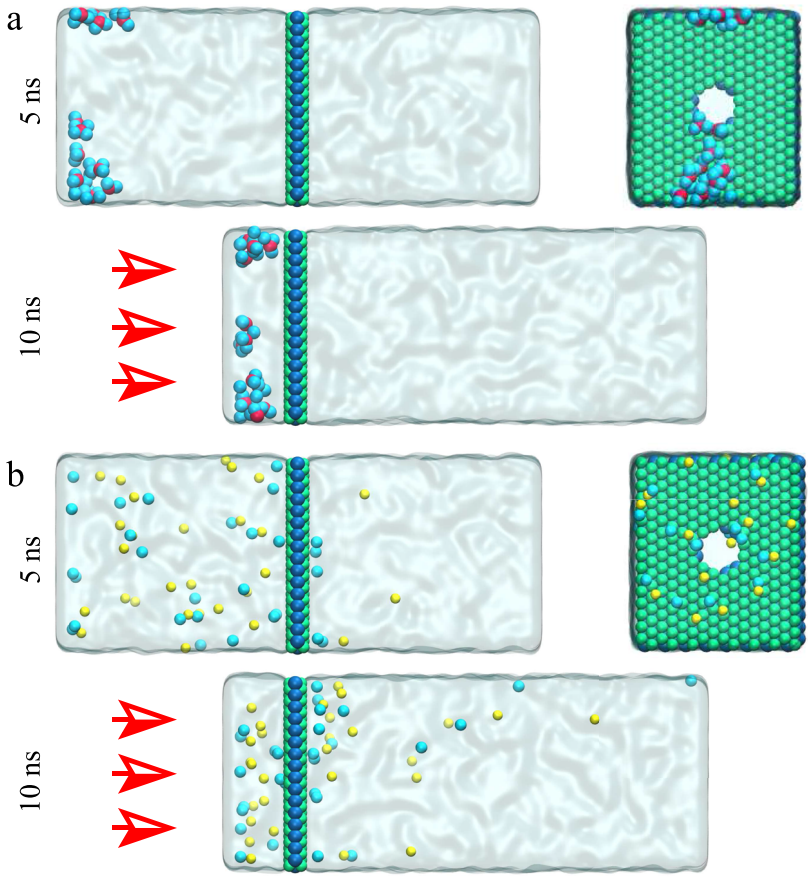

FIG. 5. Side and front view snapshots of (a) Fe^{3+} Cl^- cluster formation preventing the ion passage through a 0.95 nm MoS_2 nanopore and (b) monovalent Na^+ Cl^- passing through the same nanopore without clusterization for an external applied pressure of 50 MPa.

pore size is much smaller than the hydration radii of the cations. Therefore, it is more energetically favorable for the cation to remain in the bulk solution instead of stripping off the water and entering the pore.[50] As the pore diameter increases, this energetic penalty becomes smaller. In addition, the valence plays a crucial role here, with the monovalent ions having a smaller penalty than divalent and trivalent cations. In this way, for the nanopores with diameters 0.37 nm and 0.46 nm for graphene and MoS_2, respectively, Na^+ and Cl^- ions flow through the pore reducing the rejection efficiency for both materials, as we can see in Fig. 4(a). However, it is important to note that the ion rejection performance of molybdenum disulfide membranes is superior to that observed for graphene membranes for all ranges of pressure, sizes, and cation valences. For instance, for the divalent case Zn^{2+}, shown in Fig. 4(b), and the smaller ΔP, the rejection is 100% for all pore sizes in the MoS_2 membrane, while for the graphene membrane, we observe cation permeation for the bigger pores.

The MoS_2 membrane shows a very good performance for the rejection of the trivalent cation Fe^{3+}. As Fig. 4(c) shows, for all nanopore sizes and applied pressures the rejection is 100%. Such efficiency was not observed in the graphene membranes, were only the case with small pore diameter as 100% of iron rejection. Here, we should address that not only the hydration shell plays an important role in the cations rejection. While sodium chloride is uniformly dispersed in water and we do not observe clusters at the simulated concentration, the iron cations tend to form large clusters of ferric chlorides in solution, as shown in Fig. 5. Moreover, we observe these structures throughout the whole simulation, and even at high-pressure regime the clusters remain too large to overcome the pore. In fact, ferric chlorides are effective as primary coagulants due to their associative character in solution. At controlled concentrations, it is excellent for both drinking and wastewater treatment applications, including phosphorus removal,[51] sludge conditioning, and struvite control.[52,53] It also prevents odor and corrosion by controlling hydrogen sulfide formation. Additionally, our results indicate that the associative properties of ferric chlorides can be used to increase the efficiency of salt rejection by both MoS_2 and graphene nanopores, which may contribute in water cleaning devices.

V. SUMMARY AND CONCLUSIONS

We have calculated water fluxes through various MoS_2 and graphene nanopores and the respective percentage of the total ions rejected by both materials as a function of the applied pressure gradient. Our results indicate that 2D nanoporous membranes are promising for water purification and salt rejection. The selectivity of the membranes was found to depend on factors such as the pore diameter, the cationic valence, and the applied pressure. Nevertheless, our results show that the ion valency does not affect the water permeation—it is only affected by the pore size and chemical composition.

Particularly, our findings indicate that graphene is a better water conductor than MoS_2, with a higher permeability coefficient, although both materials have presented high water fluxes. On the other hand, MoS_2 nanopores with water-accessible pore diameters ranging from 0.26 to 0.95 nm strongly reject ions even at theoretically high pressures of 100 MPa. Additionally, the rejection is shown to depend strongly on the ion valence. It reaches 100% for trivalent ferric chloride (Fe^{3+} Cl_3^-) for all MoS_2 pore sizes and applied pressures. This is a direct result of the ability of heavy metals to form agglomerates, eventually exhibiting long ionic chains. At the same time, this did not affect the water flux. Then, the ferric chloride properties can be used to improve the effectiveness of 2D material-based nanofilters. New studies are performed in this direction.

ACKNOWLEDGMENTS

We thank the Brazilian agencies CNPq and INCT-FCx for the financial support and CENAPAD/SP and CESUP/UFRGS for the computer time.

[1] D. Ko, J. S. Lee, H. A. Patel, M. H. Jakobsen, Y. Hwange, C. T. Yavuzan, H. B. Hansen, and H. R. Andersen, J. Hazard. Mater. **332**, 140 (2017).
[2] M. B. Gumpu, S. Sethuraman, U. M. Krishnan, and J. B. B. Rayappan, Sens. Actuators, B **213**, 515 (2015).
[3] M. Li, Desalination **422**, 124 (2017).
[4] L. Wang, M. S. H. Boutilier, P. R. Kidambi, D. Jang, N. G. Hadjiconstantinou, and R. Karnik, Nat. Nanotechnol. **12**, 509 (2017).
[5] K. Celebi, J. Buchheim, R. M. Wyss, A. Droudian, P. Gasser, I. Shorubalko, J.-I. Kye, C. Lee, and H. G. Park, Science **344**, 289 (2014).
[6] Q. Xu, H. Xu, J. Chen, Y. Lv, C. Dong, and T. S. Sreeprasadc, Inorg. Chem. Front. **2**, 417 (2015).
[7] K. C. Kemp, H. Seema, M. Saleh, N. H. Le, K. Mahesh, V. Chandra, and K. S. Kim, Nanoscale **5**, 3149 (2013).
[8] L. Huang, M. Zhang, C. Li, and G. Shi, J. Phys. Chem. Lett. **6**, 2806 (2015).
[9] J. Kou, J. Yao, L. Wu, X. Zhou, H. Lu, F. Wu, and J. Fan, Phys. Chem. Chem. Phys. **18**, 22210 (2016).
[10] W. Li, Y. Yang, J. K. Weber, G. Zhang, and R. Zhou, ACS Nano **10**, 1829 (2016).
[11] M. Heiranian, A. B. Farimani, and N. R. Aluru, Nat. Commun. **6**, 8616 (2015).
[12] W. Lei, D. Portehault, D. Liu, S. Qin, and Y. Chen, Nat. Commun. **4**, 1777 (2013).
[13] J. Azamat, B. S. Sattary, A. Khataee, and S. W. Joo, J. Mol. Graphics Modell. **61**, 13 (2015).
[14] M. M. Pendergast and E. M. Hoek, Energy Environ. Sci. **4**, 1946 (2011).
[15] S. H. Jamali, T. J. H. Vlugt, and L.-C. Lin, J. Phys. Chem. C **121**, 11273 (2017).
[16] S. P. Surwade, S. N. Smirnov, I. V. Vlassiouk, R. R. Unocic, G. M. Veith, S. Dai, and S. M. Mahurin, Nat. Nanotechnol. **10**, 459 (2015).
[17] D. Cohen-Tanugi and J. C. Grossman, Nano Lett. **12**, 3602 (2012).
[18] S. Garaj, W. Hubbard, A. Reina, J. Kong, D. Branton, and J. A. Golovchenko, Nature **467**, 190 (2010).
[19] K. Yoon, A. Rahnamoun, J. L. Swett, V. Iberi, D. A. Cullen, I. V. Vlassiouk, A. Belianinov, S. Jesse, X. Sang, O. S. Ovchinnikova, A. J. Rondinone, R. R. Unocic, and A. C. van Duin, ACS Nano **10**, 8376 (2016).
[20] S. C. OHern, D. Jang, S. Bose, J.-C. Idrobo, Y. Song, T. Laoui, J. Kong, and R. Karnik, Nano Lett. **15**, 3254 (2015).
[21] J. Feng, K. Liu, M. Graf, M. Lihter, R. D. Bulushev, D. Dumcenco, D. T. L. Alexander, D. Krasnozhon, T. Vuletic, A. Kis, and A. Radenovic, Nano Lett. **15**, 3431 (2015).
[22] K. Liu, M. Lihter, A. Sarathy, S. Caneva, H. Qiu, D. Deiana, V. Tileli, D. T. L. Alexander, S. Hofmann, D. Dumcenco, A. Kis, J.-P. Leburton, and A. Radenovic, Nano Lett. **17**, 4223 (2017).
[23] Z. Wang, Q. Tu, S. Zheng, J. J. Urban, S. Li, and B. Mi, Nano Lett. **17**, 7289 (2017).
[24] D. Jang, J.-C. Idrobo, T. Laoui, and R. Karnik, ACS Nano **11**, 10042 (2017).
[25] J. L. Achtyl, R. R. Unocic, L. Xu, Y. Cai, M. Raju, W. Zhang, R. L. Sacci, I. V. Vlassiouk, P. F. Fulvio, P. Ganesh, D. J. Wesolowski, S. Dai, A. C. T. van Duin, M. Neurock, and F. M. Geiger, Nat. Commun. **6**, 6539 (2015).

[26]G. Levita, P. Restuccia, and M. Righi, Carbon **107**, 878 (2016).
[27]J. Abrahamand, K. S. Vasu, C. D. Williams, K. Gopinadhan, Y. Su, C. T. Cherian, J. Dix, E. Prestat, S. J. Haigh, I. V. Grigorieva, P. Carbone, A. K. Geim, and R. R. Nair, Nat. Nanotechnol. **12**, 546 (2017).
[28]I. Moskowitz, M. A. Snyder, and J. Mittal, J. Chem. Phys. **141**, 18C532 (2014).
[29]M. H. Köhler, J. R. Bordin, L. B. da Silva, and M. C. Barbosa, Phys. Chem. Chem. Phys. **19**, 12921 (2017).
[30]J. R. Bordin and M. C. Barbosa, Phys. A: Stat. Mech. Appl. **467**, 137 (2017).
[31]M. H. Köhler, R. C. Barbosa, L. B. da Silva, and M. C. Barbosa, Phys. A: Stat. Mech. Appl. **468**, 733 (2017).
[32]B. Corry, J. Phys. Chem. B **112**, 1427 (2008).
[33]R. Das, M. E. Ali, S. B. A. Hamid, S. Ramakrishna, and Z. Z. Chowdhury, Desalination **336**, 97 (2014).
[34]K. A. Mahmoud, B. Mansoor, A. Mansour, and M. Khraisheh, Desalination **356**, 208 (2015).
[35]F. Fu and Q. Wang, J. Environ. Manage. **92**, 407 (2011).
[36]S. Plimpton, J. Comput. Phys. **117**, 1 (1995).
[37]J. Abascal and C. Vega, J. Chem. Phys. **123**, 234505 (2005).
[38]J. P. Ryckaert, G. Ciccotti, and H. J. C. Berendsen, J. Comput. Phys. **23**, 327 (1977).
[39]R. W. Hockney and J. W. Eastwood, *Computer Simulation Using Particles* (McGraw-Hill, New York, 1981).
[40]A. Barati Farimani and N. R. Aluru, J. Phys. Chem. B **115**, 12145 (2011).
[41]T. Liang, S. R. Phillpot, and S. B. Sinnott, Phys. Rev. B **79**, 245110 (2009).
[42]R. Fuentes-Azcatl and M. C. Barbosa, J. Phys. Chem. B **120**, 2460 (2016).
[43]K. R. Hinkle, C. J. Jameson, and S. Murad, J. Chem. Eng. Data **61**, 1578 (2016).
[44]S. Nosé, Mol. Phys. **52**, 255 (1984).
[45]W. G. Hoover, Phys. Rev. A **31**, 1695 (1985).
[46]J. R. Bordin, A. Diehl, and M. C. Barbosa, J. Phys. Chem. B **117**, 7047 (2013).
[47]K. Falk, F. Sedlmeier, L. Joly, R. R. Netz, and L. Bocquet, Nano Lett. **10**, 4067 (2010).
[48]G. Tocci, L. Joly, and A. Michaelides, Nano Lett. **14**, 6872 (2014).
[49]J. Azamat and A. Khataee, Comput. Mater. Sci. **137**, 201 (2017).
[50]J. R. Bordin, A. Diehl, M. C. Barbosa, and Y. Levin, Phys. Rev. E **85**, 031914 (2012).
[51]B. Kim, M. Gautier, P. Molle, P. Michel, and R. Gourdon, Ecol. Eng. **80**, 53 (2015).
[52]O. Amuda and I. Amoo, J. Hazard. Mater. **141**, 778 (2007).
[53]J. Sun, I. Pikaar, K. R. Sharma, J. Keller, and Z. Yuan, Water Res. **71**, 150 (2015).

Appendix E

2D nanoporous membrane for cation removal from water: Maximum desalination by iron flocculation

Mateus Henrique Köhler,[1, a)] José Rafael Bordin,[2, b)] and Marcia C. Barbosa[1]

[1)] *Instituto de Física, Universidade Federal do Rio Grande do Sul, Caixa Postal 15051, 91501-970, Porto Alegre, Brazil*

[2)] *Departamento de Física, Instituto de Física e Matemática, Universidade Federal de Pelotas, Caixa Postal 354, 96010-900, Pelotas, Brazil*

In our previous work [J. Chem. Phys. 148, 222804 (2018)] we have studied the effectiveness of nanoporous graphene and molybdenum disulfide to remove cations with distinct valences from water. Inspired by that work, we now employ Molecular Dynamics simulations of a mixture of 1:1 and 3:1 salts. We explore the effect of adding ferric chloride as a flocculant to an aqueous sodium chloride solution. The NaCl rejection by the nanomembranes is enhanced due to the addition of the multivalent cation from ∼70% to 100%. Our findings indicate that the mechanism behind this effect is the ionic clustering due to the presence of the multivalent ion combined with the dielectric discontinuity at the nanopore. This result shows that a simple flocculant can maximize the water desalination by nanopores.

Keywords: desalination, nanopores, molybdenum disulfide, graphene

[a)] Electronic mail: mateus.kohler@ufrgs.br

[b)] Electronic mail: jrbphys@gmail.com

I. INTRODUCTION

Two-dimensional (2D) nanoporous membranes have stood out in the last decade as prominent materials for cleaning water, combining the unique molecular sieving properties with the fast permeation[1]. Recent advances in this field have allowed the introduction of 2D materials with tunable pore diameters and shapes[2,3], which are prerequisites for the industrial-scale production. Since the superflow of water observed in carbon nanotubes is not affected by the thickness of the membrane[4], it is possible to develop nano-sheet-based[5–10] membranes as molecular sieving for water desalination. These materials, due to its single-atom thickness and mechanical robustness, became more attractive as membranes than structures such as conventional zeolite. As a consequence, several studies have focused on the chemical functionalization of the graphene nanopores[11–13]. In addition, 2D materials with hydrophilic and hydrophobic sites, such as the molybdenum disulfide (MoS_2) nanopores, were investigated[14,15]. A nano-sheet of MoS_2 consists of a middle layer of molybdenum sandwiched between two sulfur layers, with thickness of ∼1 nm and a robust Young's modulus of ∼300 GPa[16] (comparable to the Young's modulus of steel).

The performance of current commercial reverse osmosis (RO) membrane is usually on the order of 0.1 L/cm^2·day·MPa (1.18 g/m^2·s·atm)[17]. With the aid of zeolite nanosheets, permeability high as 1.3 L/cm^2·day·MPa can be obtained[18]. Recent studies have demonstrated that the MoS_2 nanopore filters can achieve very high water permeability of the order of 100 g/m^2·s·atm[15] – two orders of magnitude higher than the commercial RO. This is comparable with the permeability measured experimentally for the graphene filter (∼70 g/m^2·s·atm) under similar conditions[19]. All of these results illustrate the high potential of 2D nanoporous membranes in desalination processes.

Although 2D membranes represent a huge step towards efficient water filtration, there are still experimental challenges concerning the nanopore tailoring. Some progress, however, has been made to produce sub-nanometer controlled nanopores. Methods including electron beam[20], ion irradiation[21] and chemical etching[22] have been applied to introduce nanopores in graphene. Using a highly focused electron beam, and transmission electron microscope, versatile nanopores with diameters ranging from subnanometer to 10 nm were sculpted successfully in MoS_2 membranes[23]. Feng et al.[24] have developed a scalable method to controllably make nanopores in single-layer MoS_2 with subnanometer precision using electrochemical re-

action (ECR). Fabrication of individual nanopores in hexagonal boron nitride (h-BN) with atomically precise control of the pore shape and size has been also reported[25]. Another challenge lies in accurately measure the size of the manufactured nanopore. Attempts have been made to extract this information from the material's conductance[26]. Recently, Wen and colleagues[27] have introduced the concept of effective transport length in order to accurate determines graphene and MoS_2 nanopore's diameter using conductance measurements.

Despite the experimental efforts, the nanopores are often larger than the ion cross section. One way to get around this is to reduce the nanopore accessible area, but this lowers the water flux, which is not desirable. Another way to induce larger desalination rates is to increase the ionic cross section to avoid ion passage through the membrane.

In this paper, we report a large increase in the salt rejection by graphene and MoS_2 membranes by adopting a new approach which goes as follows. Instead of just pressing a NaCl solution against the nanomembrane, a flocculant ingredient, the ferric chloride ($Fe^{3+}Cl^{-}$), is added to the solution. The idea is to induce the monovalent ions to aggregate to the trivalent cation through a charge reversion mechanism[28,29]. Although in recent years a considerable amount of interest has been dedicated to the investigation of desalination processes using nanomembranes, to the best of our knowledge, the nanopore plus nano flocculant approach has not been investigated so far. We choose ferric chloride as flocculant once it is easily accessible, have a low cost, is an essential element for living organisms at low concentrations, and when at high concentrations can be easily removed from water.

II. MODELS AND METHODS

Two systems are analyzed: one using a MoS_2 membrane and the other using a graphene membrane. Each simulation box has at one end a graphene sheet acting as a rigid piston which applies an external force (pressure) on the ionic solution. The pressure gradient forces the solution against the 2D nanopore at the membrane located at the center of the box, as depicted in the Fig. 1(a). The nanopore, with an accessible diameter of $\sim$1 nm and illustrated in the Fig. 1(b), is located at the center of both the MoS_2 and the graphene sheets. The system contains 22000 atoms distributed in a box with dimensions $5 \times 5 \times 13$ nm in x, y and z directions, respectively.

The ionic solution – pure sodium chloride or mixture of sodium and iron chloride – has a

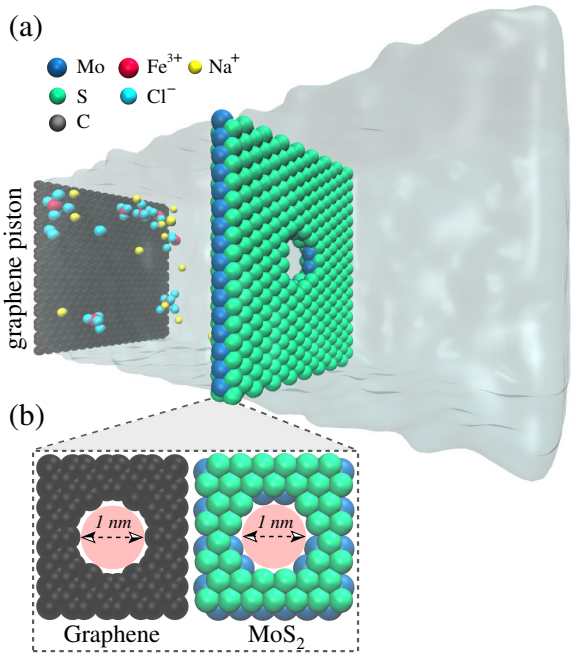

FIG. 1. (a) Schematic representation of the simulation framework. The system is divided as follows: On the left side we can see the piston (graphene) pressing the ionic solution (water, Fe^{3+}, Na^{+}, Cl^{-}) against the MoS_2 (or graphene) nanopore. On the right side we have bulk water. (b) Definition of the pore diameter for each membrane.

total molarity of 1 M in all simulations. Although larger than the salinity of seawater ($\sim$ 0.6 M), it is in the same scale range and still reduces the computational cost associated with low-molarity solutions. We do not expect that this difference would change the behavior of the macroions. In order to study the effect of adding the ferric chloride to the NaCl solution, we investigate solutions with 20, 35 and 50% of Fe^{3+} ions.

The TIP4P/2005[30] water model was used and the SHAKE algorithm[31] was employed to maintain the rigidity of the water molecules. The non-bonded interactions are described by the Lennard-Jones (LJ) potential with a cutoff distance of 0.1 nm. The reader is referred to our previous work, reference[32], for more details about the parameters used in the simulations. The long-range electrostatic interactions were calculated by the *Particle Particle Particle Mesh* method[33]. Periodic boundary conditions were applied in the in-plane direction of the nanoporous membrane.

For each simulation, the system was first equilibrated in the NPT ensemble for 1 ns at P =1 atm and T = 300 K. Graphene and MoS_2 atoms were held fixed in the space during

equilibration and the NPT simulations allow water to reach its equilibrium density (1 g/cm^3). After the pressure equilibration, a 10 ns simulation in the NVT ensemble was performed to further equilibrate the system at the same T = 300 K. Finally, a 10 ns production run were carried out, also in the NVT ensemble. Then different external pressures (10,50 and 100 MPa) were applied on the rigid piston to characterize the water filtration through the 2D (graphene and MoS_2) nanopores. We use such high pressures at MD simulations because low water flux would not go above the statistical error. The Nosé-Hoover thermostat[34,35] was used at each 0.1 ps in both NPT and NVT simulations, and the Nosé-Hoover barostat[36] was used to keep the pressure constant in the NPT simulations. For simplicity, the pores were held fixed in space to study solely the water transport and ion rejection properties of these materials. We carried out three independent simulations for each system collecting the trajectories of atoms every picoseconds.

III. RESULTS AND DISCUSSION

The most important aspect in water desalination is the ability of the membrane to reject ions. This task is either facilitated or complicated by some factors such as the nanopore's chemistry, size and shape, as well as the valence of the ion to be blocked[32]. The finite pore length effect have several consequences on the ionic structures[37], including decreasing the large ion repulsion due to the dielectric discontinuity[38]. Therefore, the ionic structuration and charge distribution are aspects that can be further explored in desalination processes through nanoporous membranes.

The percentage of total ions rejected by the MoS_2 and graphene nanopores is plotted as a function of the applied pressure in Fig. 2. For low iron concentrations, the Figures 2(a) and (b) show that the ion rejection decreases with the increase of pressure for both membranes. The higher pressures induce higher forces on the ions, allowing them to overcome the entropic and the dielectric barrier at the pore entrance. For higher iron concentrations, however, this is not the case. A complete ion rejection is observed for 35 and 50% of ferric chloride for the MoS_2 membrane and 50% of ferric chloride for the graphene membrane. The addition of ferric chloride increases the ion rejection by $\sim$30% for the MoS_2 and $\sim$32% for the graphene membranes when compared with the system without the flocculant. Additionally, the overall desalination is higher for the MoS_2 membrane compared with graphene, which

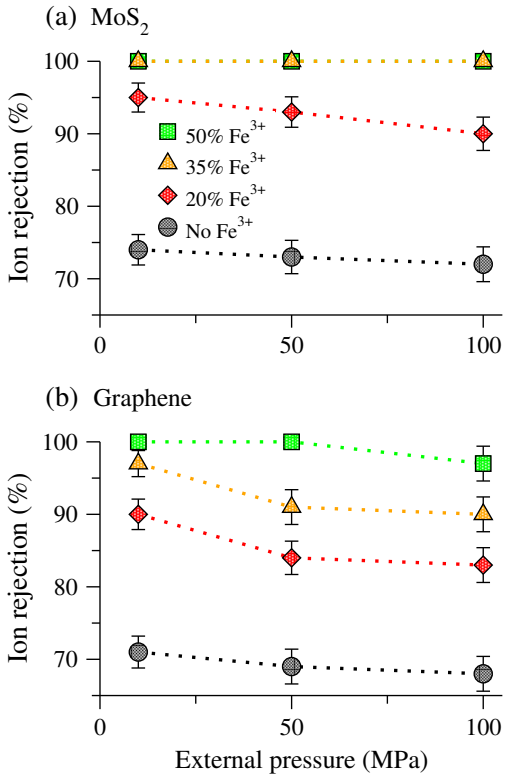

FIG. 2. Percentage of ion rejection as a function of the applied pressure for (a) MoS_2 and (b) graphene with distinct concentrations of ferric chloride. The dotted lines are a guide to the eye.

is a consequence of the nozzle-like shape of the former and the hydrophilic-hydrophobic competition at the MoS_2 pore's edge[6]. In fact, the competition between hydrophilic and hydrophobic states is determinant for adhesion and blockage of ionic solutions in solid-liquid interfaces[39]. This would be useful, for instance, in nanopore power generators, with giant osmotic effects induced by ionic concentration bias[40].

The efficiency of desalination through nanoporous membranes is usually limited by the size of the pore: as the area of the pore increases, the efficiency of rejection decreases[14]. Here, we have used effective pore diameters (discounted the van der Waals radii) of ∼1 nm, larger than that used by most of simulations with nanopores[5,14,15,41]. By adding Fe^{3+} to the solution we have achieved 100% of ion blockage, which is not observed in simple saline solutions even with functionalization of the nanopore[5,41]. The mechanism behind this new behavior is that adding Fe^{3+} in the NaCl solution leads to the formation of ionic clusters. This clusterization is mainly regulated by the charge inversion phenomena occurring when the Cl^- anions are attracted by Fe^{3+}, causing the excess of negative charge and the consequently inversion of

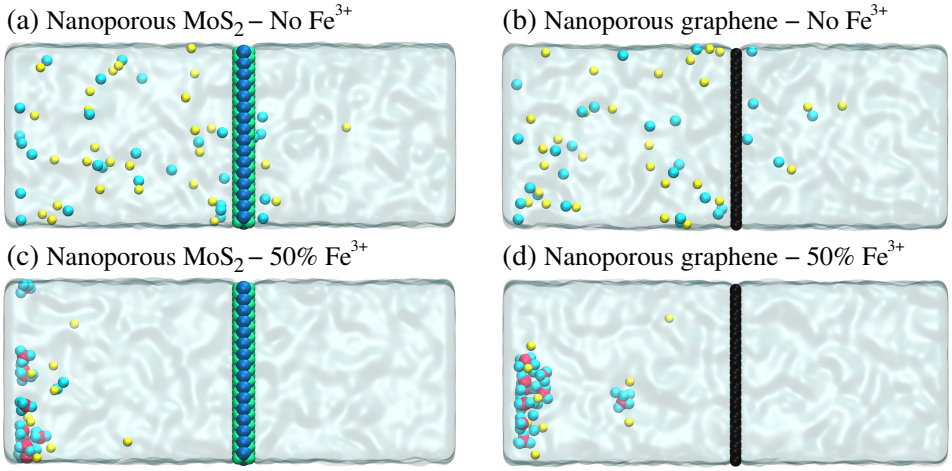

FIG. 3. (On the top) side view snapshots after 5 ns of simulations of Na^+Cl^- passing through (a) MoS_2 and (b) graphene nanopore without any trace of clusterization. (Bottom) $Fe^{3+}Cl^-$ cluster formation preventing the ion passage through (c) MoS_2 and (d) graphene nanopores. These configurations are for applied pressures of 50 MPa.

sign in the charge distribution profile. Then, the Na^+ cation is attracted to this cluster. As result, the cross section of the clusters is larger than the accessible diameter of the pore. This phenomena can be better observed in the snapshots depicted in Fig. 3. While in the absence of $Fe^{3+}Cl^-$, Figs. 3(a) and (b), the ions spread out through the simulation box, when the ferric chloride is added to the solution the ions assemble to form big clusters, avoiding the ion passage through the membrane. The rejection is then mainly dictated by the size of these clusters: when we add enough Fe^{3+} to the system the cross section of the clusters becomes larger than the accessible area within the nanopore.

Since the membrane rejection is most dependent on the ion/pore diameter ratio, with the addition of Fe^{3+} we have highly increased the desalination efficiency of the nanopore. The radial distribution function (RDF) presented in Fig. 4 highlights the ionic clusterization process as we increase the Fe^{3+} concentration. Regardless of the nanopore chemistry (graphene or MoS_2) the sodium atoms becomes closer as the number of Fe^{3+} cations added to the solution increase. The insets in Figs. 4(a) and (b) show examples of ionic clusters found in solutions with 50% of ferric chloride. These clusters are responsible for the increase in the ion rejection rate, allowing for a better use of current desalination nanotechnologies.

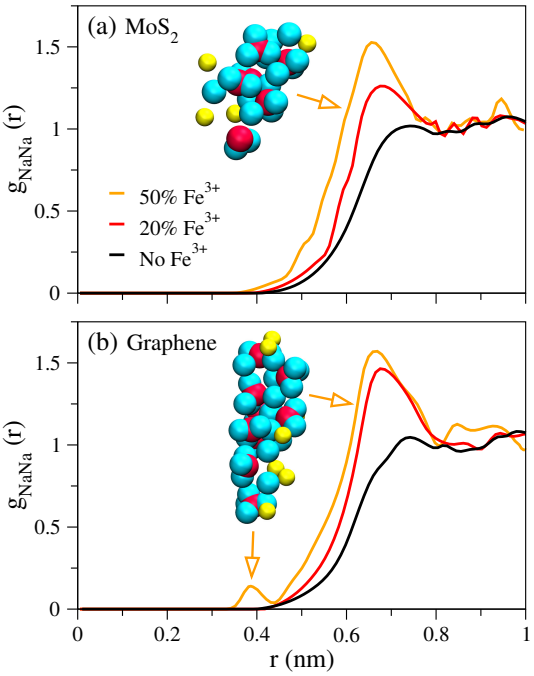

FIG. 4. Na–Na Radial distribution function for (a) Mos_2 and (b) graphene nanopores. Different ferric chloride concentrations are considered.

IV. CONCLUSIONS

Using molecular dynamics simulations we have showed that adding ferric chloride to a salt water solution can significantly increase the salt rejection by nanoporous membrane. Even for nanopores beyond 1 nm, where the efficiency of the membranes is low, the clustering process lead to a 100% salt rejection. Additionally, we have found a relation between the increase in ionic rejection and the percentage of Fe^{3+} added to the $Na^{+}Cl^{-}$ solution. As we increase the proportion of ferric chloride the Na^{+} ions aggregates forming large clusters, which is crucial for the ion blockage at the nanopore interface. This result shows how we can improve the efficiency of nanoporous membranes for water desalination using flocculant chemicals.

ACKNOWLEDGMENTS

The authors acknowledge Brazilian agencies FAPERGS, CNPq and INCT-Fcx for financial support, CENAPAD-SP and CESUP-UFRGS for the computer time. The authors

also thank Prof. Carolina de Matos and Prof. Jaqueline Vargas from UNIPAMPA for the inspirational discussions.

REFERENCES

[1]G. Xu, J. Xu, H. Su, X. Liu, Lu-Li, H. Zhao, H. Feng, and R. Das, Desalination **doi: 10.1016/j.desal.2017.09.024** (2018).

[2]Y. G. Yan, W. S. Wang, W. Li, K. P. Loh, and J. Zhang, Nanoscale **9**, 18951 (2017).

[3]K. Liu, M. Lihter, A. Sarathy, S. Caneva, H. Qiu, D. Deiana, V. Tileli, D. T. L. Alexander, S. Hofmann, D. Dumcenco, A. Kis, J.-P. Leburton, and A. Radenovic, Nano Lett. **17**, 4223 (2017).

[4]M. E. Suk and N. R. Aluru, J. Phys. Chem. Lett. **1**, 1590 (2010).

[5]D. Cohen-Tanugi and J. C. Grossman, Nano Lett. **12**, 3602 (2012).

[6]M. Heiranian, A. B. Farimani, and N. R. Aluru, Nat. Commun. **6**, 8616 (2015).

[7]J. Kou, J. Yao, L. Wu, X. Zhou, H. Lu, F. Wu, and J. Fan, Phys. Chem. Chem. Phys. **18**, 22210 (2016).

[8]H. Gao, Q. Shi, D. Rao, Y. Zhang, J. Su, Y. Liu, Y. Wang, K. Deng, and R. Lu, J. Phys. Chem. C **121**, 22105 (2017).

[9]M. Dahanayaka, B. Liu, Z. Hu, Q.-X. Pei, Z. Chen, A. W.-K. Law, and K. Zhou, Phys. Chem. Chem. Phys. **19**, 30551 (2017).

[10]Z. Li, Y. Qiu, K. Li, J. Sha, T. Li, and Y. Chen, J. Chem. Phys. **148**, 014703 (2018).

[11]V. Georgakilas, M. Otyepka, A. B. Bourlinos, V. Chandra, N. Kim, K. C. Kemp, P. Hobza, R. Zboril, and K. S. Kim, Chem. Rev. **112**, 6156 (2012).

[12]K. A. Mahmoud, B. Mansoor, A. Mansour, and M. Khraisheh, Desalination **356**, 208 (2015).

[13]Z. Hu, B. Liu, M. Dahanayaka, A. W.-K. Law, J. Wei, and K. Zhou, Phys. Chem. Chem. Phys. **19**, 15973 (2017).

[14]M. Heiranian, A. B. Farimani, and N. R. Aluru, Nat. Commun. **6**, 8616 (2015).

[15]W. Li, Y. Yang, J. K. Weber, G. Zhang, and R. Zhou, ACS Nano **10**, 1829 (2016).

[16]S. Bertolazzi, J. Brivio, and A. Kis, ACS Nano **5**, 9703 (2011).

[17]M. M. Pendergast and E. M. Hoek, Energy Environ. Sci. **4**, 1946 (2011).

[18]S. H. Jamali, T. J. H. Vlugt, and L.-C. Lin, J. Phys. Chem. C **121**, 11273 (2017).

[19]S. P. Surwade, S. N. Smirnov, I. V. Vlassiouk, R. R. Unocic, G. M. Veith, S. Dai, and S. M. Mahurin, Nat. Nanotech. **10**, 459 (2015).

[20]S. Garaj, W. Hubbard, A. Reina, J. Kong, D. Branton, and J. A. Golovchenko, Nature **467**, 190 (2010).

[21]K. Yoon, A. Rahnamoun, J. L. Swett, V. Iberi, D. A. Cullen, I. V. Vlassiouk, A. Belianinov, S. Jesse, X. Sang, O. S. Ovchinnikova, A. J. Rondinone, R. R. Unocic, and A. C. van Duin, ACS Nano **10**, 8376 (2016).

[22]S. C. OHern, D. Jang, S. Bose, J.-C. Idrobo, Y. Song, T. Laoui, J. Kong, and R. Karnik, Nano Lett. **15**, 3254 (2015).

[23]K. Liu, J. Feng, A. Kis, and A. Radenovic, ACS Nano **8**, 2504 (2014).

[24]J. Feng, K. Liu, M. Graf, M. Lihter, R. D. Bulushev, D. Dumcenco, D. T. L. Alexander, D. Krasnozhon, T. Vuletic, A. Kis, and A. Radenovic, Nano Lett. **15**, 3431 (2015).

[25]S. M. Gilbert, G. Dunn, A. Azizi, T. Pham, B. Shevitski, E. Dimitrov, S. Liu, S. A., and A. Zettl, Sci. Rep. **7**, 15096 (2017).

[26]C. M. Frament and J. R. Dwyer, J. Phys. Chem. C **116**, 23315 (2012).

[27]C. Wen, Z. Zhang, and S.-L. Zhang, ACS Sens. **2**, 1523 (2017).

[28]S. Pianegonda, M. C. Barbosa, and Y. Levin, Europhys. Lett. **71**, 831 (2005).

[29]A. Diehl and Y. Levin, J. Chem. Phys. **129**, 124506 (2008).

[30]J. Abascal and C. Vega, J. Chem. Phys. **123**, 234505 (2005).

[31]J. P. Ryckaert, G. Ciccotti, and H. J. C. Berendsen, J. Comput. Phys. **23**, 327 (1977).

[32]M. H. Köhler, J. R. Bordin, and M. C. Barbosa, J. Chem. Phys. **148**, 222804 (2018).

[33]R. W. Hockney and J. W. Eastwood, *Computer Simulation Using Particles*, McGraw-Hill, New York, 1981.

[34]S. Nosé, Mol. Phys. **52**, 255 (1984).

[35]W. G. Hoover, Phys. Rev. A. **31**, 1695 (1985).

[36]G. J. Martyna, D. J. Tobias, and M. L. Klein, J. Chem. Phys. **101**, 4177 (1994).

[37]K. Breitsprecher, M. Abele, S. Kondrat, and C. Holm, J. Chem. Phys. **147**, 104708 (2017).

[38]J. R. Bordin, A. Diehl, M. C. Barbosa, and Y. Levin, Phys. Rev. E **85**, 031914 (2012).

[39]D. Surblys, F. Leroy, Y. Yamaguchi, and F. Muller-Plathe, J. Chem. Phys. **148**, 134707 (2018).

[40]Z. Huang, Y. Zhang, T. Hayashida, Z. Ji, Y. He, M. Tsutsui, X. S. Miao, and M. Taniguchi, Appl. Phys. Lett. **111**, 263104 (2017).